2018

THE FORMATION MECHANISM OF α-PHASE DISPERSOIDS AND QUANTIFICATION OF FATIGUE CRACK INITIATION BY EXPERIMENTS AND THEORETICAL MODELING IN MODIFIED AA6061 (AL-MG-SI-CU) ALLOYS

Gongwang Zhang
University of Kentucky, gongwangzhang@outlook.com
Author ORCID Identifier:
https://orcid.org/0000-0003-4357-1711
Digital Object Identifier: https://doi.org/10.13023/etd.2018.429

STUDENT AGREEMENT:

I represent that my thesis or dissertation and abstract are my original work. Proper attribution has been given to all outside sources. I understand that I am solely responsible for obtaining any needed copyright permissions. I have obtained needed written permission statement(s) from the owner(s) of each third-party copyrighted matter to be included in my work, allowing electronic distribution (if such use is not permitted by the fair use doctrine) which will be submitted to UKnowledge as Additional File.

I hereby grant to The University of Kentucky and its agents the irrevocable, non-exclusive, and royalty-free license to archive and make accessible my work in whole or in part in all forms of media, now or hereafter known. I agree that the document mentioned above may be made available immediately for worldwide access unless an embargo applies.

I retain all other ownership rights to the copyright of my work. I also retain the right to use in future works (such as articles or books) all or part of my work. I understand that I am free to register the copyright to my work.

REVIEW, APPROVAL AND ACCEPTANCE

The document mentioned above has been reviewed and accepted by the student's advisor, on behalf of the advisory committee, and by the Director of Graduate Studies (DGS), on behalf of the program; we verify that this is the final, approved version of the student's thesis including all changes required by the advisory committee. The undersigned agree to abide by the statements above.

Gongwang Zhang, Student

Dr. Tongguang Zhai, Major Professor

Dr. Matthew Beck, Director of Graduate Studies

THE FORMATION MECHANISM OF α-PHASE DISPERSOIDS AND QUANTIFICATION OF FATIGUE CRACK INITIATION BY EXPERIMENTS AND THEORETICAL MODELING IN MODIFIED AA6061 (AL-MG-SI-CU) ALLOYS

DISSERTATION

A dissertation submitted in partial fulfillment of the requirements for the degree of Doctor of Philosophy in the College of Engineering at the University of Kentucky

By
Gongwang Zhang
Lexington, Kentucky
Director: Dr. Tongguang Zhai, Associate Professor of Materials Engineering
Lexington, Kentucky
2018

https://orcid.org/0000-0003-4357-1711

ABSTRACT OF DISSERTATION

THE FORMATION MECHANISM OF α-PHASE DISPERSOIDS AND QUANTIFICATION OF FATIGUE CRACK INITIATION BY EXPERIMENTS AND THEORETICAL MODELING IN MODIFIED AA6061 (AL-MG-SI-CU) ALLOYS

AA6061 Al alloys modified with addition of Mn, Cr and Cu were homogenized at temperatures between 350 °C and 550 °C after casting. STEM experiments revealed that the formation of α-Al(MnFeCr)Si dispersoids during homogenization were strongly affected by various factors such as heating rate, concentration of Mn, low temperature pre-nucleation treatment and homogenization temperature. Through analysis of the STEM results using an image software Image-Pro, the size distributions and number densities of the dispersoids formed during different annealing treatments were quantitatively measured. It was revealed that increasing the heating rate or homogenization temperature led to a reduction of the number density and an increase in size of the dispersoids. The number density of dispersoids could be markedly increased through a low temperature pre-nucleation treatment. A higher Mn level resulted in the larger number density, equivalent size and length/width ratio of the dispersoids in the alloy.

Upsetting tests on two of these Mn and Cr-containing AA6061 (Al-Mg-Si-Cu) Al alloys with distinctive Mn contents were carried out at a speed of 15 mm s^{-1} under upsetting temperature of 450 ºC after casting and subsequent homogenization heat treatment using a 300-Tone hydraulic press. STEM experiments revealed that the finely distributed α-Al(MnFeCr)Si dispersoids formed during homogenization showed a strong pinning effect on dislocations and grain boundaries, which could effectively inhibit recovery and recrystallization during hot deformation in the two alloys. The fractions of recrystallization after hot deformation and following solution heat treatment were measured in the two alloys with EBSD. It was found that the recrystallization fractions of the two alloys were less than 30%. This implied that the finely distributed α-dispersoids were rather stable against coarsening and they stabilized the microstructure by inhibiting recovery and recrystallization by pinning dislocations during deformation and annealing at elevated temperatures. By increasing the content of Mn, the effect of retardation on recrystallization were further enhanced due to the formation of higher number density of the dispersoids.

STEM and 3-D atom probe tomography experiments revealed that α-Al(MnFeCr)Si dispersoids were formed upon dissolution of lathe-shaped Q-AlMgSiCu phase during homogenization of the modified AA6061 Al alloy. It was, for the first time, observed that Mn segregated at the Q-phase/matrix interfaces in Mn-rich regions in the early stage of homogenization, triggering the transformation of Q-phase into strings of Mn-rich dispersoids afterwards. Meanwhile, in Mn-depleted regions the Q-phase remained unchanged without segregation of Mn at the Q-phase/matrix interfaces. Upon completion of α-phase transformation, the atomic ratio of Mn and Si was found to be 1:1 in the α-phase. The strengthening mechanisms in the alloy were also quantitatively interpreted, based on the measurements of chemical compositions, dispersoids density and size, alloy hardness and resistivity as a function of the annealing temperature. This study clarified the previous confusion about the formation mechanism of α-dispersoids in 6xxx series Al alloys.

Four-point bend fatigue tests on two modified AA6061 Al alloys with different Si contents (0.80 and 1.24 wt%, respectively) were carried out at room temperature, f = 20 Hz, R = 0.1, and in ambient air. The stress-number of cycles to failure (S-N) curves of the two alloys were characterized. The alloys were solution heat treated, quenched in water, and peak aged. Optical microscopy and scanning electron microscopy were employed to capture a detailed view of the fatigue crack initiation behaviors of the alloys. Fatigue limits of the two alloys with the Si contents of 0.80 and 1.24 wt% were measured to be approximately 224 and 283.5 MPa, respectively. The number of cracks found on surface was very small (1~3) and barely increased with the applied stress, when the applied stress was below the yield strength. However, it was increased sharply with increase of the applied stress to approximately the ultimate tensile strength. Fatigue crack initiation was predominantly associated with the micro-pores in the alloys. SEM examination of the fracture surfaces of the fatigued samples showed that the crack initiation pores were always aspheric in shape with the larger dimension in depth from the sample surface. These tunnel-shaped pores might be formed along grain boundaries during solidification or due to overheating of the Si-containing particles during homogenization.

A quantitative model, which took into account the 3-D effects of pores on the local stress/strain fields in surface, was applied to quantification of the fatigue crack population in a modified AA6061 Al alloy under cyclic loading. The pores used in the model were spherical in shape, for simplicity, with the same size of 7 μm in diameter. The total volume fraction of the pores in the model were same as the area fraction of the pores measured experimentally in the alloy. The stress and strain fields around each pore near the randomly selected surface in a reconstructed digital pore structure of the alloy were quantified as a function of pore position in depth from the surface using a 3-D finite element model under different stress levels. A micro-scale Manson-Coffin equation was used to estimate the fatigue crack incubation life at each of the pores in the surface and subsurface. The population of fatigue cracks initiated at an applied cyclic loading could be subsequently quantified. The simulated results were consistent with those experimentally measured, when the applied maximum cyclic stress was below the yield strength, but the model could not capture the sudden increase in crack population at UTS, as observed in the alloy. This discrepancy in crack population was likely to be due to the use of the spherical pores in the

model, as these simplified pores could not show the effects of pore shape and their orientations on crack initiation at the pores near surface. Although it is presently very time-consuming to calculate the crack population as a function of pore size and shape in the alloy with the current model, it would still be desirable to incorporate the effects of shape and orientation of the tunnel-shaped pores into the model, in the future, in order to simulate the fatigue crack initiation more accurately in the alloy.

KEYWORDS: Al-Mg-Si-Cu Alloy, High Temperature Precipitation, Recrystallization, Porosities, Multi-site Fatigue Crack Initiation, Finite Element Modeling

Gongwang Zhang

10/27/2018

THE FORMATION MECHANISM OF α-PHASE DISPERSOIDS AND QUANTIFICATION OF FATIGUE CRACK INITIATION BY EXPERIMENTS AND THEORETICAL MODELING IN MODIFIED AA6061 (AL-MG-SI-CU) ALLOYS

By
Gongwang Zhang

Dr. Tongguang Zhai
Director of Dissertation

Dr. Matthew Beck
Director of Graduate Studies

10/27/2018
Date

ACKNOWLEDGMENTS

First of all, I would like to gratefully thank my advisor Dr. Tongguang Zhai for giving me this opportunity to pursue my Ph.D degree at University of Kentucky and his valuable academic guidance on my work. In particular, I would like to thank his patience in teaching on how to keep a logical and scientific way to think and write, which will help me achieve my career goals in the future.

I am also grateful to my committee members: Dr. John Balk, Dr. Matthew Beck and Dr. I. S. Jawahir, as well as Dr. Robert B. Grossman serving as my outside examiner, for their professional comments and suggestions that guided my research work.

I would furthermore greatly acknowledge Prof. Hiromi Nagaumi and Dr. Yi Han at Suzhou Research Institute for Nonferrous Metals, China for providing research opportunities and financial support. Meanwhile, many thanks for Dr. Chad Parish and Donovan Leonard at Oak Ridge National Laboratory, Dr. Dali Qian, Dr. Nicolas Briot and Nancy Miller at University of Kentucky for their technical assistance in STEM, 3-D APT, SEM and other experiments. Moreover, I would like to thank my former and current group members, including Dr. Yan Jin, Dr. Lin Yang, Pei Cai, Liang Chen and Rami A. Almatani, who have been very helpful in academic discussion and experimental work.

Last but not least, I would like to express my gratitude to my families, particularly my wife, Mingzhu Cai, for their priceless love and support in the past five years Ph.D study.

TABLE OF CONTENTS

LIST OF TABLES

LIST OF FIGURES

Chapter 1 Introduction

1.1 Aluminum and aluminum alloys

Aluminum (Al) is the third most abundant element and the second most abundant metallic element in the Earth's crust and is most heavily used metal except iron in the world. It possesses a mass density of 2.698 g/cm^3 and crystal structure of FCC with lattice parameter a = 0.405 nm in metal form over the temperature range from 4 K up to the melting point of 933 K. However, Al does not exist in the pure metal form, but binds with other elements forming compounds because of its high chemical affinity. Al compounds are primarily the oxide with various purity and hydration, and to extract Al metal from Al oxide ores like Bauxite, Nepheline rocks, Alunite, etc., two independent industrial processes are employed: production of an Al oxide from Al ores by different chemical methods, and production of Al from an Al oxide using electrolysis with fused Na_3AlF_6 (cryoliye). Due to the unique properties of Al (alloys) - low density (~1/3 of the density of steel), high strength and good formability, thermal and electrical conductivity, high corrosion resistance and recyclability, it has been increasingly used in many conventional and novel engineering applications, such as automobile, aerospace, packaging of food and beverages, building and construction, electricity transmission, manufacture of tools, production of durable consumer and ecologically sustainable products, etc. [1-4].

Through addition of other elements to form alloys, the application of Al can be expanded to other engineering fields [1-4]. Differing in forming routes, Al alloys are divided into two main categories: wrought and cast alloys. Wrought Al alloys are more widely used than cast alloys, since virtually every available metal forming process can be used to form Al. The forms of wrought Al alloys include sheet and plate, foil, extrusions, bar, rod, wire, forgings and impacts, drawn and extruded tubing, etc. Cast alloys are directly produced by various casting methods without any plastic deformation, such as die casting, direct chill casting, etc., where the casting is the final form. According to the alloying elements, the two classes of Al alloys are sorted into different series. The designation systems for wrought and cast Al alloys are given in Table 1.1. Wrought Al alloys are further categorized into non-heat-treatable and heat-treatable alloys. Heat-treatable Al alloys are

strengthened by solution heat treatment followed by water quenching and aging, which include 2xxx, some 4xxx, 6xxx and 7xxx series alloys. Whereas non-heat-treatable Al alloys obtain their strength through solid solution or dispersoid hardening. The strengthening effect could be further enhanced by strain hardening, and this class of wrought Al alloys include 1xxx, 3xxx, 4xxx and 5xxx series alloys. Cast Al alloys are either used in the as-cast or heat-treated conditions and cannot be strengthened by work hardening.

1.1.1 Different series of wrought Al alloys

Different series of wrought Al alloys possess different mechanical properties by adding various elements, fulfilling the specific requirements for applications in different areas [1-4]. 1xxx series Al alloys include 99.0% to 99.99% of Al (controlled unalloyed (pure) composition). This series of Al alloys have low mechanical strength, high ductility, excellent corrosion resistance and high electrical conductivity, which are primarily used in electrical and chemical industries. 2xxx series Al alloys contain copper (Cu) as the major alloying element, and other elements, notably magnesium (Mg), may be added. This series of Al alloys with high mechanical strength and low corrosion resistance are widely used in aircraft area. Manganese (Mn) is the principal alloying element in 3xxx series Al alloys. With moderate mechanical strength, high ductility and excellent corrosion resistance, 3xxx series Al alloys are used as general-purpose alloys for architectural applications and various products. 4xxx series Al alloys include silicon (Si) as the major alloying element, applied in welding rods and brazing sheet. The major alloying element in 5xxx series Al alloys is magnesium (Mg). Alloys of this series have moderate to high mechanical strength combined with relatively high ductility, good corrosion resistance and weldability, which are applied for boat hulls, gangplanks, and other products exposed to marine environments. 6xxx series Al alloys contain magnesium (Mg) and silicon (Si) as the principal alloying elements. Alloys of this series possess high mechanical strength combined with good formability and corrosion resistance, commonly used for architectural extrusions and automotive components. Zinc (Zn) is the major alloying element in 7xxx series Al alloys, although other elements, such as copper (Cu), magnesium (Mg), chromium (Cr), and zirconium (Zr), may be specified. The applications of 7xxx series Al alloys include aircraft

structural components and other high-strength applications, since this series of Al alloys have the highest mechanical strength with good corrosion resistance, weldability and formability. 8xxx series Al alloys constitute miscellaneous compositions and are alloyed with other elements which are not covered by other series. Aluminum (Al) - lithium (Li) alloys are an example.

1.1.2 Strengthening mechanisms in Al alloys

Due to the low strength and toughness, pure Al cannot be readily used in applications where severe deformation and fracture could easily occur. Generally, several hardening mechanisms can be applied to strengthening of Al alloys, such as work or strain hardening, grain refinement hardening, solid solution hardening, dispersoid hardening, precipitation hardening and texture hardening [1,2,6-10].

For most metals, work hardening can increase the strength and hardness at the expense of ductility and formability through plastic deformation, which is the principle means to strengthen non-heat-treatable alloys [1,2,6-10,11]. When a metal is plastically deformed, existing dislocations move, and new dislocations are created through mechanisms such as Frank - Read source. During deformation, dislocations will interact each other and become pinned or tangled, leading to low mobility of the dislocations, which causes further deformation to become more difficult and thus the strengthening of the metal. In addition, work hardening only works at a temperature low enough where recovery and recrystallization will not occur to return the metal to the fully annealed state with an appreciable rate, lowering the strength below the design level. Cold rolling of sheet and foil is the most common means of work hardening in non-heat-treatable Al alloys.

The grain size within a material influences the strength of the material [1,2,6-8,10,12]. Since the orientation of the slip planes and directions between two neighboring grains is different, a dislocation cannot continue its slip motion into another grain when reaching a grain boundary. The grain boundary serves as a barrier to movement of dislocations which pile up near the boundary. With decreasing grain size, shorter distance can be moved by a

glissile dislocation before reaching a grain boundary, improving the strength of a material. Strengthening by grain refinement is commonly described by the Hall–Petch relation:

$$\sigma_y = \sigma_0 + kd^{-1/2} \quad (1.1)$$

where σ_y is the yield stress of the alloy, σ_0 is the frictional stress, d is the average grain size and k is referred to Hall-Petch constant, characterizing the difficulty of transmitting slip across the grain boundary for a given alloy system. Although the value of k is approximately five times smaller than ferrous alloys, considerable grain size strengthening can still be achieved at very fine grain sizes in Al alloys, where Hall-Petch relation remains operative.

Alloying elements can dissolve into the Al matrix and form a solid solution through solution heat treatment. Solid solution hardening is caused by the interaction of alloying elements with dislocations, which act as barriers to the dislocation motion to increase strength [1,6-8,10,13]. Three different ways are provided in which solute atoms can interact with dislocations: Parelastic interaction (lattice parameter effect), Dielastic interaction (shear modulus effect) and Chemical interaction (Suzuki effect). Parelastic interaction is caused by the atomic size difference between solute and matrix atoms, leading to compressive or tensile stresses, which depends on whether the solute atom is larger or smaller than the matrix atoms. The elastic distortion energy by the solute atom is reduced if segregation of solute atoms from perfect crystal to dislocations occurs. When such dislocations move, the separation of dislocations and solute atoms require the expenditure of elastic energy obtained during segregation, corresponding to a back stress on the dislocations, which results in an additional stress applied to overcome this stress, and thus increase the critical resolved shear stress of the alloys compared to that of the pure matrix. In the dielastic interaction, since the energy density of a dislocation is proportional to the shear modulus, the total energy of the dislocation contributed by the solute atoms with different shear modulus is different from pure solvent atoms, leading to a dielastic interaction force. Chemical interaction effect is caused by the dependence of the stacking fault energy on chemical composition. Increasing solute concentration can decrease stacking fault energy through segregation of solute atoms to dislocations. If the dislocation

moves, the segregated solute atoms are left behind, which increases the dislocation energy, making itself felt as a back stress on the dislocation.

Transition elements like Mn, Cr and Zr are typically added to Al alloys to form non-deformable fine incoherent dispersoids by solid state precipitation, either during ingot preheating or thermal heat treatment of cast shapes to inhibit dislocations movement and thus obtain substantial strengthening effect. These elements have slow diffusivity, which are soluble in molten Al but with limited solubility in solid Al. In addition, nonmetallic particles like oxides, carbides, or borides contained in Al alloys can also achieve this hardening effect. Since the dislocations cannot cut or penetrate these hard particles (dispersoids), they have to circumvent the particles by bowing out between the particles with the formation of dislocation loops - Orowan mechanism, which not only engenders strong contribution to the yield stress, but also leads to significant strain hardening, much larger than that in pure metals or solid solutions. Dispersoid hardening also contributes in the aged condition when incoherent particles precipitate and do not deform with the matrix [1,2,6-10,14-16].

During precipitation hardening of Al alloys, alloying elements are brought into solid solution of alloys, which have a sloping solvus line, at high temperatures and after quenching the alloys to room temperatures, metastable phases with (partially) coherent phase boundaries with the matrix are precipitated from the supersaturated solid solution at ambient temperature (nature aging) or at elevated temperature (artificial aging). These precipitates can be cut through by moving dislocations; however, forces will be exerted on the motion of dislocations which have to be overcome, resulting in the increase of the strength of Al alloys [1,2,6-10]. Coherency strain and chemical hardening are at least two causes of the inhibition of dislocations motion, which result in precipitation hardening. Coherency strain hardening is caused by the slight misfit between precipitated particles and the matrix, giving rise to stress fields which hinder the movement of gliding dislocations. Chemical hardening provides a short-range interaction between dislocations and precipitates when dislocations pass through, which arises from four possible causes: (a) the energy required to create two ledges of an additional particle-matrix interface; (b)

the additional work required to create an anti-phase boundary (APB) on the slip plane of the particle with ordered structure; (c) the change in width of a dissociated dislocation as it passes through the particle where the stacking fault energy differs from the matrix; and (d) the dislocation energy change due to the difference in shear modulus of the particle and the matrix.

Al alloys with a preferred orientation will show plastic anisotropy depending on the perfection of the texture, which can also increase the strength of the alloys [2,7,17]. In commercial Al alloys, the mechanisms of strengthening disscussed above are often combined to provide even higher strength for applications [1,18,19].

1.2 Wrought 6xxx series Al alloys

The 6xxx series heat-treatable wrought Al-Mg-Si(-Cu) alloys have been the topic of this dissertation. These alloys have an excellent combination of medium strength, favorable formability, good corrosion resistance and lower costs. As a result, they are increasingly used in automotive applications to improve the fuel-efficiency and mechanical performance of automobiles. The main alloying elements in 6xxx series alloys are Mg and Si, sometimes with a minor addition of Cu to further enhance the mechanical properties [1-5,9].

1.2.1 Constituent phases in 6xxx series Al-Mg-Si-(Cu) alloys

The constituent phases are formed during casting of the Al-Mg-Si-(Cu) alloys, which do not dissolve in the Al matrix during following homogenization even for a long period of time, although they may change in composition and morphology. Figure 1.1 shows several types of constituents in as-cast state of a Cr-containing AA6005 Al alloy [20]. Three most prevalent constituents in 6xxx series alloys are the monoclinic β-AlFeSi phase, the hexagonal α_h-AlFeSi phase and the cubic α_c-Al(FeMn)Si phase [20-40]. The plate-like β-AlFeSi phase has a monoclinic crystal structure with the stoichiometry of approximately Al_5FeSi [21,22]. Compared with the α_c-phase, there is no Mn present in the β-phase. The hexagonal α_h-AlFeSi phase forms in 6xxx series alloys when Mn or Cr concentration is less than about 0.01wt% [20,21,23]. Its approximate stoichiometry is Al_8Fe_2Si, in which

the concentrations of Fe and Si range from 30-33 wt% Fe and 5-12 wt% Si, respectively [21]. Only in high purity Al-Fe-Si cast alloys, the β-phase can transform to the stable α_h-phase during homogenization [21,41]. The approximate stoichiometry of the cubic α_c-phase is generally displayed by $Al_{12}(Fe_xMn_{1-x})_3Si$ [21,33], in which Fe atoms are interchangeable with V, Cr and/or Mn atoms, causing a change in crystallographic space group and a small shift in lattice parameters [21]. The α_c-phase with a "Chinese-script" morphology is formed during casting, mostly with a high Fe/Mn ratio. During homogenization, α_c-phase, with an intermediate Fe/Mn ratio, can also be formed through the β-to-α transformation, in which plate-like β-Al_5FeSi particles transform to multiple rounded α-AlFeMnSi particles with the diffusion of Mn, presented as a string of α_c-particles located on the previous location of the original β-particle [20,21,32,42-44]. The morphological change of this transformation is represented in Figure 1.2 [44]. The transformation rate and stability of the constituent phases are influenced by the chemical compositions of the alloys [22,23,43]. In addition, Mg and Si elements are partly dissolved into the primary Al matrix and to a certain extent are present in the form of Mg_2Si constituent phase during casting, as shown in Figure 1.1 [20].

1.2.2 Dispersoid phases in 6xxx series Al-Mg-Si-(Cu) alloys

Transition elements of Mn and/or Cr are often added into 6xxx series Al-Mg-Si-(Cu) alloys to further enhance the mechanical properties by formation of fine α-Al(MnCrFe) dispersoids (10-500 nm in diameter) during high temperature annealing (400-550 °C), as given in Figure 1.3 [45], which could act as recovery/recrystallization inhibitors during high temperature deformation and following annealing treatment due to their fairly high density and high thermal stability, enhancing both the strength and toughness of the alloys [20,45-49]. For example, Jeniski et al. [46] studied the effect of Mn content on the formation of Mn-containing dispersoids and recrystallization in an AA6013 Al alloy. It was found that by increasing the content of Mn, the volume fraction of dispersoids was increased, thereby enhancing the resistance to recrystallization in the alloy. Hu et al.'s [48] investigation on the precipitation of Mn-containing dispersoids and recrystallization behavior in an AA6082 Al alloy showed that the fine spherical-shaped dispersoids with uniform distribution, formed during homogenization using the slower heating rate, were

very effective for the retardation of recrystallization during annealing treatment after cold rolling. The research work by Lee et al. [49] illustrated that the increase of the strength and fracture toughness in Al-Mg-Si alloys with high Mn content was attributed to the formation of Mn-bearing dispersoids.

The α-Al(MnCrFe)Si dispersoids are reported to have a cubic unit cell with the lattice parameter a in the range of 1.25-1.27 nm, which are suggested as isomorphous to AlMnSi (Pm3 space group [29]) and AlFeSi (Im3 space group [30]). The chemical composition of α-dispersoids is between α-AlMnSi and α-AlFeSi, in which Fe and Mn (Cr) could substitute each other freely in a wide range. However, the controversy whether the structure is simple cubic (SC) or body centered cubic (BCC) still exists. It has been found that with an increase of the Fe/Mn ratio in cubic α-dispersoids (Fe/Cr ratio in α-Al(CrFe)Si dispersoids), the crystal structure tends to transform from SC structure to BCC structure [20,45,50,51]. When only Cr is present, in addition to α-Al(CrFe)Si dispersoids, α'-AlCrSi dispersoids with face centered cubic (FCC) unit cell (lattice parameter a = 1.092 nm) and structural formula of $Cr_4Si_4Al_{13}$ could be formed [20,52]. The precipitation behavior of the α-dispersoids during homogenization of an Al-Mg-Si alloy has been extensively investigated by Yoo et al. [50]. A dispersoids crystal structure transformation accompanying Mn/Fe ratio change was reported. With higher Mn/Fe ratio, the disperoids had a simple cubic (SC) crystal structure, while with lower Mn/Fe ratio, the crystal structure became body centered cubic (BCC), both of which had the lattice parameter about 1.25 nm. As illustrated in Figure 1.4, a critical Mn/Fe ratio for this transformation was found to be about 1.6 under the specific experimental details applied in their study. Besides Mn/Fe ratio, the temperature and time of heat treatments were also observed to affect the structure transformation. Donnadieu et al. [33] studied the Mn and Fe-containing phases in AA6013 Al alloys. It was found that the small α-dispersoids (with sizes between 0.1 and 0.3 μm), formed during preheating with a Mn/Fe ratio larger than 3 regardless of the nominal composition of the alloys, had Pm3 space group with the lattice parameter close to 1.27 nm. And the increase of Mn was observed to favor long range ordering transition from Im3 to Pm3 space group. Strobel et al. [53] investigated the α-dispersoids at three different homogenization treatments in an AA6082 Al alloy. It was reported that the small

dispersoids formed during heating to homogenization temperature were α-$Al_{15}(MnFe)_3Si_2$ with SC structure and high Mn/Fe ratio, while coarse particles that were present after further homogenization were α-$Al_{12}(MnFe)_3Si$ with BCC structure and low Mn/Fe ratio. The transition in crystal structure might be controlled by the diffusion of Fe to the coarse particles and substitution for Mn.

Because of the complex structures and incoherent interfaces to the Al matrix, homogeneous nucleation of α-dispersoids seems to be excluded [45]. Several heterogeneous nucleation sites have thus been suggested. Hirasawa [54] studied the formation of Mn-containing dispersoids during high temperature annealing in Al-Mg-Si alloys containing Mn. It was reported that the intermediate form of β-Mg_2Si phase (β”- and β’-Mg_2Si needles), formed in the heating period, could act as nucleation sites for the dispersoids during annealing at 350 ˚C. In addition, at higher temperature probably around 400 ˚C, cubic α-$Al_5Mn_{12}Si_7$ dispersoids with a = 1.267 nm seemed to precipitate on the plate-like β-Mg_2Si phase. Hu et al. [48] reported that during homogenization of a Mn-containing AA6082 Al alloy with the appropriate heating rate, the Mn-containing dispersoids were observed to nucleate preferentially on the needle shaped β’-Mg_2Si phase that first nucleated along the <100> directions of the Al matrix as shown in Figure 1.5. With increasing homogenization temperature and time, the β’-Mg_2Si phase gradually disappeared, and finally only the dispersoids were left. Lodgaard and Ryum [20,45] has done a thorough investigation on the nucleation mechanism of α-dispersoids during heat treatments in Al-Mg-Si alloys with varying amounts of Mn and/or Cr. A rod-shaped intermediate phase, referred to as the ‘u-phase’, was found to nucleate on the β’-Mg_2Si needles and be lined up in the <100> directions in the Al lattice during the heating of the as-cast alloys to 580 ˚C at a heating rate of 3 K min^{-1}. This phase was reported to have the hexagonal structure and be rich in Mn and/or Cr, which was considered to act as the preferential nucleation site for the α-dispersoids (Figure 1.6). It was also found that the distribution of dispersoids was strongly affected by the heating procedure and Si concentration in the matrix, which was due to their effects on the precipitation of β’-precipitates that was a prerequisite for the formation of the nucleation sites (‘u-phase’) for the α-dispersoids.

1.2.3 Ageing response in 6xxx series Al-Mg-Si-(Cu) alloys

The strength of the wrought Al-Mg-Si alloys can be largely enhanced through age hardening which is achieved by T6 artificial aging treatment (typically between 150 and 250 $^{\circ}$C for 10-20 hours) after appropriate solution and quenching treatments that generate a supersaturated solid solution. During aging treatment, the supersaturation of the solute atoms in Al matrix is gradually reduced, and the strength increase results from the formation of a high density of fine coherent or semi-coherent precipitates of Mg and Si which act as obstacles to dislocations movement during mechanical loading. Although a number of studies concerning the kinetics and structure of precipitates are available, controversy still exist concerning the precipitation process and compositions of intermediate precipitates. The generic precipitation sequence for 6xxx series alloys during artificial aging, which is generally accepted in the literature, can be described as follows [55-68]: SSSS → atomic clusters → GP zones → β” → β’ → β-phase

where SSSS refers to the initial supersaturated solid solution and GP zones stand for Guinier-Preston zones. Some authors consider the GP zones as GP1 zones, while the β”-phase is called a GP2 zone [55,56]. At the beginning of the precipitation process, Si and Mg start to form clusters, which are initially rich in Si due to its lower solubility in Al and its higher diffusion speed, and subsequently, Mg and more Si diffuse into the Si-rich clusters to form Mg-Si clusters [55,57] driven by the large amount of quenched-in vacancies. The GP zones formed after the Mg/Si clusters during the initial stages of precipitation. In general, the clusters and GP zones are reported to be spherical, which are aggregates of disordered solute atoms and fully coherent with the Al matrix [58]. Compared to the much smaller co-clusters, GP zones are thermally more stable and contain considerably more solute atoms with typical sizes of 1-3 nm, in which the Mg/Si ratio is usually < 1 [57,59-63]. The pre-β”-phase with a composition of $(Al+Mg)_5Si_6$ is considered to be the most developed GP zone and occurs just before the formation of the β”-phase. The unit cell of pre-β”-phase is only slightly different from that of the β”-phase, and during annealing, the Al atoms in pre-β”-phase are replaced by Mg and Si atoms to form β”-phase [56,58].

Upon further aging, the clusters and GP zones can serve as nucleation sites for the β”-precipitates. The β”-phase was reported to be formed after GP zones and before the β’-phase, which has the needle-like morphology (typically about 4 x 4 x 50 nm^3) aligned along the $<1\ 0\ 0>_{Al}$ directions and is fully coherent along the needle axis (b-axis) and semi-coherent along a and c axes [55,58-61,64]. The β”-phase is considered as the dominant strengthening phase, mostly responsible for the peak-hardening effect [55,58-61,65], due to its semi-coherent interface with the Al matrix together with its high number density [63], which is more effective for dislocation pinning. Various crystal structures reported in the early studies include monoclinic structure with a = c = 0.616 nm, b = 0.71 nm, $\beta = 82^{\circ}$, monoclinic structure with a = 0.30 nm, b = 0.33 nm, c = 0.40 nm, $\gamma = 71^{\circ}$, and hexagonal structure with a = 0.705 nm, c = 0.405 nm [9]. By means of high resolution electron microscopy and electron diffraction, the β”-precipitate is proposed to have C-centered monoclinic structure (space group of C2/m, a = 1.516 nm, b = 0.405 nm, c = 0.674 nm, $\beta = 105.3^{\circ}$) with the atomic composition of Mg_5Si_6 [59], which is identical to the based-centered monoclinic structure determined by Edwards et al. in a Cu-containing Al-Mg-Si alloy [57]. The typical morphology of β”-phase is shown in Figure 1.7 [59].

The next phase appearing in the aging sequence after β”-phase is the β’-phase, which is formed as rods with their long c-axes parallel to and fully coherent with $<100>_{Al}$ directions, having hexagonal crystal structure with lattice parameters a = 0.705nm and c = 0.405nm [9,55,57-62,66]. The β’-phase has the Mg/Si ratio close to the equilibrium Mg_2Si phase, which is determined to be 1.68 [57,59,61,62]. It is also suggested that the β’-phase has a hexagonal structure (space group P63/m, a = 0.715 nm, c = 1.215 nm) with a formula of Mg_9Si_5 [9,55,58]. The structure and composition of the equilibrium β-phase has been well established to be the fluorite type FCC structure with a = 0.639 nm and composition of Mg_2Si, which appears as platelets along $\{100\}_{Al}$ planes with dimensions of several micrometers [55,58-61,65]. The rod-shaped β’-phase as well as the corresponding equilibrium β-phase are characteristic of the overaged conditions, which exhibit reduced mechanical properties [58,65]. Plates of Si can be formed together with the β-phase in Al-Mg-Si alloys rich in Si, which are also viewed as equilibrium phase [58,67,68]. Actually, the precipitation sequence is more complex than the given generic sequence. In addition to

the phases mentioned above, some other phases are also reported in Al-Mg-Si alloys, particularly in alloys containing an excessive amount of Si. Three types of phases U1, U2, and B, also referred to as type A, B, and C, are most common at longer heat treatment time or at higher temperatures, and they can coexist with the β-phase upon over-ageing [9,55,59,65].

When Cu is added as a major alloying element, the precipitation process in Al-Mg-Si-Cu alloys becomes quite complex. The normally accepted precipitation sequence [69-86] changes to SSSS → atomic clusters → GP zones → β" → β', Q' → Q-phase. Equilibrium Q-phase is formed as long laths or rods with the long axes parallel to $<001>_{Al}$ directions. The crystal structure is hexagonal with space group of P6, and the lattice parameters c = 0.405 nm and a = 1.04 nm, with 21 atoms in the unit cell [64,69-71]. The structure is very similar to that of Th_7S_{12}, in which Si atoms take the place of Th atoms, Al and Mg atoms replay S atoms, and Cu atoms locate at other sites that are not occupied in the Th_7S_{12} structure [71]. The exact stoichiometry has been found to vary between different studies. First principles atomistic calculations suggest an energetically preferred composition of $Al_3Cu_2Mg_9Si_7$ [69]. Other studies reported compositions of $Al_4CuMg_5Si_4$ [22], $Al_5Cu_2Mg_8Si_6$ [39,72], $Al_4Cu_2Mg_8Si_7$ [71] and $Al_3CuMg_4Si_3$[73], respectively.

It has been claimed that Q' is the coherent version of the equilibrium Q-phase, which is considered to be a precursor of the Q-phase, as shown in Figure 1.8 [74]. The Q'-phase is mainly formed in overaged conditions, and has a lath shape and hexagonal structure (a = 1.04 nm and c = 0.404 nm) with the long axis oriented parallel to the $<001>_{Al}$ directions and $\{150\}_{Al}$ habit planes of the matrix. The Q'- and Q-phases have the same crystal structure with slightly different lattice parameters, and Q' is coherent with the Al matrix along its long axis [75,76]. Matsuda et al. [77] observed a mean chemical composition of $Al_4CuMg_6Si_6$ for Q'-phase precipitates and suggested that the Q'-phase could transform from the β'-phase or nucleate on the interface between the β'-phase and the matrix in an Al-1.0Mg_2Si-0.5Cu wt% alloy. Yassar et al. [78] reported that the Q'-precipitates could be formed by heterogeneous nucleation on dislocations. Transformation from type-C precipitate was also suggested [79]. However, this is only the main precipitation sequence

in Al-Mg-Si-Cu alloys, and the precise precipitation sequence is still not fully understood, due to complex combinations of metastable phases reported in a number of studies, such as L, S, C, QP, QC, which are influenced by the Mg to Si ratio (balanced versus excess), the level of excess Si, and the presence of Cu or the Cu level [72,74,80-82]. The significant strengthening effects in Al-Mg-Si-Cu quaternary alloys by addition of Cu can be attributed to the increase of the density of β”-[74] and β’-phases [83], the precipitation of Q’-phase [83,84] or its lath-shaped precursor phase like L-phase [81,82].

1.3 Recovery and recrystallization

Recovery and recrystallization are two different reasons for the loss of strength through rearrangement and removal of dislocations that are stored in plastic deformation and cause strain hardening, during heat treatment after plastic deformation, known as annealing which usually means keeping the deformed metal for a certain time at a temperature higher than about one-third of the absolute melting point. Recovery and recrystallization may also take place during deformation at elevated temperatures, termed dynamic recovery and dynamic recrystallization, respectively [2,6,10,87].

1.3.1 Recovery and recrystallization during and after hot deformation

Recovery occurs at the early stages of the thermally activated restoration of the inner structure of cold-worked metals without notable changes of the grain and phase topology. Static recovery proceeds by the reorganization of the dislocation substructure, driven by the elastic internal stresses from the preceding plastic deformation and by point defect annihilation, which can be observed at temperatures far below the recrystallization temperature of about 1/3-1/2 of the absolute melting point. During recovery subgrain (boundaries) are gradually formed due to the rearrangement of dislocations. Primary static recrystallization, which follows the recovery stage and competes with it, is characterized by nucleation and nucleus growth into the deformation substructure via the formation and motion of new high-angle grain boundaries. When recrystallization starts, the deformation substructure is already in a recovered state because the recrystallization process requires an incubation period and recovery does not. During primary static recrystallization, the remaining recovered cold-worked structure is replaced by new strain-free and

approximately equiaxed grains. The driving force is provided by the stored deformation energy, i.e. primarily by the long-range elastic stresses associated with the dislocation and subgrain structure that is formed during plastic straining. Following nucleation, grain growth happens, the driving force of which comes from the reduction in the total grain boundary area [2,6,10,87].

The accumulated dislocations can continuously be removed by dynamic recovery and dynamic recrystallization during hot deformation at temperatures above half of the absolute melting point. Dynamic recovery occurs in materials with high stacking fault energy such as Al in a continuous fashion and leads to the gradual mutual annihilation of dislocations by climbing and cross-slip, and the thermally activated formation of subgrains and subboundaries. Dynamic recrystallization may take place when a critical deformation condition is reached in metals in which recovery processes are slow, such as those with a low or medium stacking fault energy, because the accumulated dislocation density is sufficiently high to stimulate the nucleation of recrystallization during hot deformation. This mechanism of dynamic recrystallization consists in the formation of mobile high-angle boundaries that at least partially surround the nuclei and the subsequent sweeping of the deformation substructure that is stored during hot working. However, it has been found that under certain conditions a microstructure of high angle grain boundaries may evolve during high temperature deformation in ways other than the nucleation and growth of grains, which is called continuous dynamic recrystallization. And there are at least two processes which can be classed as continuous dynamic recrystallization: geometric dynamic recrystallization and dynamic recrystallization by progressive lattice rotation [2,6,10,87-97].

1.3.2 Dragging effect of particles on moving grain boundaries

Second phase particles can exert a substantial back driving force on the moving grain boundaries, referred to as particle-pinning force or Zener force, since the presence of second phase particles on the grain boundary reduces the grain boundary area, and hence the grain boundary energy, which must be replenished upon unpinning [6,10,88,98]. Considering pinning effect imposed by a stable array of incoherent particles that reside on

the grain boundaries of the deformed microstructure, assuming that the boundary moves as a straight interface through the particle array, the magnitude of the pinning force (Zener pressure) by randomly distributed spherical particles is approximated by Zener and Smith to be [87,99,100]

$$P_Z = -\frac{3}{2}\gamma\frac{f}{r} \quad (1.2)$$

where γ is the grain boundary energy (in units of J/m^2), f is the volume fraction of spherical particles and r is the particle radius.

1.4 Fatigue damage and crack initiation mechanisms

Fatigue failures in metallic structures are a well-known technical problem. When a metal is subjected to a cyclically variable stress (or strain) of sufficient magnitude (often below the yield stress), a detectable change in mechanical properties is produced, which is called fatigue [101,102]. In practice, a large number of service failures are due to fatigue, and therefore, researches on fatigue failure of materials are highly concerned. Based on the number of stress or strain cycles during fatigue lifetime, fatigue regime is relegated to either a low-cycle fatigue (LCF) regime or a high-cycle fatigue (HCF) regime, between which there is no sharp dividing line. In LCF, stress amplitudes are high, typically over the yield strength, and the cycle loading is always associated with macro-plastic deformation. Whereas HCF is more related to elastic behavior of the material on a macro-scale, in which the stresses applied are just above the fatigue limit [103-105]. As indicated in Figure 1.9, the fatigue life is usually split into three stages: crack initiation, crack growth and final fracture due to unstable crack growth [103]. In the crack initiation period, a fatigue crack nucleus can be initiated on a microscopically small scale under a cyclic load. The crack initiation period is supposed to include some microcrack growth, but the fatigue cracks are still too small to be visible. Following crack initiation period, cracks grow to a macroscopic size, and finally until complete failure [103,104].

1.4.1 Approaches to evaluation of fatigue properties

Traditionally, there are two major approaches to characterize fatigue properties and predict fatigue life of materials, i.e. total-life approach and damage-tolerant approach [101,105]. In total fatigue life approach (S-N curve approach), the number of stress or strain cycles

(fatigue life) necessary to induce fatigue failure in initially uncracked and nominally smooth-surfaced laboratory specimens is estimated under controlled amplitudes of cyclic stresses or strains. In high-cycle fatigue regime, the stress range is used to characterize the number of cycles to failure, whereas the fatigue life is characterized in terms of the strain range in low-cycle fatigue regime. However, large scatter always exists in the measured data due to inherent microstructural inhomogeneities in real engineering components. In defect-tolerant approach, all engineering components are assumed to be inherently flawed, and the size of flaw is generally determined from nondestructive flaw detection techniques. If no cracks are detected, the largest initial crack size is estimated from the resolution of the flaw detection technique. The fatigue life is defined as the number of fatigue cycles or time to propagate the dominant crack from this initial size to some critical dimension, which is predicted using empirical crack growth laws based on fracture mechanics. This approach is too conservative, because only largest flaw is considered for prediction of fatigue life. In addition, the propagation period of crack may cover only small percentage of total fatigue life, making the prediction much less than the reality.

An experimental methodology, considering the effects of microstructures, has been developed by Zhai [106] for quantitative characterization of multi-site fatigue crack initiation behavior in Al alloys, which was well summarized in reference [107]. In this method, four-point bend fatigue tests are conducted under stress or strain control, by which the number of fatigue cracks (weak-links, proposed by Weibull [108]) on the sample surface are measured at different cyclic stress or strain levels. Among all the sigmodal functions, the populations of crack initiation sites (fatigue weak-links) on the surface are found to be appropriately a three-parameter Weibull function of the applied maximum cyclic stress or strain in the alloys, from which the fatigue weak-link density and strength distribution of fatigue weak-links could be calculated. The fatigue density and strength distribution of the weak-links could be regarded as materials fatigue properties, which could be used to quantify the fatigue crack initiation behavior and evaluate the quality of Al alloys. For example, the effects of environment, types of microstructural heterogeneities and loading direction on crack initiation were studied in detail in AA7075 T651 [109], AA 8090 Al-Li [106], AA2026 T3511 [107], A713 alloys [110], etc. It was found that the

anisotropy of fatigue properties in AA8090 Al-Li and AA7075 T651 alloys was due to the difference in grain structure and particles in different planes [106,109]. The strength distribution of fatigue weak-links (pores) was indicated to be more appropriate to be used to evaluate the fatigue crack initiation property of A713 cast Al alloy instead of the simple pore size distribution [110]. It was also revealed that the crack initiation rate density, rather than weak-link density, was more accurate to describe the relationship in the Weibull function. And when the maximum cyclic stress exceeded the yield stress of an alloy, the applied cyclic strain should be used in the Weibull function to quantify the fatigue crack initiation behavior in the alloy [107].

1.4.2 Effects of microstructures on fatigue crack initiation

Under high-cycle fatigue (HCF) loading conditions, the period of crack initiation and propagation of microstructurally short cracks can account for up to 90% of the total fatigue life of a technical component [101,102]. Many factors have been found to influence the initiation of a fatigue crack, such as microstructural effects, geometrical effects, loading conditions, surface effects and environmental effects. In this work, only the effect of the microstructure will be discussed. During fatigue loading, crack initiation is predominantly observed at the surface or subsurface, where local stress-strain concentration occurs, giving rise to local exceeding of the microscopic yield strength, due to the existence of a variety of microstructural inhomogeneities, such as persistent slip bands (PSB), nonmetallic inclusions, second phase particles, pores and grain boundaries.

1.4.2.1 Persistent slip bands

In metals and alloys of high purity, cyclic deformation can lead to crack initiation, if some infinitesimal amount of localized irreversible plastic slip is present. Fatigue often occurs in grains at the material surface at stress levels below the yield strength because cyclic slip in surface grains is less constrained by neighboring grains than in subsurface grains [101-103,111]. During cyclic slip, the plastic deformation is only partially reversible (slip irreversibility), causing a small increment of fatigue damage in each cycle. As a consequence, the permanent slip band (PSB) is formed on the sample surface, leading to micro-crack initiation [101-103,112-114]. Two reasons of the irreversibility have been

mentioned [103,115,116]: (1) adsorption of oxygen to form the oxide monolayer at the fresh metal surface of the emerging slip bands, which cannot simply be removed from the slip step; (2) non-fully reversible strain hardening in the slip band. Wood [117] proposed that during cyclic straining the irreversibility of shear displacements along the slip bands resulted in microscopic 'hills' and 'valleys' at the free surface, which are commonly referred to as 'intrusions' and 'extrusions', respectively, leading to additional slip and fatigue crack nucleation because of the stress concentration by the valleys. The slip-induced surface roughening during fatigue was reported by Forsyth [118] in a solution-treated Al-4 wt% Cu alloy, in which thin ribbons of the metal (0.1 μm thick and 10 μm long) 'extruded' at the specimen surface from the PSBs to trigger microcrack initiation. Using interferometric measurements, it was found by Laird et al. [119] that during the fatigue of Cu single crystals, surface slip steps were formed in proportion to the applied plastic strain with irreversible slip in individual steps. Cheng and Laird [120] observed that crack initiation occurred preferentially at the sites of the PSBs with the highest slip offset and largest strain localization. Protrusion has also been reported to be responsible for fatigue crack initiation in some materials, which is a surface uplift with many micrometers in height and tens of micrometers wide, containing tens of matrix and/or PSB lamellae. Several intrusions and extrusions may be included in a protrusion [101]. Boyce et al. [121] revealed a new level of understanding of the mechanistic role of oxygen in PSB crack initiation during fatigue loading in nickel micro-specimens formed by the LIGA process. Zabett and Plumtree [122] reported formation of cracks at localized slip bands within the largest available surface grains in the T and S direction specimens of 2024-T351 plates, which were narrower in the S direction specimens, facilitating decohesion and leading to earlier microcracking. A model for surface roughening and crack nucleation was developed by Essmann et al. [113] based on the hypothesis that the annihilation of the dislocations within the slip bands was the origin of slip irreversibility. Antonopoulos et al. [123] proposed a model of dislocations at PSB/matrix interfaces by considering a continued increase in the density of vacancy dipoles during fatigue. Tanaka et al. [124] modeled the forward and reverse plastic flow within the slip band by dislocations with different signs moving on two closely located layers based on the assumption that their movement was irreversible to illustrate fatigue crack initiation. The interfaces between PSBs and matrix can also serve as preferential sites

for fatigue crack nucleation. Direct observation of crack nucleation preferentially along the interface between PSBs and matrix has been obtained by Hunsche and Neumann in Cu crystals [114].

1.4.2.2 Second phase particles or inclusions

Constituent particles which are formed during casting and break up and redistribute themselves during subsequent thermo-mechanical processing, such as rolling and extrusion, can lead to initiation and growth of small fatigue cracks either by debonding of the interface between the matrix and particles or by fracture of the particles themselves [101,102,109,122,125-147]. Sigler et al. [125] studied the fatigue crack initiation in an overaged 2024 Al alloy. It was found that most fatigue cracks initiated at β-constituent particles at all stress amplitudes, while crack initiation at S-phase particles was extremely rare and confined almost entirely to the about 95% of the yield strength. In addition, at low stress amplitudes, crack initiation occurred primarily at the interface between β-particles grouped in closely-spaced pairs (cluster sites), produced by the fracture of large particles during rolling. Crack initiation at constituent particles in 7075-T651 has been reported by several researchers [109,126-128]. Jin et al. [109] investigated the fatigue crack initiation in an AA7075 T651 alloy plate. Fatigue cracks were predominantly initiated at Fe-containing particles on the L-T and L-S planes, part of which were pre-fractured during prior rolling, but only at Si-bearing particles on the T-S plane. Harlow et al. [126] observed that Al_7Cu_2Fe particles were predominate crack sites, and the damage mechanism was typically decohesion for Mg_2Si. Payne et al. [127] found that the hard Al_7Cu_2Fe particles acted as effective fatigue crack initiation sites, a majority of which were cracked during the hot rolling process, while the softer Mg_2Si particles were not effective at nucleating cracks. It was revealed by Patton et al. [129] that most of the cracks were initiated by the fracture of intermetallic Al_7Cu_2Fe and Mg_2Si particles, which was favored by twisted cubic texture in 7010-T7651 Al alloys. Mg_2Si/matrix interface decohesion was also detected as minor sites in the alloy. Zabett and Plumtree [122] found that almost all the cracks were observed at Al_7Cu_2Fe second phase particles, which had been broken during prior rolling, in the L direction in 2024-T351 plate specimens. Zheng et al. [130] studied the fatigue crack initiation behavior of AA2524-T34 alloy. It was observed that most of the cracks were

initiated from the second phase particles such as $Al_7Cu_2(FeMn)$, θ (Al_2Cu) and S (Al_2CuMg), or the interface between the particles and the matrix.

Fatigue crack initiation can also occur at nonmetallic inclusions. In the case of the high strength steels, cracks are initiated most frequently at nonmetallic inclusions such as Al_2O_3, MnS or SiO_2 [101-103]. Large Al_2O_3 inclusions tend to crack during cold working or service in steels [102]. In the case of sulfur-containing steels, the initial stage of fatigue damage is the debonding of the inclusion from the matrix. Fatigue crack nucleation due to partial debonding of a MnO-SiO_2-$A1_2O_3$ inclusion from the matrix in a 4340 steel was reported [101]. In high strength P/M nickel-based superalloys AF-115, crack initiation has been identified with the existence of HfO_2 inclusion [101]. Crack initiation from SiC particles was also observed in a SiC-reinforced 8019 Al alloy [102].

1.4.2.3 Grain boundaries (GBs)

Grain boundaries (GBs) can also be one type of fatigue crack initiation sites in alloys [101,102]. Three main ideas to explain the grain boundary (GB) fracture were reviewed in precipitation hardened Al alloys [93]: (1) microvoid growth at large GB precipitates; (2) strain localization in the soft, and sometimes solute-free, GB precipitate free zones and (3) large stress concentrations applied to the GB at the end of slip bands by inhomogeneous "planar" slip given by matrix precipitate shearing. The first process was of overwhelming importance compared with the last two processes, which was tested by Vasudevan et al. [93] in Al-Li alloys, showing that the occurrence of intergranular fracture was associated with microvoids growth at large GB δ-precipitates. Sigler et al. [125] observed that more than 10% of the crack initiation was at grain boundaries at the highest amplitude employed (320 MPa) in an overaged 2024 Al alloy, which was suggested that only at high applied stresses, the local strains caused by irreversible slip were sufficient to open up a crack along the grain boundary. Srivatsan et al. [140] showed that the preferential plastic deformation resulted in a highly localized stress concentration at locations of grain boundary triple junctions, leading to early nucleation of fine microscopic cracks. Zhai [106] found predominant intergranular fracture in S-L and S-T samples of an Al-Li alloy due to the segregation of trace amount of Na and K at grain boundaries when loading in the S direction.

Intergranular crack initiation was also revealed by Davidson et al. [149] to prevail in a nickel-based superalloy at the sites where the grain boundaries were 45 to 60° to the loading axis, the trace of a {111} was within 20° of the GB direction, and the trace of a {111} impinged on the GB at an angle of 72 to 82°. Mulvihill et al. [150] demonstrated that the fatigue crack initiation at GBs resulted from the weakening effect of PFZs surrounding GBs along which a number of equilibrium θ-precipitates were formed in peak-aged Al-Cu alloys at a maximum stress of 80% of yield strength. Krupp [102] summarized two mutual superimposing mechanisms for intercrystalline crack initiation at room temperature, which did not take grain boundary precipitates or segregation effects into account: (1) high normal stresses acting on the grain boundaries locally caused by elastic anisotropy, which may exceed the interfacial cohesion; (2) formation of slip steps by plastic incompatibility, which generates dislocation pairing along the active slip band and/or dislocation pileup at the grain boundaries under planar slip conditions. In addition, transgranular crack initiation can occur if the resistance of the grain boundary to (1) slip transmission (plastic incompatibility) and (2) interfacial separation is sufficiently high to increase the back stress encouraging dislocation pairing and/or dislocations pileup and eventually cause slip band separation.

1.4.3 Effects of porosity on fatigue crack initiation

Pores in metals and alloys could become the predominant fatigue crack initiation sites, in particular when their size falls within the dimension of the most characteristic microstructural feature of the material, e.g., the grain size or the phase distribution in two- or multi-phase materials [1,102]. Microporosity formation is generally attributed to two factors in the cast alloys [1,151]: (1) shrinkage resulting from a lack of interdendritic feeding during solidification (shrinkage pores) and (2) evolution of hydrogen gas bubbles due to a sudden decrease in hydrogen solubility in solid metal compared to the liquid during solidification (gas pores). Shrinkage pores are more like mircocracks often with an irregular three-dimensional shape and sharp corners, which are quite deleterious to fatigue properties; whereas gas pores are usually spherical in shape and less detrimental to fatigue properties than shrinkage pores. Since liquid Al is prone to hydrogen adsorption and oxidation, both types of these pores can be associated with Al oxide films in Al castings.

Fatigue crack initiation is reported to occur preferably at pores that are close to or at the surface [152-165], mainly due to the high stress/strain concentration adjacent to the pores, as shown in Figure 1.10. Decreasing the size of pores could lead to the increase of the fatigue life [159,160,162,163]. In the study of Chan et al. [153], fatigue cracks were found to be initiated at shrinkage pores with sharp radii of curvature in the B319-T6 alloy, which appeared to have a high stress concentration factor. Large rounded gas pores were also observed, but they did not initiate any fatigue cracks due to a lower stress concentration factor. Zhu et al. [152] observed that in E319 cast Al alloy fatigue cracks were predominantly initiated from large pores located at or very near to the specimen surface. Yi et al. [161] identified only large pores close to the specimen surface as the major initiators of fatigue cracks in the examined A356-T6 castings. The resultant fatigue life was also related to the initiating pore size through a relationship based on the rate of small-fatigue-crack propagation. Wang et al. [154] reported that the fatigue cracks were initiated from porosity and oxide films located close to or at the specimen surface in Sr modified cast A356 alloy, with more detrimental effect on fatigue life for porosity. By reducing the pore size until a critical defect size ~25 μm, fatigue life was increased, below which the fatigue cracks were initiated from other intrinsic initiators such as eutectic particles and slip bands. In the study of the effect of porosity on the fatigue life of LP PM319-F and A356-T6 alloys, Ammar et al. [160] demonstrated that 92% of all tested specimens fractured because of surface porosity acting as a crack initiation site. The fatigue life of the sample decreased as surface pore size increased, which was consistent with Couper's observations in CP601 cast Al alloy, in which the reduction of the pore size below ~15 mm did not further improve the fatigue life due to initiation from PSBs became operative [30]. In addition, Stanzltschegg et al. [166] found that a reduction of the number of casting pores could lead to a higher number of cycles necessary for crack initiation in $AlSi_7Mg$ cast alloy. However, some experimental results showed that fatigue cracks were not necessarily initiated from the larger pores on or near to the surface [162]. It was observed that smaller pores, ~10 μm in diameter, on the surface or below surface could still cause crack initiation in an A713 sand cast Al alloy, indicating that the strength distribution of fatigue weak-links, instead of the simple pore size distribution, should be used to evaluate the fatigue crack initiation property of the alloy.

1.4.4 Modeling of crack initiation from pores using finite element analysis

Finite element analysis was previously used to analyze the effects of pore size, position, shape and clustering on stress/strain concentration and crack initiation in Al alloys [157,165]. Gao et al. [156] conducted high cycle fatigue tests on cast A356-T6 alloys, showing that the pore size and proximity to the specimen surface significantly influenced fatigue crack initiation, which was supported by finite element analysis (FEA), demonstrating that high stress/strain concentration was induced by pores with idealized geometries, which were both large and near to the specimen surface, as shown in Figure 1.11. Similar results were also obtained in A356-T6 alloys [157,161] that a large pore close to the surface was more likely to initiate a fatigue crack due to the higher induced stress and accumulated plastic strain, using both experiments and finite element analysis. The effects of pore position in depth, pore orientation, pore size and pore clustering on the stress field around a pore (pores) was studied by Xu et al. [165] in a cast 713 Al-Zn alloy using finite element modeling. It was found that the stress and strain concentrations increased sharply when a pore intercepted the free surface or with the decrease in distance between two pores in the surface. By tilting an elongated (ellipsoidal) pore in the surface, the stress/strain was further increased. Increasing the pore size could only increase the zone of high stress/strain concentration around the pore in the surface. Yang et al. [167] developed a quantitative 3-D pore-sensitive model, taking into account the 3-D effects of pores on fatigue crack initiation in an A713 cast Al alloy. In the model, the relationship of the fatigue crack incubation life with the pore position and size was analyzed by a 3-D finite element analysis. The fatigue weak-link density and strength distribution as a function of the applied cyclic stress was consequently quantified by the 3-D pore-sensitive model, which was validated by the experimentally measured results in the alloy. The influence of pore size, spacing, and clustering on fatigue crack incubation has been analyzed by Fan et al. [155] using an FEM-based micromechanical approach. The local maximum plastic shear strain range, regarded as the driving force for fatigue crack formation [168], was used to estimate the cycles to crack incubation using the Coffin-Manson equation. It was revealed that larger pores and smaller pore spacing led to higher strain concentration and lower fatigue crack incubation life, with a competition between the effects of pore size and spacing on plastic strain intensification. The plastic strain intensification effect was found

to be sensitive to the applied stress level in particular at stress amplitudes below macroscopic yielding. The driving force for fatigue crack formation from damaged inclusions and pores in cast A356 Al alloy was quantified by Gall et al. [168], considering both idealized circular and realistic shaped inhomogeneities in the finite element study. It was found that the shape of inclusions or voids had a relatively small effect on the driving force compared to other critical effects such as size, damaged state, and reversed plasticity. McDowell et al. [169] applied a HCF model to cast A356-T6 alloy with various types of inclusions, ranging from individual Si particles to large shrinkage pores and trapped oxide films, which was capable of predicting the variability of fatigue life for realistic ranges of solidification rates, hydrogen gas levels, and resulting microstructures. The morphological assessment of porosity coupled with finite element analysis (FEA) has been increasingly used to investigate the correlations between defect geometry, stress concentration and crack initiation [170,171]. For example, an accurate methodology has been developed to identify local stress concentration on the contour of casting pores in high Fe-content Al-Si-Cu alloys [170]. Micro-computed tomography (μ-CT) was applied to reconstruct the morphology of pores which was converted into a 3-D volumetric model to be used as an input for linear finite element analysis (FEA) with the aim of investigating the structural influence of these defects. It was indicated that particularly holes in the shape of shrinkage pores acted as stress concentrators and could thus be identified as hot spots.

1.5 Motivation of the study

Currently, the primary issue in automotive industry is to further decrease the weight of vehicles to improve the automobile fuel-efficiency and performance. This can be accomplished by development of light-weight, low-cost, and high-performance materials. 6xxx series Al alloys are considered as one of the most significant automobile materials due to their high specific strength, excellent formability, corrosion resistance, and low cost, etc. 6xxx series Al alloys have been already substantially used in the automotive applications to substitute steel or conventional Al alloy components worldwide. For example, Kobelco has developed 6xxx series Al alloys with high strength and high ductility, such as KS651 alloy with the yield strength of 340 MPa and fatigue strength of 135 MPa, and more recently KD610 alloy with the yield strength of 380 MPa and the fatigue strength

of 150 MPa, by controlling alloy composition and thermomechanical processing. However, the yield and fatigue strengths of the 6xxx series Al alloys might be further enhanced by further optimizing the alloy composition, microstructure and thermomechanical processing, which could only be achieved by thorough understanding of the formation mechanisms of all the phases in the alloys.

In 6xxx series Al alloys, addition of transition elements of Mn and Cr could promote formation of fine α-Al(MnCrFe)Si dispersoids which inhibit recrystallization, thereby leading to fine grain structure by forming a large volume fraction of subgrains during thermomechanical processing. Grain refinement could enhance both strength and toughness of these alloys. The dispersoids are usually formed during ingot homogenization. It is therefore desirable to optimize the density and distribution of the dispersoids in order to retard recrystallization to refine the grain structure effectively in the alloys. This can only be done by fully understanding the formation mechanism of these dispersoids. Although these dispersoids have been extensively studied before, their formation mechanism is still not fully understood, which is still a challenge for the researchers to make efforts. In addition, although studies of fatigue crack initiation in 6xxx series Al alloys have been carried out, the quantitative analysis of its correlation with microstructure is still scare and far from satisfaction.

This research work therefore is focused on the formation mechanism of these dispersoids and their effects on the mechanical properties, especially the fatigue properties, of the 6xxx series Al alloys. In this study, STEM and 3-D APT techniques were employed to try to reveal the formation process of α-dispersoids in Mn and/or Cr-containing AA6061 Al alloys during high temperature annealing. Also, the effects of various homogenization parameters on dispersoids formation and their inhibiting effect on recovery and recrystallization during hot deformation were investigated. In the meantime, an attempt was made to qualitatively/quantitatively explain the relationship of the fatigue crack initiation with microstructure (mainly pores) in these alloys using four-point bend fatigue tests and finite element analysis (FEA).

Table 1.1 Designation systems for Al alloys [1]

Wrought Aluminum Alloys		Cast Aluminum Alloys	
Alloy Series	Description or Major Alloying Element	Alloy Series	Description or Major Alloying Element
1xxx	99.00 Minimum Aluminum	1xx.x	99.00 Minimum Aluminum
2xxx	Copper	2xx.x	Copper
3xxx	Manganese	3xx.x	Silicon plus Copper and/or Magnesium
4xxx	Silicon	4xx.x	Silicon
5xxx	Magnesium	5xx.x	Magnesium
6xxx	Magnesium and Silicon	6xx.x	Unused Series
7xxx	Zinc	7xx.x	Zinc
8xxx	Other Elements	8xx.x	Tin
9xxx	Unused Series	9xx.x	Other Elements

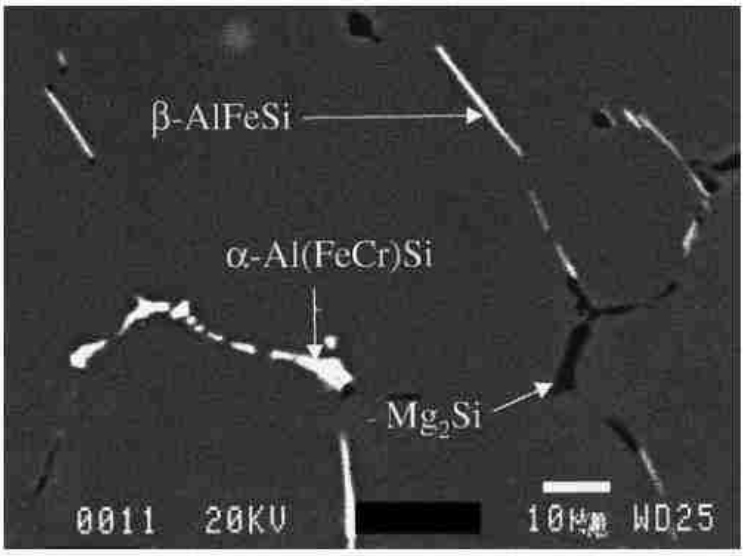

Figure 1.1 Different constituent phase particles formed during casting in a Cr-containing AA6005 Al alloy [20].

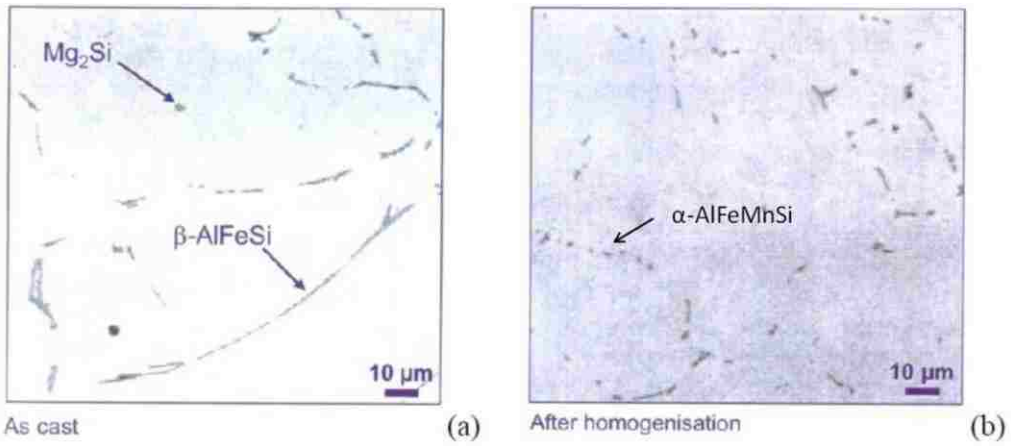

Figure 1.2 Morphological change resulting from β-phase to α-phase transformation in an AA6060 Al alloy (a) before transformation and (b) after transformation [28].

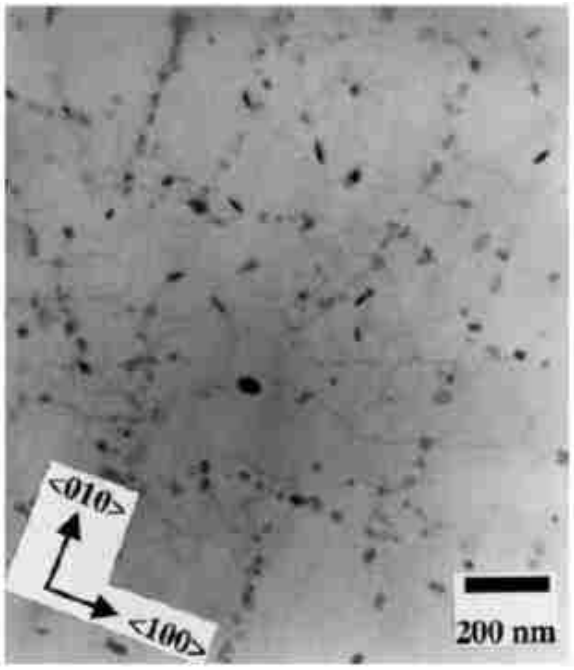

Figure 1.3 TEM micrograph of formation of Mn and Cr-bearing dispersoids during homogenization of an Al-Mg-Si alloy [45].

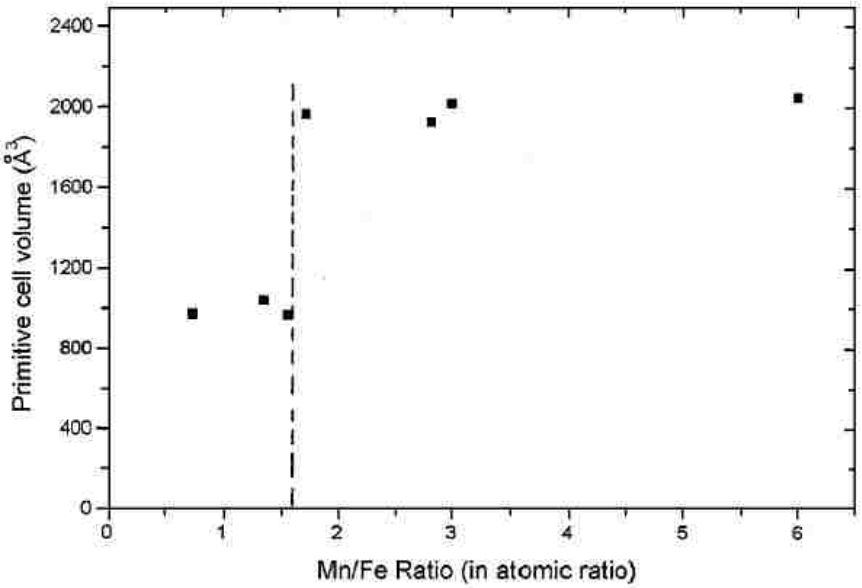

Figure 1.4 Primitive cell volume versus Mn/Fe ratio of dispersoids in an Al-Mg-Si alloy [50].

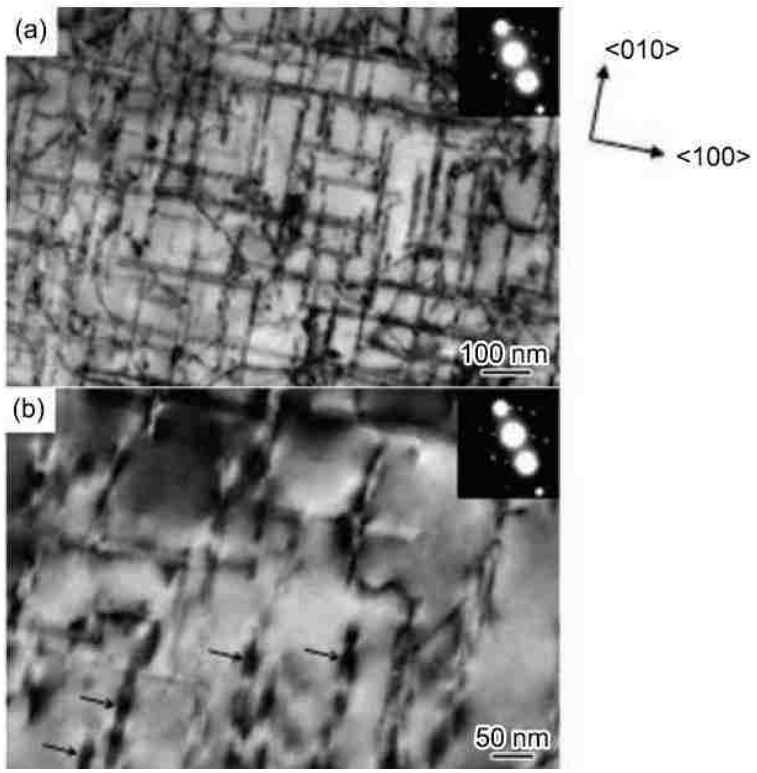

Figure 1.5 TEM micrographs of an AA6082 Al alloy. (a) β'-Mg2Si phase aligned to <100> directions of the matrix; (b) arrows indicate Mn-containing dispersoids on β'-Mg2Si phase [48].

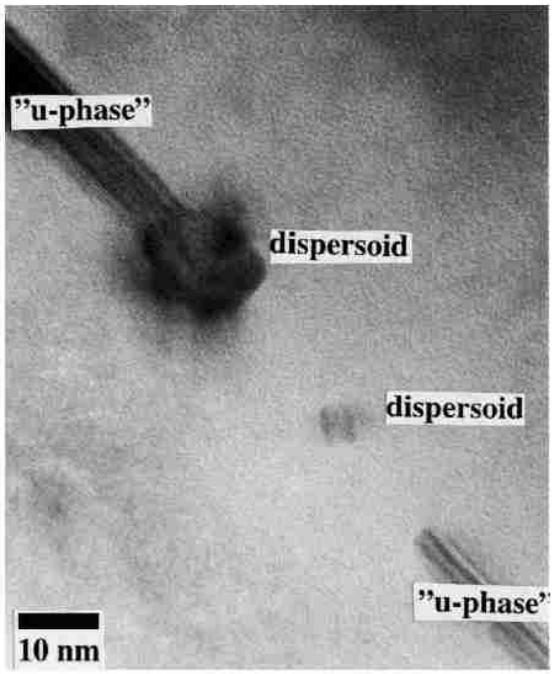

Figure 1.6 TEM bright-field micrograph of a dispersoid that nucleated on the surface of 'u-phase' precipitate [45].

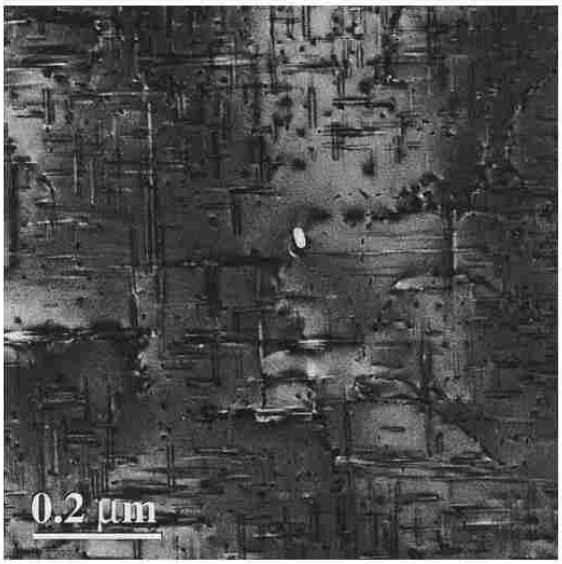

Figure 1.7 A typical low magnification micrograph of β"-needles in a $<001>_{Al}$ zone axis [18].

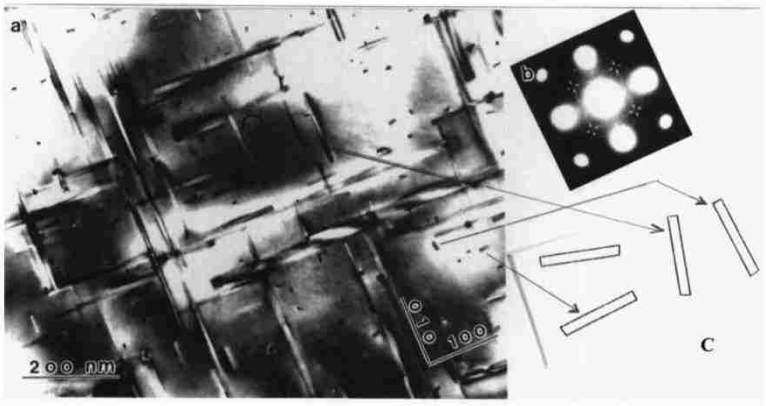

Figure 1.8 TEM micrograph of Q'-phase precipitates [74].

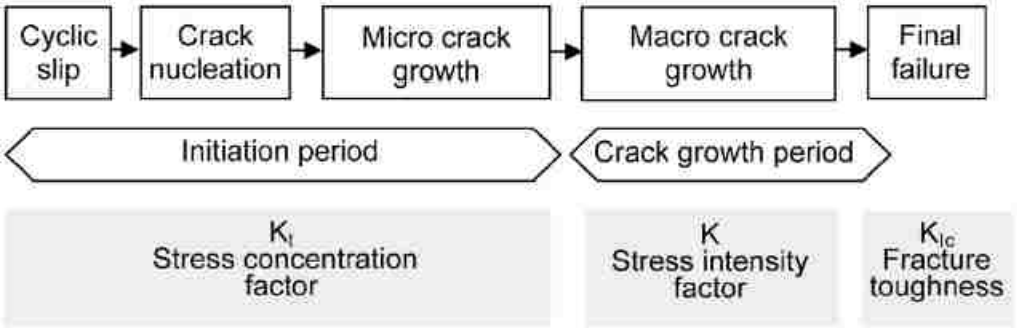

Figure 1.9 Different phases of the fatigue life and relevant factors [103].

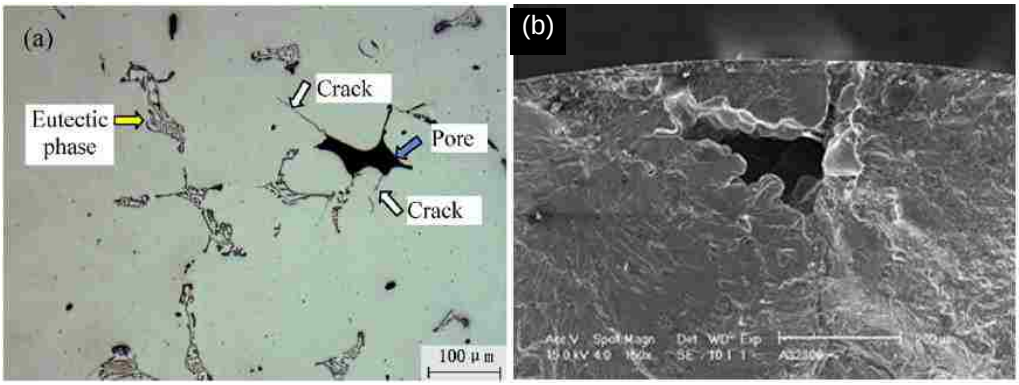

Figure 1.10 Typical fatigue crack initiation pores in (a) A713 [162] and (b) E319 cast Al alloys [152].

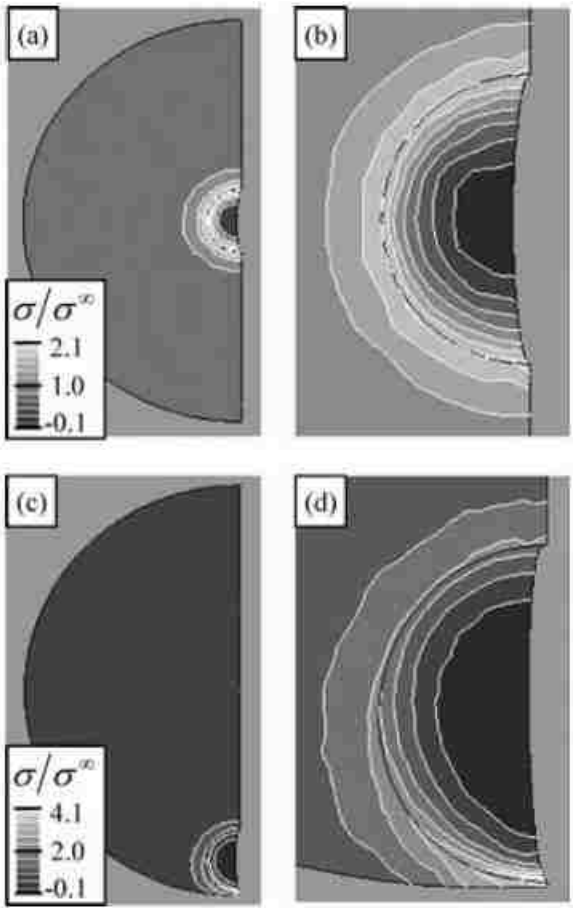

Figure 1.11 Pore-location effect showing the stress concentration around the pore on a cross section. (a) Global and (b) local views of a central pore (D = 800 μm); (c) global and (d) local views of a pore close to the surface (D = 800 μm) [156].

Chapter 2 Experimental methods and theory

2.1 Main experimental methods

2.1.1 Four-point bend fatigue testing

A self-aligning four-point bend testing rig was made and used to study the fatigue behavior of alloys in this research work whose sample and loading geometries are shown in Figure 2.1 [172]. A ceramic semi-sphere is used as a joint between the upper extension bar and the loading plate, which can effectively minimize the misalignment between the two extension bars, leading to uniform loading on a specimen. Two sample pins are designed to position the sample with a diameter slightly smaller than that of the pin holes at the ends of the specimen to avoid possible contact, and thus noticeable friction, between the sample and the two pins during fatigue tests. In addition, two support rollers are used to prevent sample drifting during fatigue, which are located in the grooves (3 mm apart) with varied spacing to meet the testing requirements. The grooves are curved in shape with a diameter slightly larger than 3 mm. The optimum testing geometry has been found to be load-span/specimen thickness ratios (t/h) = 1.2 - 1.5 and support-span/load-span ratios (L/t) = 4 - 5 through finite element modeling verified by experimental work, which gives a uniform stress distribution between the inner-rollers in the sample during four-point bend testing. In this work, the sample dimension of two modified AA6061 Al alloys was 36.5×10×4.7 mm^3. The fatigue tests were conducted on an Instron 8802 testing machine (Figure 2.2), with a sinusoid wave form at f = 20 Hz, stress ratio R = 0.1 and room temperature in air.

2.1.2 Transmission electron microscopy (TEM)

Transmission electron microscopy (TEM) is a microscopic technique in which an image is formed from the interaction of the electrons with the sample as the e^--beam is transmitted through the specimen, which has the ability to not only image microstructures and defects at the micro- and nano-scales, but also use diffraction to gain information about crystal structure, crystallography, lattice parameters of the constituent phases in the microstructures [2,6,173,174]. A very basic system for a TEM is shown schematically in Figure 2.3. There are two modes of operation - imaging and diffraction in TEM, and the corresponding ray diagrams are illustrated in Figure 2.4. When the Bragg conditions are

satisfied at certain angles between electron beams and crystal orientation, constructive diffraction and thus strong electron deflection occur. Diffraction pattern can be generated in the back focal plane by adjusting the magnetic lenses such that the back focal plane of the lens rather than the imaging plane is placed on the imaging apparatus. By using a parallel beam of electrons and defining the particular area of interest with a selected area aperture, selected area diffraction patterns (SADPs) are obtained that not only generate diffraction images but also provide information about the crystal structure producing an image that consists of a pattern of dots in the case of a single crystal, or a series of rings in the case of polycrystalline specimens. Through the insertion of an objective aperture in the back focal plane, i.e., in the plane in which the diffraction pattern is formed, either the directly transmitted beam or a strong diffracted beam is selected to form images (diffraction contrast). If only the transmitted beam is allowed to contribute to the final image by inserting a small aperture in the back focal plane to block the strongly diffracted ray, the contrast is shown on a bright background and is known as bright-field imaging. Whereas, if the diffracted ray is only allowed through the aperture by tilting the incident beam, the contrast on a dark background is observed, known as dark-field imaging. These two arrangements are shown in Figure 2.5. Scanning transmission electron microscopy (STEM) is a type of TEM, which operates by scanning a sharply focused electron beam across the specimen in a raster pattern, while simultaneously collecting various signals for image magnification and/or chemical analysis, synchronized with beam position. Figure 2.6 shows a schematic diagram of the electro-optical configuration used when operating the microscope in an STEM condition. Most STEM microscopes have a two-condenser lens system; however, some newer systems are available with a three-condenser lens system. The scanning of the beam across the sample makes STEM suitable for analytical techniques such as Z-contrast annular dark-field imaging, energy-dispersive X-ray spectroscopy (EDX) and electron energy loss spectroscopy (EELS). These signals can be obtained simultaneously, and direct correlation of image and spectroscopic data can be achieved. The directly interpretable Z-contrast images in STEM are used to form atomic resolution images with a high-angle detector, which afford improvements of spatial resolution compared with the conventional TEM. A Hitachi 3300 scanning transmission electron microscope (STEM) was employed in the current study.

2.1.3 3-D Atom probe tomography (3-D APT)

3-D APT is the three-dimensional atom probe microscopy offering extensive capabilities for both 3-D imaging and quantification of individual chemical species at the atomic scale (around 0.1 - 0.3 nm resolution in depth and 0.3 - 0.5 nm laterally), which is a natural complement to other major microscopy techniques such as transmission electron microscopy (TEM) [2,6,175-177]. 3-D APT provides the highest available spatial resolution for chemical analysis and becomes an essential tool to study nano-scale phenomena in well-equipped laboratories. The atom probe combines a time-of-flight mass spectrometer with a point projection microscope capable of atomic-scale imaging. Combining this with position sensing in the 3-D APT permits the full three-dimensional reconstruction capabilities of APT. The sample is prepared in the form of a very sharp tip commonly through electropolishing or FIB milling. At cryogenic temperatures, a high electric field (~1010 V/m), just below the point of atom evaporation, is created on the apex of a sharp (<100 nm radius) tip by applying a high voltage (~10 kV). Under short laser or HV pulsing, atoms on the specimen apex are field evaporated as ions and accelerated toward the imaging detector with very high detection efficiency (Figure 2.7). By pulsing the evaporation, the flight time of each ion can be measured and used to calculate the mass-to-charge ratio and thus determine its chemical nature. The original position of atoms on the specimen apex is determined from the hit position of the ions on the detector, while the sequence of evaporation events is used to provide depth information. By repeating this process, the atoms are progressively removed from the tip, and 3-D images of the element distributions can be reconstructed with near-atomic resolution. In this work, a local electrode atom probe CAMECA LEAP 4000SI ® was used, and reconstruction and analysis of APT data was conducted using Integrated Visualization and Analysis Software IVAS®3.6.8.

2.1.4 Scanning electron microscopy (SEM)

Scanning electron microscopy (SEM) is a type of electron microscopic techniques to image a sample by scanning it with a high energy beam of electrons in a raster scan pattern [2,174,178,179]. A diagram of the scanning electron microscope (SEM) is shown in Figure 2.8. The electrons interact with the atoms that make up the sample and produce signals that

contain information about the sample's surface topography, composition and other properties such as electrical conductivity. The types of signals produced by an SEM include secondary electrons (SEs, E ≈ 100 eV), backscattered electrons (BSEs, with E ≈ 30 kV which is the incident energy), characteristic X-rays, etc. Due to the low energy of secondary electrons, they can be bent around corners and give rise to the topographic contrast. Secondary electron detectors are common in all SEMs, and the signals result from interactions of the electron beam with atoms at or near the surface of the sample. In the most common or standard detection mode, secondary electron imaging, the SEM can produce very high resolution images of a sample surface, revealing details less than 1 nm in size. Backscattered electrons (BSEs) are beam electrons that are reflected from the sample by elastic scattering. BSEs are often used in analytical SEM along with the spectra made from the characteristic X-rays. Because the intensity of the BSE signal is strongly related to the atomic number (Z) of the specimen, BSE images are particularly important in showing contrast from changes of composition in the sample. The Magnification in a SEM can be controlled over a range of up to 6 orders of magnitude from about 10 to 500000 times. Energy-dispersive X-ray spectroscopy (EDS or EDX) is an analytical technique used for the elemental analysis or chemical characterization of a sample. Its characterization capabilities are due in large part to the fundamental principle that each element has a unique atomic structure allowing X-rays that are characteristic of an element's atomic structure to be identified uniquely from one another. The EDX system is usually equipped with SEM, which can provide detailed information on the μm scale. In the present work, SEMs Hitachi S-4300 and Zeiss EVO MA10 were employed.

2.2 Other experimental methods

2.2.1 Optical microscopy (OM)

Optical microscopy was used to observe the microstructures and fatigue cracks of the modified AA6061 Al alloys on an Olympus PME microscope with the magnifications of 50, 100, 200 and 500 times. For metallographic examinations, the samples were ground with SiC abrasive papers in a sequence of 400, 600, 800, and 1200 grits, followed by mechanically polishing using Alumina (Al_2O_3) powders in sizes of 1, 0.3 and 0.05 μm and colloidal silica suspension.

2.2.2 Electron backscattered diffraction (EBSD)

Electron backscattered diffraction (EBSD) has become a powerful technique used on SEM to obtain crystallographic information for samples without too much prior preparation [180,181]. When an electron beam strikes a tilted crystalline sample (usually 70˚ to the fluorescent screen), a diffraction pattern can be formed by the diffracted electrons, which is recorded with a charge coupled device. Incident electrons which are scattered by atoms in the surface part of the sample with a small energy loss are called inelastically scattered electrons. Through the Bragg diffraction of the inelastically scattered electrons by crystallographic planes in the sample, a Kikuchi pattern [182] is produced on the fluorescent screen, which can be used to analyze the crystal structure and orientation, grain boundary misorientations and local crystal rotations in the sample. When the electron beam is scanned in a grid across a polycrystalline sample, the preferred orientation or texture can be shown by measuring the orientation at each point, which nowadays is fully automated analyzed by image recognition computer algorithms. In this study, EBSD work was carried out on a JEOL JSM-6480 SEM, equipped with a CCD camera and a Channel EBSD system. Data was analyzed using the software provided by TexSem Lab Inc.

2.2.3 Electron probe microanalysis (EPMA)

Electron probe microanalysis is used primarily for the non-destructive elemental analysis of micron-sized volumes at the surface of solid materials with sensitivity at the level of ppm on a micro-analyzer [6]. EPMA works by bombarding a micro-volume of a sample with an electron beam (typical energy = 5 - 30 keV), emitting X-rays at wavelengths characteristic to the elements being analyzed. It is fundamentally the same as SEM, but differs in that it is equipped with a range of crystal spectrometers that enable quantitative chemical analysis (WDS) at high sensitivity. EPMA provides much better results than standard SEM/EDS systems, which gives very flexible sample inspection with image magnification ranging from 40 to 400000. The spectral resolution and detector dead time of EPMA are much better than EDS. In the current work, FE-EPMA JEOL JXA-8530F was used.

2.2.4 Tensile and hardness testing

Hardness testing was carried out on a Vickers tester (HVS-1000) with 100 g load and 15 s dwell time according to GB/T4340.1-2009 standard [183]. At least five indents were made for each specimen tested. Tensile tests were carried out on a CSS-44100 Materials testing machine operated at a constant crosshead speed with an initial strain rate of 5×10^{-4} s^{-1}. The tensile specimens were machined perpendicular to the forging direction based on GB/T228.1-2010 standard [184] with the gauge length of 25 mm, as illustrated in Figure 2.9. Three specimens were tested for each alloy and the average value was taken.

2.2.5 Electrical conductivity measurement

Electrical conductivity measurements give insight in the solid solution levels in the Al alloys. Electrical conductivity of Al alloys can be measured by a so-called Eddy current instrument. The Eddy currents are induced by a time varying magnetic field and are measured by a probe (electromagnet) [185].

2.3 Numerical modeling by finite element analysis (FEA) and Matlab

The finite element method is a numerical method for solving problems of engineering and mathematical physics [186]. When solving problems involving complicated geometries, loadings, and material properties, analytical mathematical solutions are not usually obtainable, and therefore, numerical methods, such as the finite element method need to be employed for acceptable solutions, resulting in a system of simultaneous algebraic equations for solution. In the finite element method, the modeled body is divided into an equivalent system of smaller bodies or units (finite elements) interconnected at nodes and/or boundary lines and/or surfaces. To obtain the solution of the entire body, the equations for each finite element are formulated and then combined. MATLAB is a widely used powerful language for technical computing, whose basic data element is a matrix (array), and can be used for math computations, modeling and simulations, data analysis and processing, visualization and graphics, and algorithm development [187]. In MATLAB program, common problems can be solved by tools (functions), and to solve specific types of problems, optional toolboxes that are collections of specialized programs

are designed. In the present work, the softwares of ABAQUS 6.13 and Matlab R2018a were used.

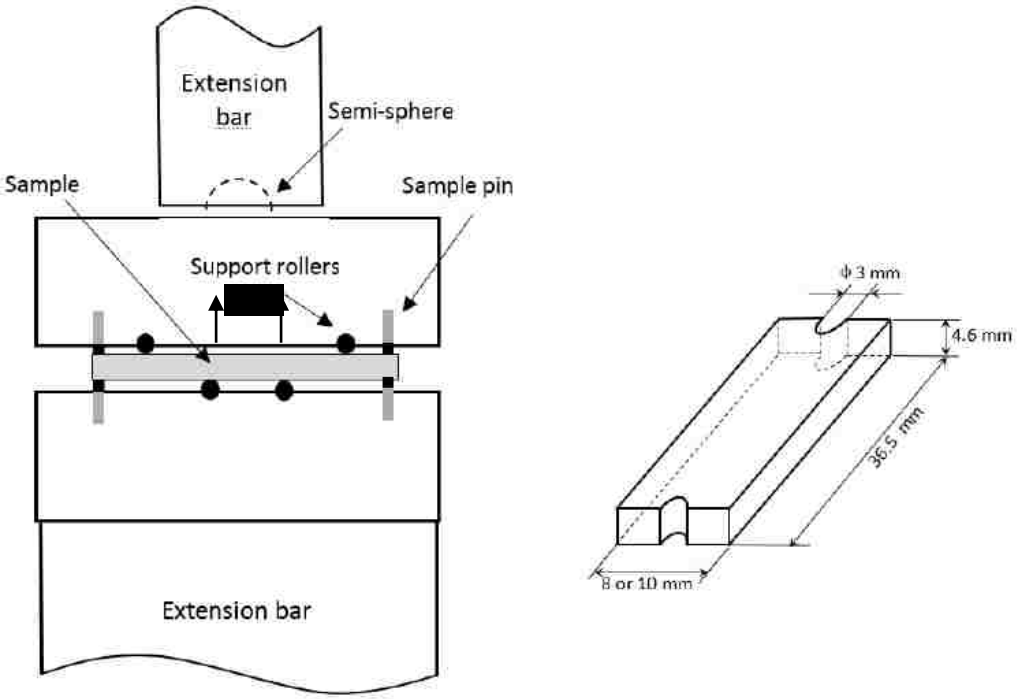

Figure 2.1 A self-aligning four-point bend fatigue testing rig and the geometry and dimensions of a four-point bend sample.

Figure 2.2 Instron-8802 testing machine for four-point bend fatigue tests.

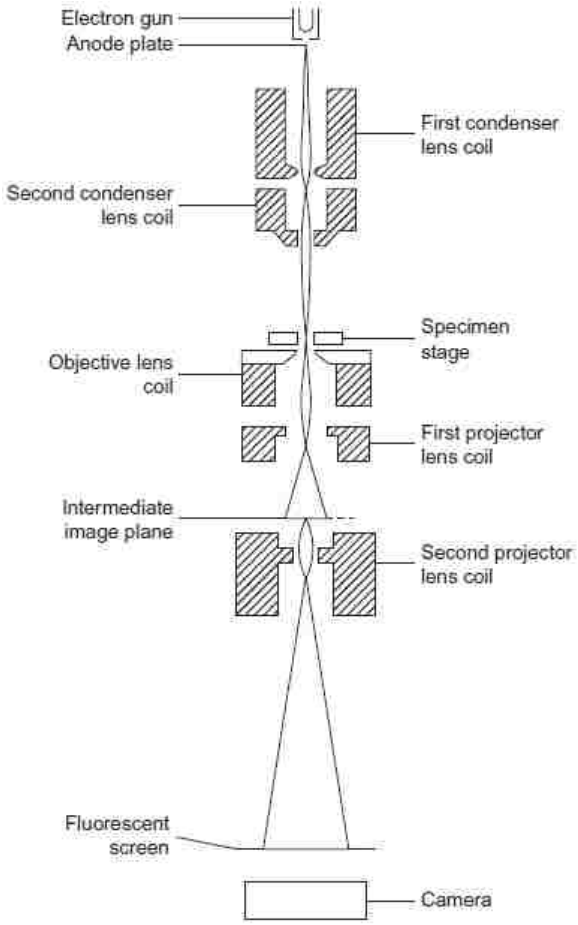

Figure 2.3 Schematic arrangement of a basic TEM system [2].

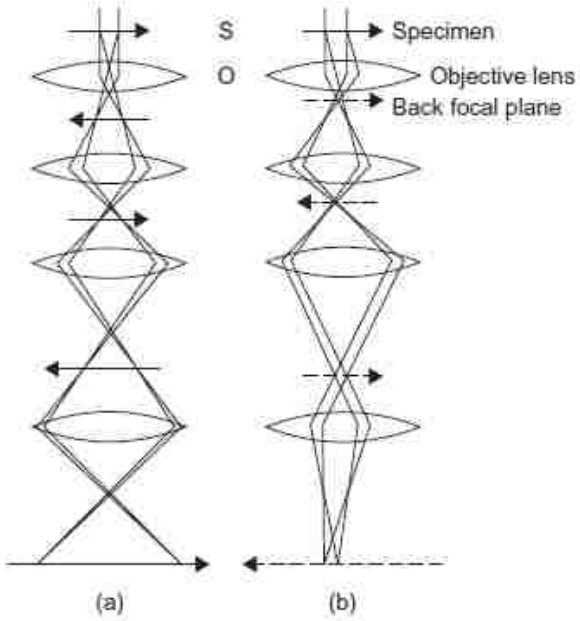

Figure 2.4 Schematic ray diagrams for (a) imaging and (b) diffraction modes in TEM [2].

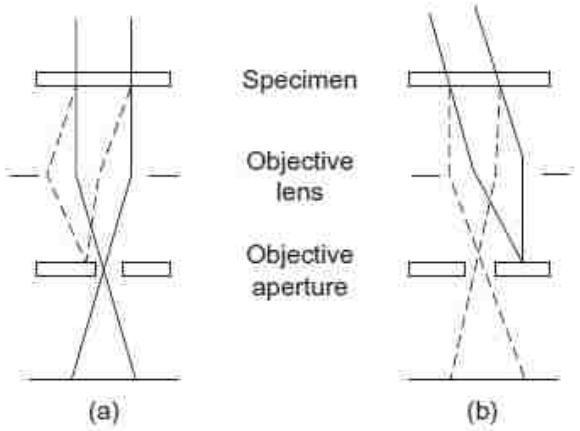

Figure 2.5 Schematic diagram illustrating (a) bright-field and (b) dark-field image formations [2].

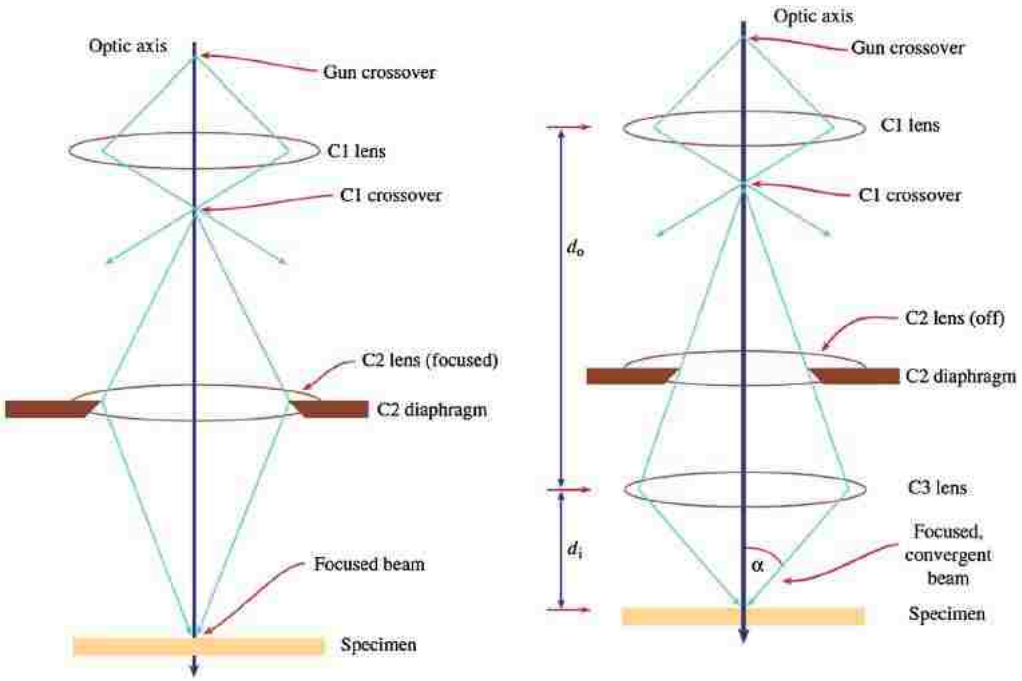

Figure 2.6 A schematic diagram of the electro-optical configuration used when operating the microscope in STEM condition [173].

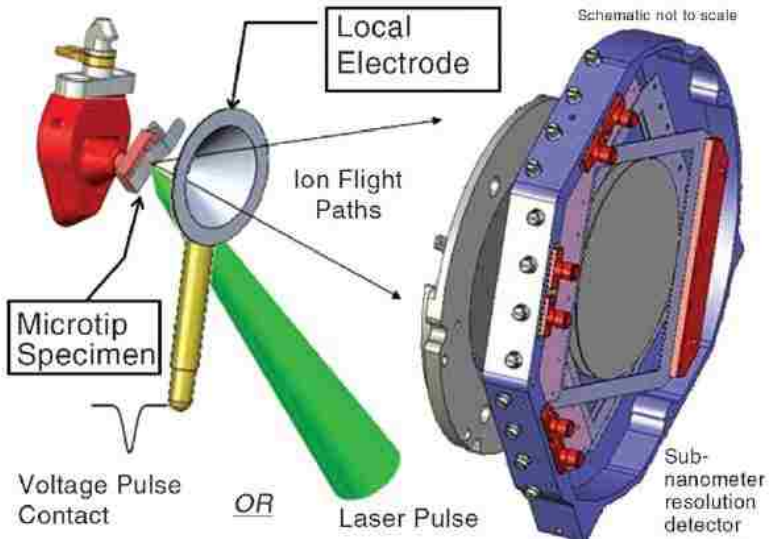

Figure 2.7 Schematic diagram of a local electrode atom probe [175].

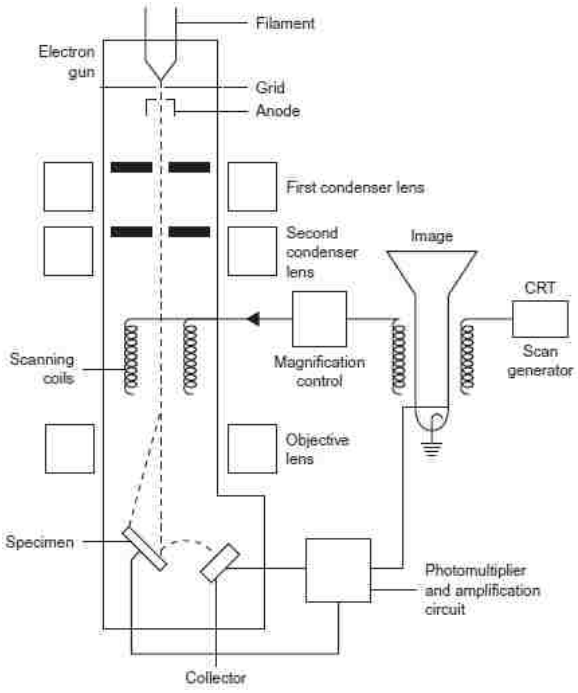

Figure 2.8 Schematic diagram of a basic SEM [2].

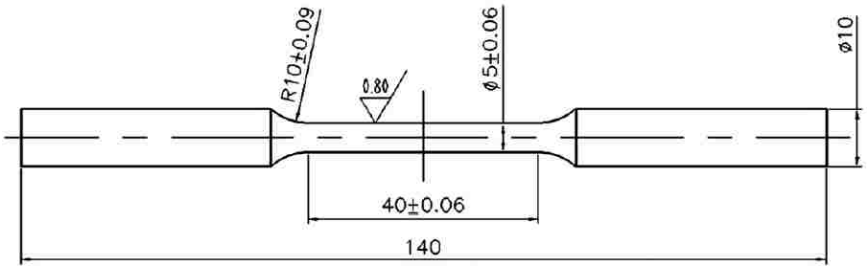

Figure 2.9 Schematic diagram of the tensile specimen.

Chapter 3 Effects of different homogenization treatments on dispersoid formation in modified AA6061 (Al-Mg-Si-Cu) Al alloys

3.1 Introduction

The formation of α-dispersoids depend mainly on the homogenization treatment of cast Al alloys, and partially on the amount of transition metal [53]. Therefore, a better understanding of the precipitation behavior of the dispersoids is crucial to optimize the chemical compositions, homogenization treatments and thus mechanical properties of the alloys. Hu et al. [48] investigated the effect of heating rate on the size and distribution of α-dispersoids in an AA6082 Al alloy. It was observed that a rapid heating rate produced large needle-shaped dispersoids with heterogeneous distribution, while a slow heating rate produced homogeneously distributed fine spherical-shaped dispersoids. Lodgaard and Ryum [45] reported that in order to obtain a uniform dispersoids distribution in studied Al-Mg-Si alloys, it was necessary to heat with a low heating rate from a fairly low temperature ($T < 250\ ^{\circ}C$) to the annealing temperature. The work of Strobel et al. [53] showed that increasing the homogenization temperature and time led to a reduction of the number density and an increase in the size of the dispersoids in AA6082 Al alloy. In 3xxx (Al-Mn) series Al alloys, α-dispersoids prefers to precipitate when the Si level is high. The influence of alloying elements (Si and Mn), annealing temperature and annealing time on the precipitation behavior of α-dispersoids during homogenization treatments has been studied by Li et al. [15,188] in AA3xxx Al alloys with varying compositions of Mn and Si. The evolution of size, size distribution and number density of dispersoids has been quantitatively evaluated. However, despite the effects of different homogenization parameters on the formation of α-dispersoids have been reported, there is still a lack of systematical study regarding these influences, especially in AA6061 Al alloys with the addition of Mn and Cr. These have greatly limited our capability in engineering the size and distribution of the dispersoids in order to effectively inhibit recrystallization and optimize the mechanical properties of the alloys.

In this chapter, the effects of heating rate, Mn content, low temperature pre-nucleation treatment and homogenization temperature on the formation of α-dispersoids during

homogenization in modified AA6061 Al alloys with the addition of Mn, Cr and Cu have been investigated with the employment of STEM. The dispersoids size, size distribution and number density of dispersoids after different annealing treatments were quantitatively measured using the image analysis software Image-Pro on the STEM micrographs.

3.2 Experimental details

Three DC-cast ingots of Mn and Cr-containing Al-Mg-Si-Cu alloys, with 127 mm in diameter and 1500 mm in length, were produced by Suzhou Research Institute for Nonferrous Metals, China, which were then machined to cylindrical billets with 100 mm in diameter and 250 mm in length. The nominal chemical compositions of the alloys with different amounts of Mn are listed in Table 3.1. The cast alloy samples were heat treated in air from 350 $^{\circ}$C up to annealing temperatures of 460 and 540/560 $^{\circ}$C with different heating rates (direct-heating, 6 $^{\circ}$C min^{-1} and 0.6 $^{\circ}$C min^{-1}). At the annealing temperatures, the samples were kept for 4 hours and subsequently quenched by water. To investigate the pre-nucleation effect, another sample was isothermally annealed at 350 $^{\circ}$C for 2 hours before heating to 560 $^{\circ}$C.

Optical microscopy, electron probe microanalysis (EPMA) and scanning electron microscopy (SEM) with an energy dispersive spectroscopy (EDS) system were employed to investigate the microstructures in the as-cast and homogenized samples. Electrical conductivity measurement was performed on the alloys after 4 hours of homogenization between 460 and 550 $^{\circ}$C. For metallographic examination, the sample surface was ground with water proof abrasive SiC papers gradually from grit 240 to 1200, followed by mechanical polishing using alumina powders (1 μm, 0.3 μm and 0.05 μm in size) and colloidial silica suspension. Some homogenized samples were then etched with Keller's reagent for 15 seconds to observe the formation of dispersoids. Scanning transmission electron microscopy (STEM) was employed to study the effects of heating rate, Mn content, low temperature pre-nucleation treatment and homogenization temperature on the formation of α-dispersoids during homogenization on a Hitachi 3300 scanning transmission electron microscope operated at 300 kV. TEM thin foils (3 mm in diameter) were prepared by mechanical grinding before twin-jet electropolishing in a Struers

TenuPol-5 machine. The electropolishing was conducted at -10 °C and 20 V in an electrolyte containing 70% methanol and 30% nitric acid. Energy dispersive spectroscopy (EDS) attached to the STEM was used to measure the composition of the dispersoids. The thickness of the local area of TEM foils, where images of dispersoids were taken, was measured by the electron energy loss spectroscopy (EELS) technique to calculate the number density of α-dispersoids. The size and number density of α-dispersoids were determined by image analysis of the STEM micrographs using ImagePro software. The number of dispersoids were counted on each STEM micrograph to calculate the number density for each sample area. The diameter of an area-equivalent circle was reported as dispersoid size.

3.3 Results and discussion

3.3.1 Microstructures in as-cast and homogenized alloys

The as-cast microstructure of alloy A is shown in Figure 3.1. The alloy showed a multiple-phase dendritic structure with porosity in as-cast condition. Several morphologically distinct constituents were observed, mostly formed along grain boundaries (GBs), which were identified by a combination of morphology and composition analysis. The SEM-EDS results in Figure 3.2 and Table 3.2 display that the as-cast microstructure was composed of three constituent phases: a dominant α-Al(MnCrFe)Si phase (typical lamellar or Chinese script-like morphology), a minor phase of dark Mg_2Si (needle-shaped or Chinese script-like morphology), and a small amount of AlMgSiCu phase (round or oval-shaped morphology), which are consistent with literature [189]. As reported by Han et al. [189], Mn has obvious inhibiting effect on the formation of β-platelets in which no Mn can be present [21], and promote the more compact, less harmful α-phase formation in 6xxx series Al alloys. In the present study, only α-phase was found in the as-cast microstructure of the examined alloys. The EDS analysis shows the average composition of 66.3 wt% Al, 23.8 wt% (Mn+Cr+Fe) and 7.5 wt% Si in α-Al(MnCrFe)Si phase, corresponding to a formula of $Al_{9.1}(FeMnCr)_{1.6}Si$, which is close to the reported $Al_{15}(FeMnCr)_3Si_2$ stoichiometry of the α-phase in literature [22,190]. The AlMgSiCu phase contained a high content of copper, which has been mostly designated as Q-phase [74]. In addition, the formation of porosity during the solidification process was generally attributed to two factors [1,151]: (1)

shrinkage resulting from the volume contraction accompanying solidification due to a lack of interdendritic feeding, and (2) gas evolution (mainly hydrogen) resulting from a sudden decrease in gas solubility in solid metal compared to the liquid. The distributions of the alloying elements contained in as-cast alloy A are shown in Figure 3.3. According to the EPMA mappings, non-uniform distributions of the elements were revealed in the Al matrix. The large bright blue areas along the grain boundaries indicate high concentrations, mainly in constituent phases, while dark areas show low concentrations. As can be seen, in solid solution the Mn was roughly uniformly distributed within the grains, but there were Mn depleted regions (i.e., the dark regions in Figure 3.3(h)) along the GBs where Mg_2Si phase was formed (Figures 3.3(e,h)).

The microstructure of the examined alloys after homogenization at 540 $^{\circ}$C holding for 4 hours is illustrated in Figure 3.4. As shown in Figure 3.4(a), coarse constituent phases decreased with the increase of temperature and soaking time during homogenization. After homogenization the majority of Mg_2Si and AlCuMgSi phases were dissolved into the Al matrix, and α-Al(FeMnCr)Si phase began to fragment and spheroidize during homogenization process. Besides, there was a large quantity of fine dispersoids formed in the grains during homogenization treatment due to the decomposition of supersaturated elements in as-cast Al matrix. The distribution of dispersoids in the matrix is clearly presented by etching pits in Figure 3.4(b), and the PFZs surrounding grain boundaries can also be observed. Figure 3.4(c) shows the precipitation of dispersoids in alloy A annealed at 540 $^{\circ}$C for 4 hours by STEM observation. The dispersoids were generally present in three morphologies, i.e., rods, platelets and little blocks, as indicated by the red arrows, and some of the "rod-like" dispersoids were actually platelets due to the observation from one view direction [191]. Furthermore, STEM-EDS results in Figures 3.4(d,e) indicate that the dispersoids were composed with Al, Mn, Cr, Fe and Si elements, which are believed to be α-Al(MnCrFe)Si dispersoids based on their morphologies and composition which were almost identical with those of α-Al(MnCrFe)Si dispersoids formed during high temperature homogenization treatment in AA6xxx Al alloys, as reported in literature [45,50]. Due to the high content of Cu in the matrix, it could not be considered as a certain element in the dispersoids. STEM analysis was performed to reveal PFZs besides

dispersoids formation. The PFZs surrounding grain boundaries (Figure 3.5(a,b)) can be observed in alloy A after 4 hours of homogenization at 560 ˚C. This was due to the obvious depletion of Mn around the Mg_2Si particles at grain boundaries based on the EPMA results (Figure 3.3). However, the presence of a PFZ was not observed if enough amount of Mn existed near a grain boundary, and a considerable amount of dispersoids were thus formed after homogenization (Figure 3.5(c)).

3.3.2 Effect of heating rate on the formation of dispersoids

Figures 3.6-3.10 present STEM micrographs showing precipitation of dispersoids in the examined alloys after different homogenization treatments, in which the effects of various parameters - heating rate, Mn content, low temperature pre-nucleation treatment and homogenization temperature, on the formation of dispersoids were revealed. Moreover, as illustrated in Figure 3.11, quantitative measurements have been conducted on STEM micrographs to clearly indicate the difference in size, number density and aspect ratio of the dispersoids formed under different homogenization conditions.

It was found that heating rate could significantly affect the number density of dispersoids. The number density of dispersoids increased more than twice when lower the heating rate from 6 ˚C min^{-1} to 0.6 ˚C min^{-1} (Figure 3.11(e)). Reducing the heating rate could also decrease the equivalent size of dispersoids (Figure 3.11(a)). In the present investigation, the dispersoids formed during homogenization have an incoherent interface to the Al matrix and homogeneous nucleation thus seems to be excluded [45]. It is known that heterogeneous nucleation at another phase can reduce the nucleation energy barrier of dispersoids, and therefore, several sites for heterogeneous nucleation have been suggested. The work by Hu et al. [48] showed that α-dispersoids preferentially nucleated on the β'-Mg_2Si needles during homogenization of an AA6082 Al alloy with the addition of Mn. The formation of the Mn-containing dispersoids, which nucleated on the β'-Mg_2Si phase, were strongly affected by the heating rate. It was observed that a rapid heating rate produced large needle-shaped dispersoids with heterogeneous distribution, while a slow heating rate produced homogeneously distributed fine spherical-shaped dispersoids. This is because that the β'-Mg_2Si phase was preferentially formed in the areas rich in Mg and

Si when the heating rate was high, whereas the β'-Mg_2Si phase was able to nucleate everywhere in the matrix if the heating rate was slow. Lodgaard and Ryum [45] studied the nucleation mechanism of α-dispersoids in Al-Mg-Si alloys with various amounts of Mn and Cr during high temperature annealing. It was found that the dispersoids nucleated heterogeneously on an intermediate phase, referred to as the 'u-phase' that nucleated on the β'-Mg_2Si needles. In order to obtain a uniform dispersoids distribution in the alloys, it was necessary to heat with a low heating rate from a fairly low temperature ($T < 250\ ^{\circ}C$) to the annealing temperature. During such slow heating, a large number of β'- precipitates were formed which was a prerequisite for a high density of nucleation sites ('u-phase') for the dispersoids. The formation mechanism for α-dispersoids in the studied alloy has been recently revealed by the author which will be described in detail in chapter 5. The Q-AlMgSiCu phase was considered to be the nucleation site for the α-dispersoids. During slow heating ($0.6\ ^{\circ}C\ min^{-1}$), larger number of Q-precipitates could be formed, which was a prerequisite for the formation of higher number density of dispersoids. Lower heating rate could also promote the diffusion of Mn and nucleation of α-dispersoids on Q-precipitates, leading to larger amount of dispersoids. When higher heating rate was used, the less formed dispersoids tend to grow and coarsen, resulting in the increased frequency of dispersoids with larger equivalent diameters, as shown in Figure 3.11(a).

3.3.3 Effect of Mn content on the formation of dispersoids

The concentration of Mn was revealed to strongly affect the shape, equivalent size and number density of dispersoids formed during homogenization. In alloy C, the Mn level was high, resulting in the larger length/width ratio (Figures 3.7 and 3.8), number density (Figure 3.11(e)) and equivalent size (Figure 3.11(b)) of dispersoids after the same annealing treatment as alloy B with low content of Mn. Increasing the Mn content, the amount of Mn supersaturation in the Al matrix after solidification was increased, which provided more dispersoids-forming element, leading to more nucleation and growth of dispersoids, confirmed by the broadening of particle size distribution shown in Figure 3.11(b). In addition, the shape difference of dispersoids can be clearly observed from Figure 3.8. In the alloy containing trace amount of Mn (alloy B), the shape of dispersoids was more square-like (Figures 3.8(a-c)), meaning that the aspect ratio was close to 1. Whereas the

aspect ratio of dispersoids could be much larger than 1 in high Mn alloy (alloy C), as illustrated in Figures 3.8(d,e). It was possible that the dispersoids with low aspect ratio served as precursors for the high aspect ratio ones. As the square-like dispersoids precipitated during homogenization, the insufficiency of Mn restrained the formation of new structure. Whereas when Mn was adequate, the square-like dispersoids could evolve into rod-like or plate-like shapes.

3.3.4 Effect of low temperature pre-nucleation treatment on the formation of dispersoids

As indicated in Figure 3.11(e), low temperature pre-nucleation treatment at 350 °C for 2 hours could increase the nucleation sites (Q-precipitates) of dispersoids, and thus increase the number density of dispersoids compared to that without low temperature pre-nucleation treatment. The equivalent size was found to be similar for the dispersoids formed with or without low temperature pre-nucleation treatment (Figure 3.11(c).

3.3.5 Effect of homogenization temperature on the formation of dispersoids

As shown in Figures 3.11(d,e), increasing the homogenization temperature led to a reduction of the number density and an increase in the equivalent size of dispersoids. As illustrated in Figures 3.10(a,b), after 4 hours annealing at 540 °C, the dispersoids have grown in size, but the number density of the dispersoids has decreased compared to those after annealing at 460 °C. At higher temperature, the solubility and the diffusion speed of Mn increased, resulting in faster growth and coarsening of dispersoids, which led to the number density decrease and size increase of dispersoids. This is confirmed by the electrical conductivity measurements on the alloy after homogenization at different temperatures, shown in Figure 10(c). According to Matthiessen's law [100,193], Mn, Cr and Fe have relatively greater contributions to increase the electrical resistivity as compared to other elements. In the alloys studied, nearly all the Fe content formed constituent particles. The decrease of electrical conductivity after homogenization at 540 °C (red arrow) compared to 460 °C (blue arrow) was due to the increased solubility of Mn (Cr) in the matrix, which made plenty of finer dispersoids dissolve into the Al matrix, leading to the decrease in number density. Figure 3.11(d) displays the size distribution of

the dispersoids homogenized at the two annealing temperatures. At lower temperature (460 °C), the size histogram is very narrow. With the increase in homogenization temperature (540 °C), the size distribution moved to the right side, and the frequency of the dispersoids with larger equivalent diameters went up, meaning the growth and coarsening of dispersoids. A larger scatter in size was also present when the temperature was increased.

3.4 Conclusions

(1) The as-cast microstructure of the alloys studied consisted of a dominant α-Al(FeMnCr)Si constituent phase, a minor phase of Mg_2Si and a small amount of AlCuMgSi phase. During homogenization treatments, α-phase began to fragment and spheroidize, and Mg_2Si and Q-AlCuMgSi phases were almost fully dissolved into the Al matrix.

(2) During homogenization treatments, a large amount of α-Al(MnFeCr)Si dispersoids were formed in the alloys which had the morphology of rods, platelets and fine blocks, with PFZs being formed surrounding grain boundaries. The formation of α-dispersoids was strongly affected by various homogenization parameters, such as heating rate, content of Mn, low temperature pre-nucleation treatment and homogenization temperature. Increasing the heating rate or homogenization temperature led to a reduction of the number density and an increase in the equivalent size of dispersoids. A higher Mn content resulted in a larger number density, equivalent size and length/width ratio of the dispersoids. Through low temperature pre-nucleation treatment, the number density of dispersoids was increased.

Table 3.1 The chemical compositions of Al-Mg-Si-Cu alloys studied in the present work (in wt%.)

Alloy	Mg	Si	Cu	Mn	Cr	Fe
A	0.85	1.24	0.43	0.63	0.26	0.15
B	0.85	1.21	0.37	0.04	0.23	0.15
C	0.97	1.16	0.36	0.80	0.21	0.18

Table 3.2 Compositions of experimentally observed constituent phases in as-cast microstructure (in wt%)

Phase	Al	Mg	Si	Cu	Mn	Cr	Fe
Al(MnCrFe)Si	61.56	0.60	7.47	1.25	12.81	2.16	14.15
Al(MnCrFe)Si	68.93	0.85	6.87	1.13	9.90	1.78	10.54
Al(MnCrFe)Si	63.93	1.26	9.05	1.37	12.83	4.88	6.69
Al(MnCrFe)Si	70.74	0.92	6.67	2.07	9.43	1.68	8.48
AlMgSiCu	56.79	2.68	7.09	33.21	0.09	0.05	0.09
AlMgSiCu	66.27	2.54	3.59	24.59	1.92	0.57	0.52
MgSi	69.65	6.63	22.34	1.36	0.00	0.00	0.02
MgSi	64.39	17.92	16.83	0.63	0.14	0.05	0.03

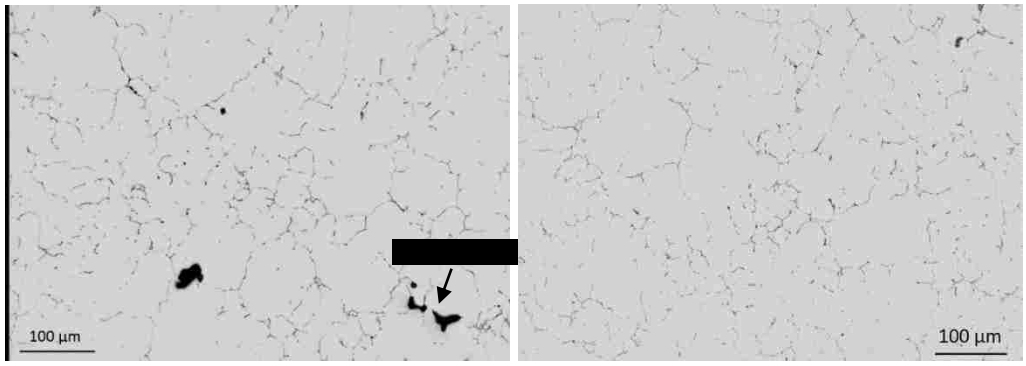

Figure 3.1 Optical micrographs of alloy A in as-cast state.

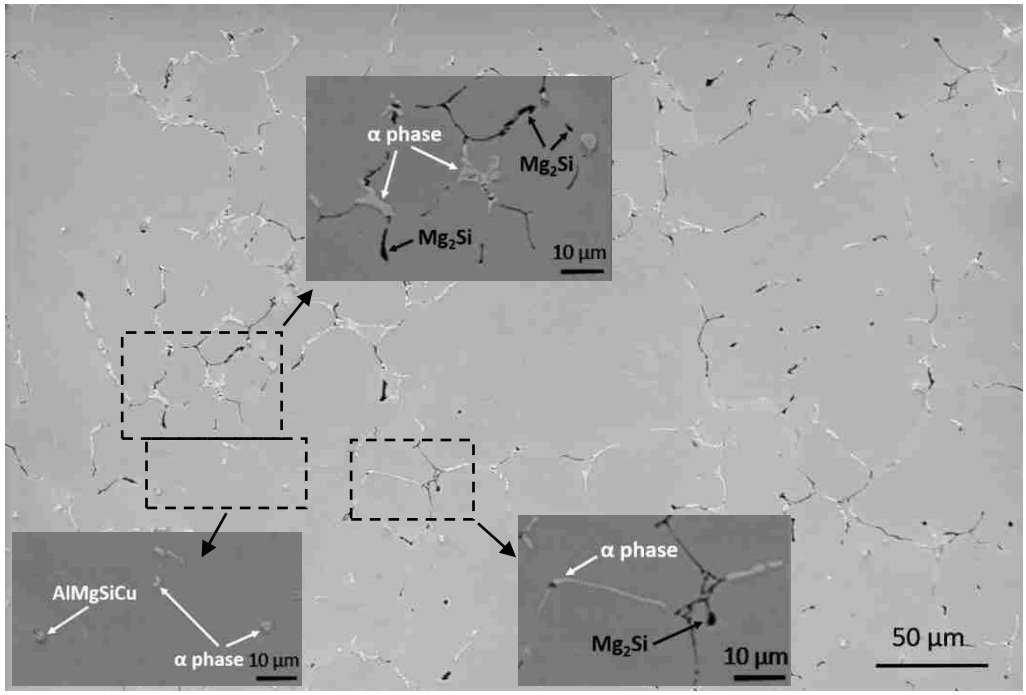

Figure 3.2 SEM images of constituents in as-cast alloy A.

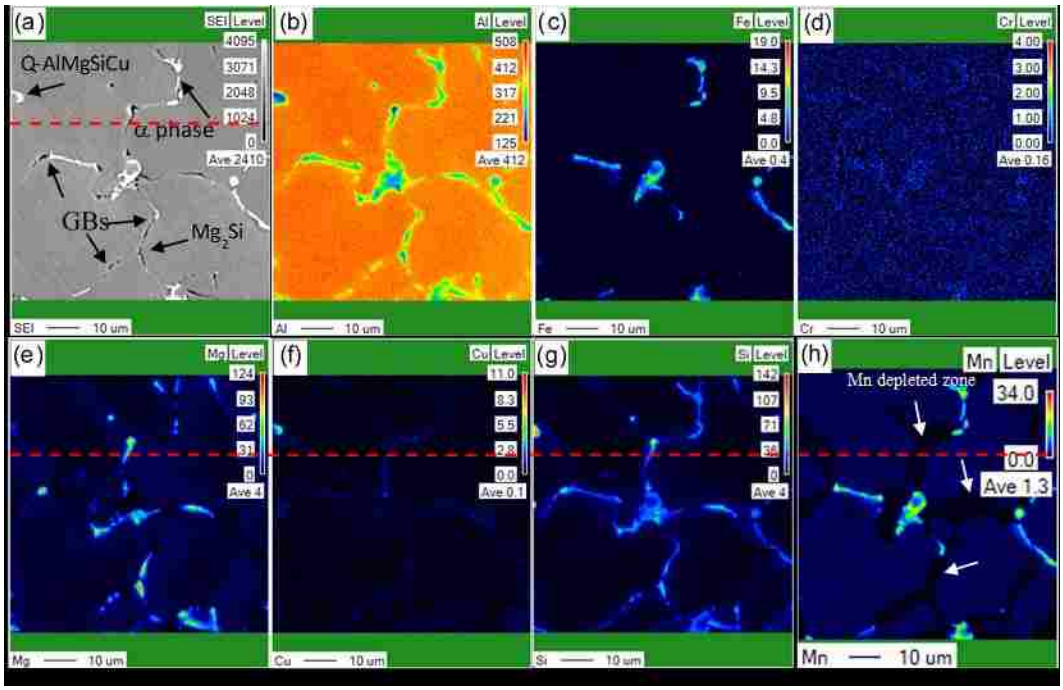

Figure 3.3 EPMA maps for the as-cast alloy A. (a) SE image of the alloy; EPMA elemental maps: (b) Al distribution; (c) Fe distribution; (d) Cr distribution; (e) Mg distribution; (f) Cu distribution; (g) Si distribution and (h) Mn distribution with a line scan along the line.

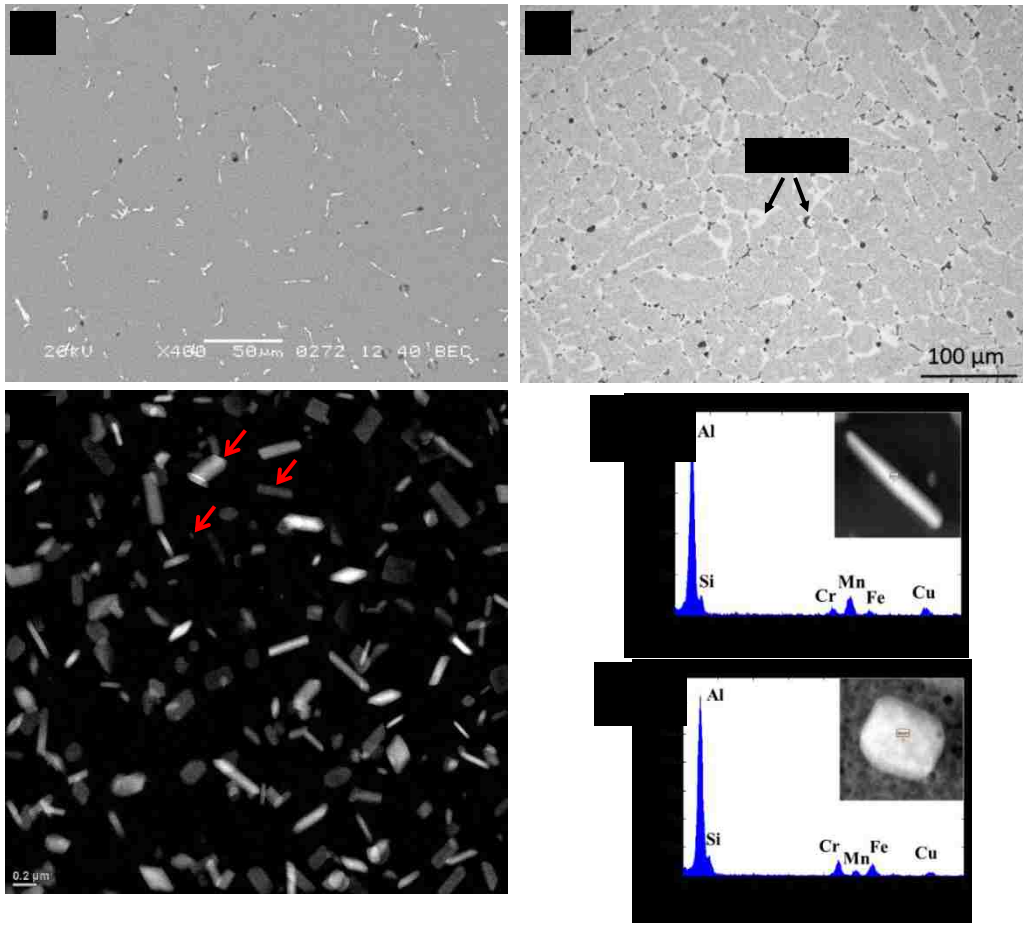

Figure 3.4 Microstructure of alloy A after homogenization at 540 ˚C holding for 4 hours. (a) SEM image; (b) optical micrograph; (c) STEM micrograph showing typical morphology of dispersoids; (d) and (e) STEM-EDS results of dispersoids in alloys A and B after homogenization.

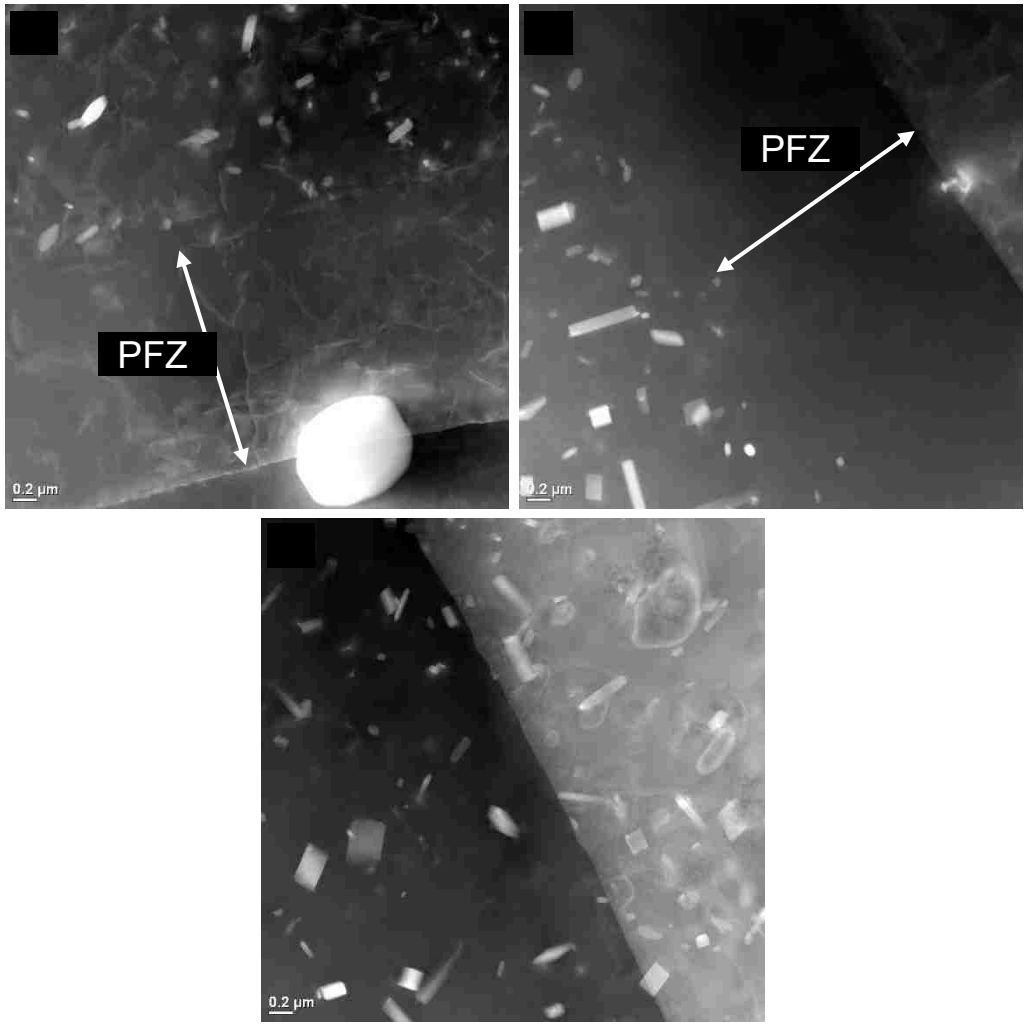

Figure 3.5 Precipitation free zones in alloy A after homogenization at 560 ˚C holding for 4 hours (0.6 ˚C min^{-1}). (a) and (b) along grain boundary; and (c) no PFZ along grain boundary.

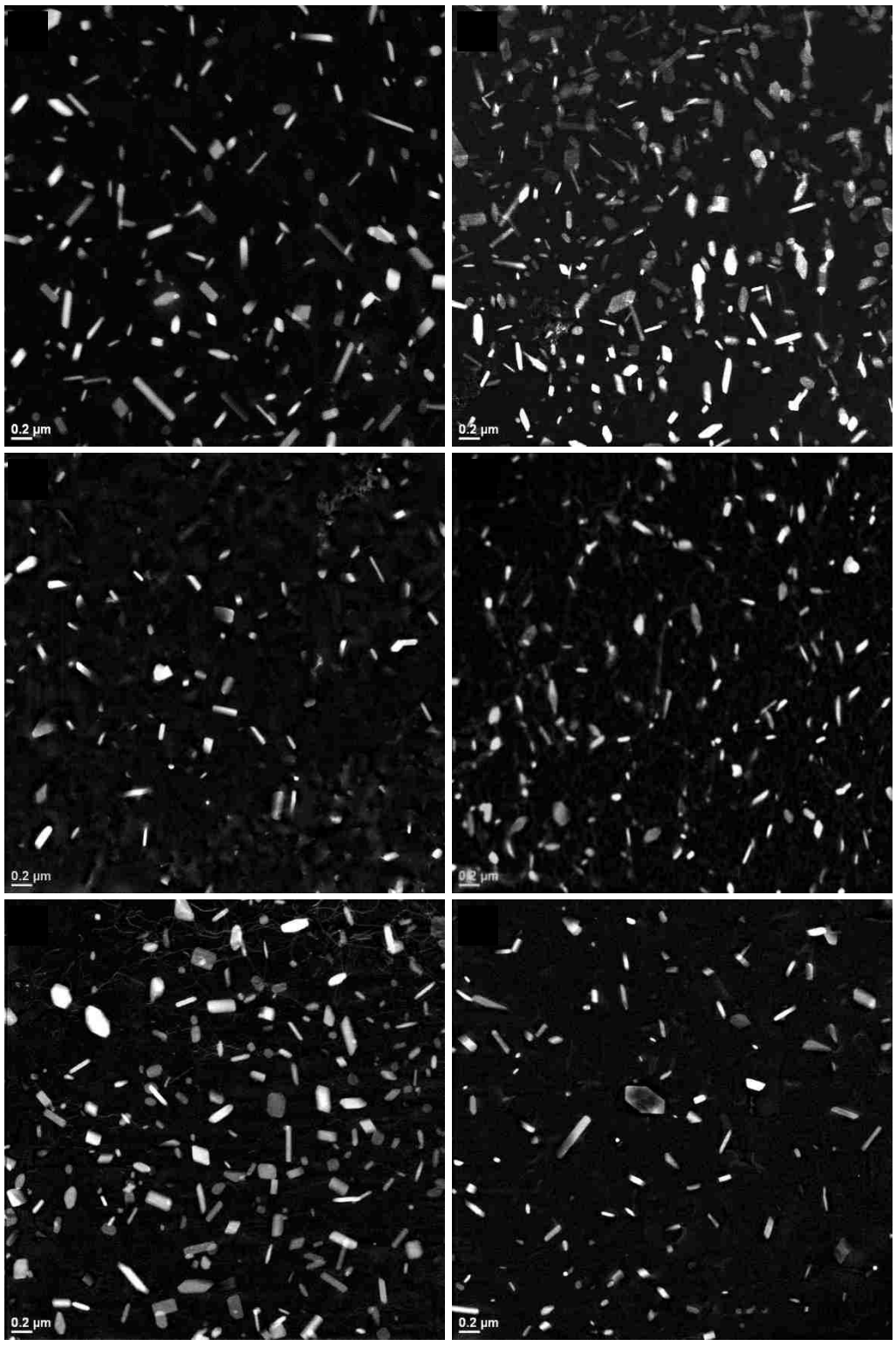

Figure 3.6 STEM micrographs showing the effect of heating rate on the formation of dispersoids in (a)-(c) Alloy A, 540 ˚C/4 h, 6 ˚C min^{-1}; (d)-(f) alloy A, 540 ˚C/4 h, 0.6 ˚C min^{-1}.

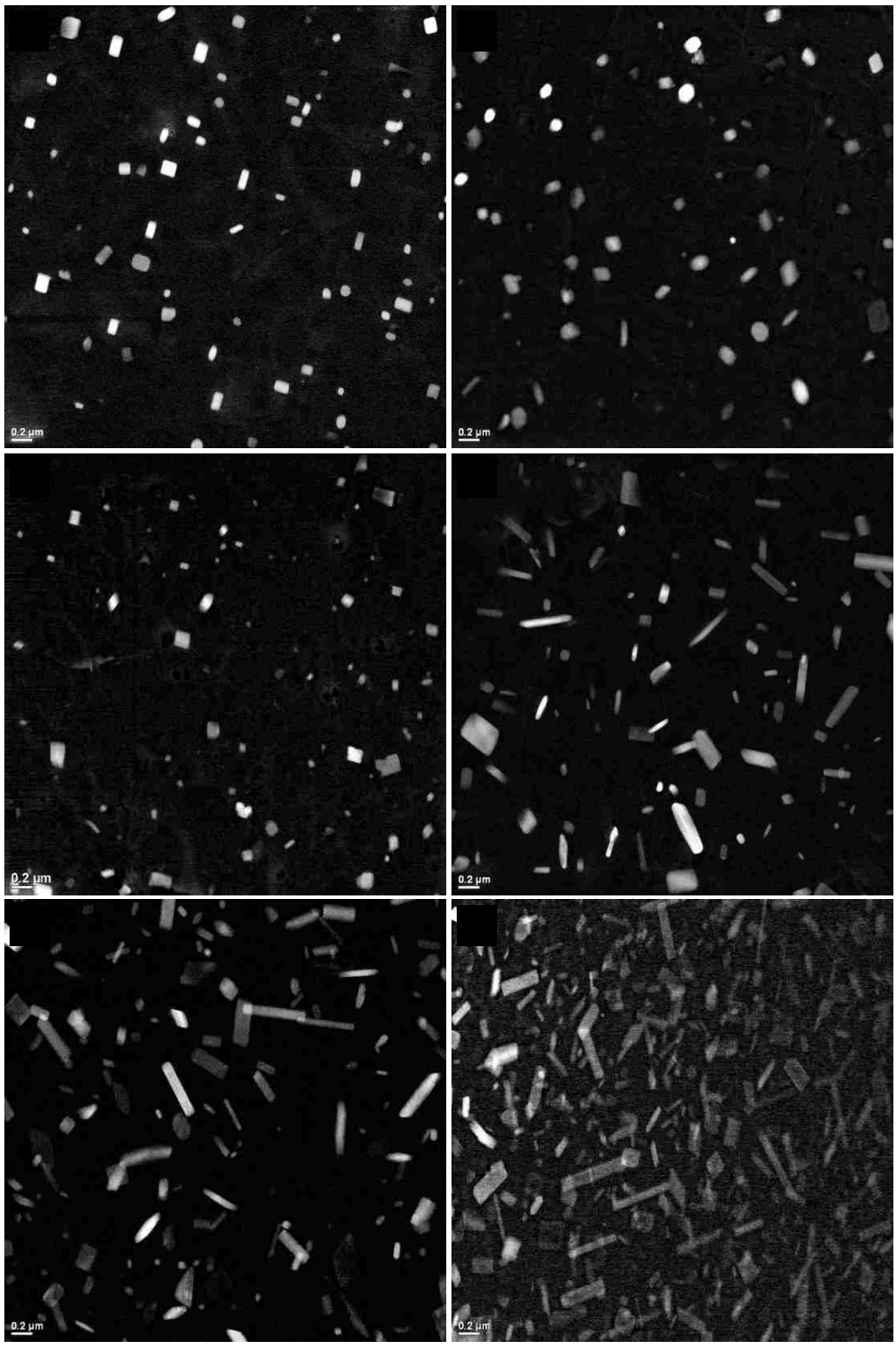

Figure 3.7 STEM micrographs showing the effect of Mn concentration on the formation of dispersoids in (a)-(c) Alloy B, 560 ˚C/4 h, 6 ˚C min^{-1}; (d)-(f) Alloy C, 560 ˚C/4 h, 6 ˚C min^{-1}.

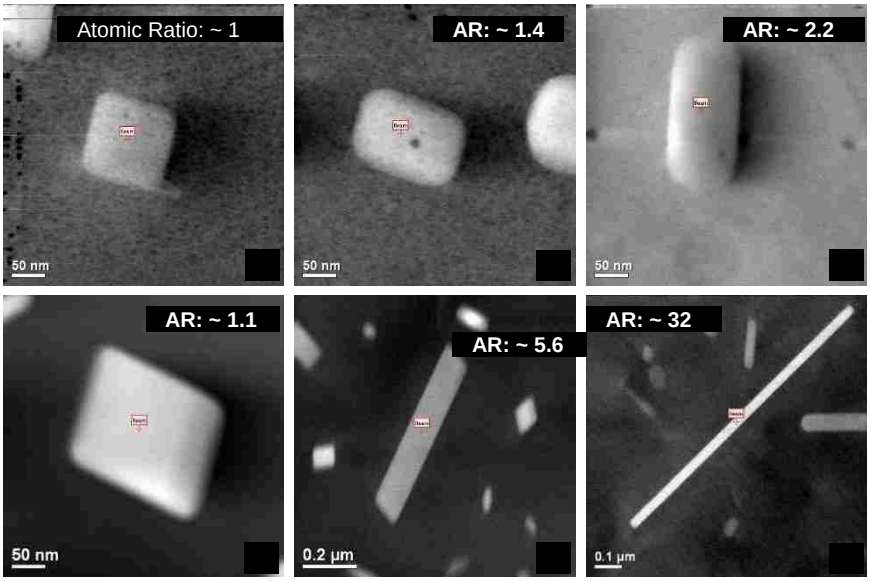

Figure 3.8 Morphology of dispersoids formed after homogenization at 560 ˚C holding for 4 hours (6 ˚C min^{-1}) in (a-c) alloy B and (d-f) alloy C.

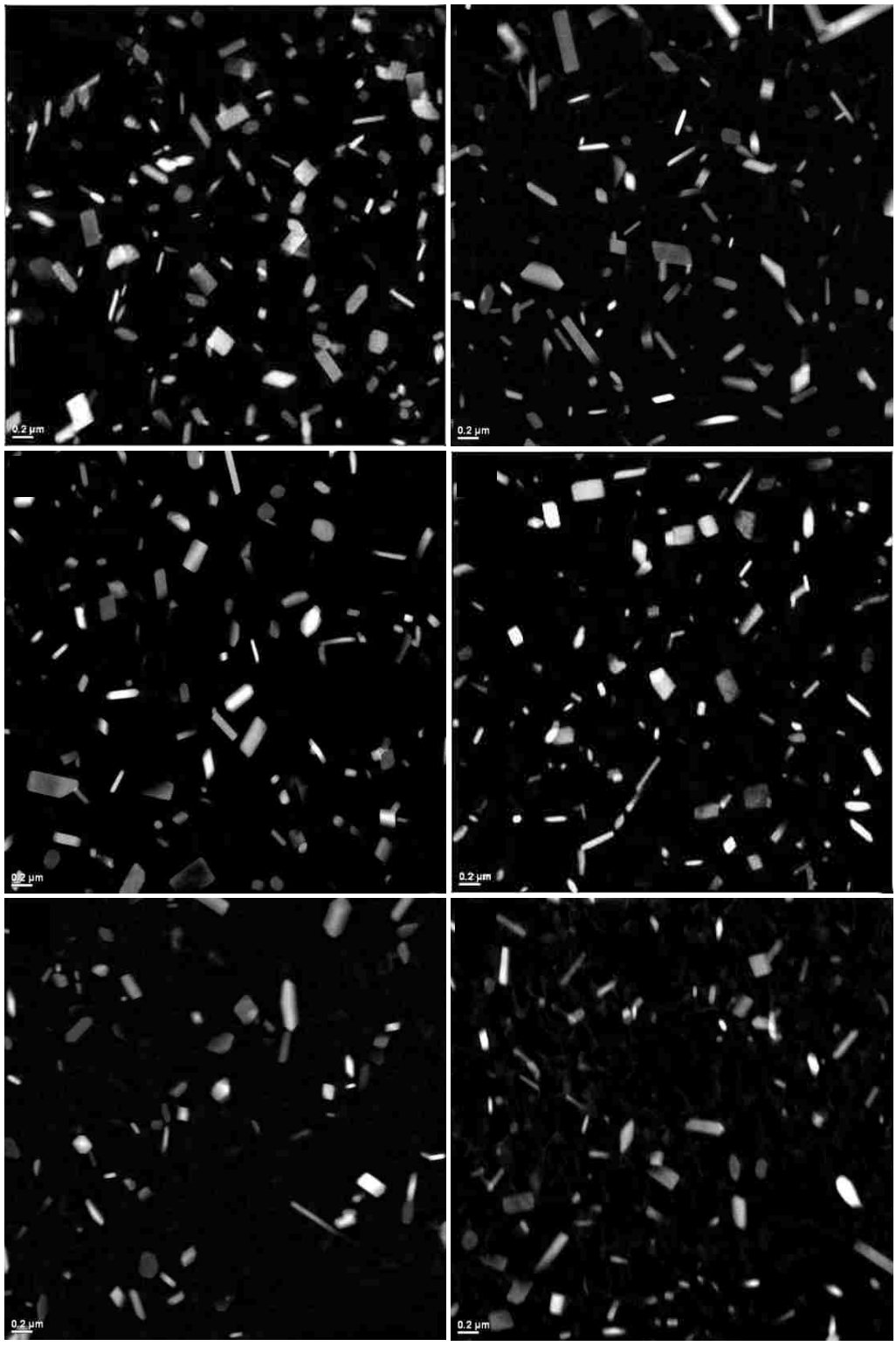

Figure 3.9 STEM micrographs showing the effect of low temperature pre-nucleation treatment on the formation of dispersoids in (a)-(c) Alloy A, 350 ˚C/2 h to 560 ˚C/4 h, 6 ˚C min^{-1}; (d)-(f) alloy A, direct heating to 560 ˚C/4h.

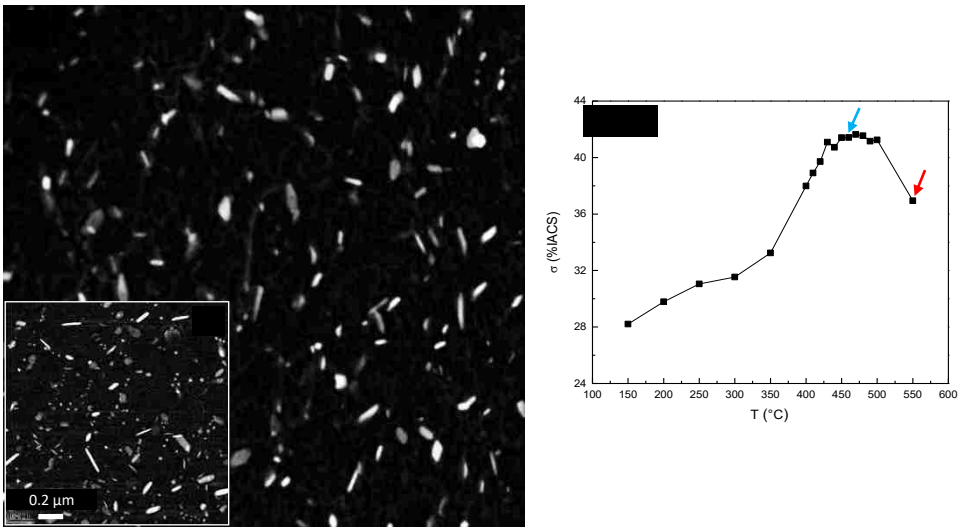

Figure 3.10 STEM micrographs showing the formation of dispersoids in alloy A after homogenization at (a) 540 ˚C and (b) 460 ˚C holding for 4 hours (0.6 ˚C min^{-1}); (c) electrical conductivity of alloy A annealed at different temperatures holding for 4 hours.

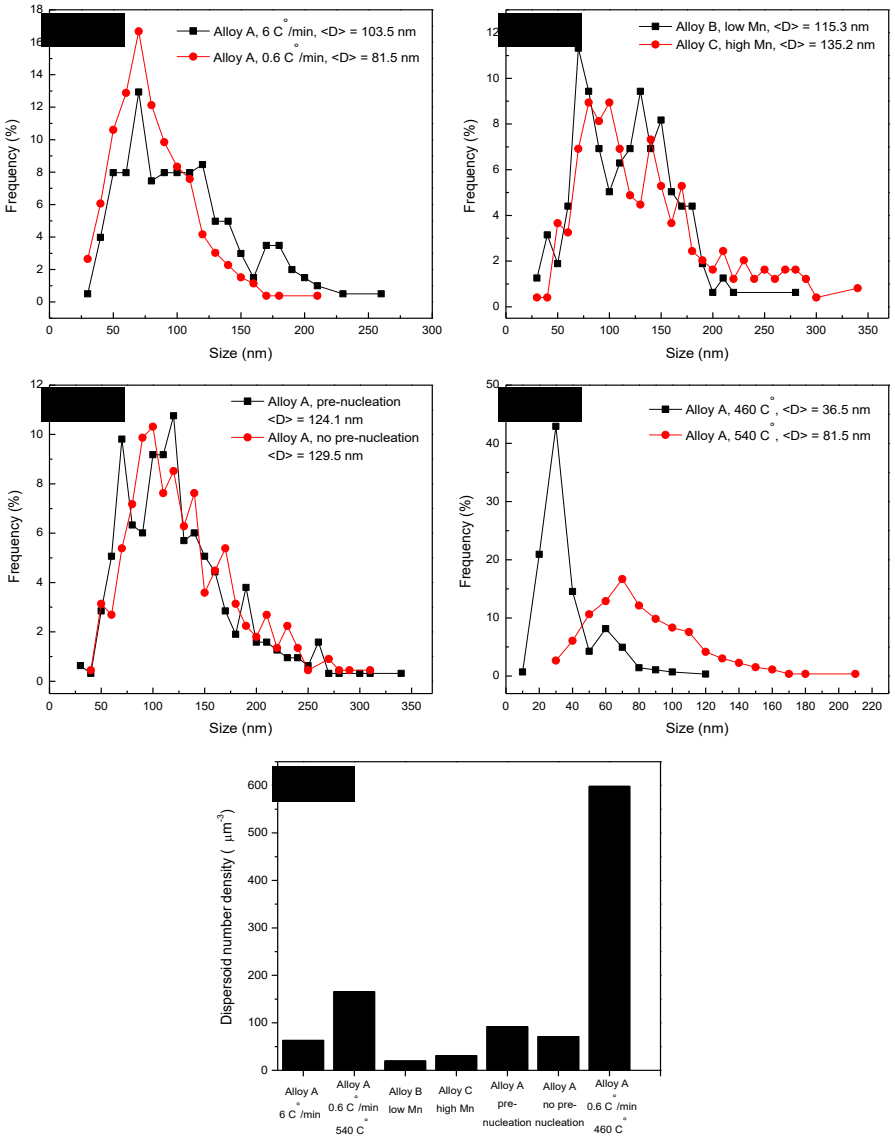

Figure 3.11 Size distribution of dispersoids in (a) Alloy A, 540 ˚C/4 h, 6 ˚C min^{-1} and 0.6 ˚C min^{-1}; (b) alloy B and alloy C, 560 ˚C/4 h, 6 ˚C min^{-1}; (c) alloy A, 350 ˚C/2 h to 560 ˚C/4 h, 6 ˚C min^{-1} and direct heating to 560 ˚C/4h; (d) alloy A, 540 ˚C/4 h and 460 ˚C/4 h, 0.6 ˚C min^{-1}; (e) number density of dispersoids after above homogenization treatments.

Chapter 4 Effects of Mn and Cr addition on the recrystallization behaviors of modified AA6061 (Al-Mg-Si-Cu) Al alloys

4.1 Introduction

Wrought Al alloys are subject to complex thermomechanical processing treatments to obtain good mechanical properties, such as high yield strength and good fracture toughness [1]. Homogenization heat treatment, which is an early processing stage and carried out directly after casting, is particularly critical, since it plays a key role in determining the microstructural evolution during subsequent processing steps. One of the primary objectives of the homogenization process is to form dispersoids with small size and high distribution density, which could give rise to an enhancement of the alloys' performance through retardation of recrystallization in addition to dispersoid strengthening during following deformation and solution heat treatments [44]. The effects of various types of dispersoids in different series of Al alloys on the inhibition of recrystallization have been extensively investigated. For example, in 3xxx series Al alloys, Mn-containing dispersoids, formed during homogenization, play an important role in controlling the recrystallization behaviors of the alloys [191,194,195]. In the case of 7xxx series Al alloys, the Zr and/or Sc-containing dispersoids, which lead to recrystallization inhibition, have been a subject of interest for many years [196-199]. In 6xxx series Al-Mg-Si(-Cu) alloys, Mn and/or Cr-containing dispersoids with a high thermal stability and number density could effectively retard the behaviors of recovery/recrystallization of the alloys, due to their strong pinning effects on the movement of dislocations and grain boundaries at elevated temperatures during or after plastic deformation, thereby leading to fine grain structure by forming a large volume fraction of subgrains during thermomechanical processing, enhancing both strength and toughness of these alloys [46-49,88,200]. However, the inhibiting effects of these dispersoids during hot deformation still need to be investigated, especially in AA6061Al alloys with addition of Mn and Cr.

In this chapter, the retardation effect on recrystallization in two Mn and Cr-containing modified AA6061 (Al-Mg-Si-Cu) Al alloys with various Mn contents during hot deformation and solution heat treatment were studied using upsetting experiments, STEM

and EBSD. It was found that the Mn and Cr-containing dispersoids formed during homogenization could effectively inhibit recrystallization, as they could effectively limit the mobility of dislocations and grain boundaries in the alloys. Because of the addition of higher amount of Mn, more dispersoids could be formed, leading to enhanced recrystallization inhibition effect.

4.2 Experimental details

Two Mn and Cr-containing Al-Mg-Si-Cu alloys with varying amounts of Mn were prepared by Suzhou Research Institute for Nonferrous Metals, China. The chemical compositions of alloys A and B were (wt%): Mg 0.85, Si 1.21, Cu 0.37, Mn 0.04, Cr 0.23, Fe 0.15, and Mg 0.85, Si 1.24, Cu 0.43, Mn 0.63, Cr 0.26, Fe 0.15, respectively. These two alloys were made into billets with 100 mm in diameter and 250 mm in length after direct-chill casting, followed by homogenization at 560 $^{\circ}$C for 4 hours at a heating rate of 6 $^{\circ}$C min^{-1}, and subsequently water cooling.

Upsetting experiments on cylindrical samples of the two alloys (100 mm in diameter and 120 mm in height) machined from the cast billets were carried out at a speed of 15 mm s^{-1} under upsetting temperature of 450 $^{\circ}$C after homogenization at 560 $^{\circ}$C for 4 hours using a 300-Tone hydraulic press. In the upsetting tests, the flat dies were first heated to 250 $^{\circ}$C before the samples were deformed from 120 mm to 60 mm in height followed by water quenching to retain the microstructure formed during upsetting. These samples were then sectioned into two halves along their axes. One half of a sample was used for examination of the deformed microstructure, and the other was solution heat treated at 560 $^{\circ}$C for 1 hour to study the microstructure evolution in the alloys during solid solution heat treatment after upsetting. Since the strain was non-uniform along the thickness of a sample due to the friction between the specimen and anvil during deformation, the specimens used for microstructure observation were all taken from the center of the hot deformed samples. Electron backscatter diffraction (EBSD) measurements were employed to study the microstructures after upsetting and solid solution heat treatment on a JEOL JSM-6480 scanning electron microscope. The specimens were electrolytic polished using 10 vol.%

HClO4 acid in alcohol. The fractions of recrystallization were analyzed using the software provided by TexSem Lab Inc.

In this work, cylindrical samples of the two alloys with a diameter of 10 mm and height of 15 mm for hot compression tests were also machined from the cast billets. A graphite sheet coated with high temperature lubricant was used between the specimen and anvils to reduce the friction between them in hot compression. Compression tests were carried out on a Gleeble-3500 system at the strain rate of 1 s^{-1} and deformation temperatures between 420 and 550 $^{\circ}$C for alloy A, between 390 and 460 $^{\circ}$C for alloy B, varied at the interval of 10 $^{\circ}$C. The samples were first heated to the deformation temperature at a heating rate of 5 $^{\circ}$C s^{-1} and held for 120 s before compression. When the samples were deformed 50% in the compression tests, the compressed samples were water quenched and post solution heat treated at 550 $^{\circ}$C for 2 hours before quenching into water. After following T6 heat treatment (artificial aging at 180 $^{\circ}$C for 6 hours in an air furnace), the non-recrystallized area fractions were quantified to investigate the effect of Mn content on the recrystallization behavior.

The samples after homogenization and upsetting were studied using a Hitachi 3300 scanning transmission electron microscope (STEM) at 300 kV. TEM thin foils (3 mm in diameter) were prepared using mechanical grinding before electropolishing by Struers TenuPol-5 machine. The electro-polishing was performed at -10 $^{\circ}$C in an electrolyte that contains 70% methanol and 30% nitric acid. EDS attached to the STEM was used to measure the composition of the dispersoids. The thickness of observed areas was measured by electron energy loss spectroscopy (EELS).

4.3 Results and discussion

4.3.1 Precipitates in hot forged alloys

As illustrated in Figure 4.1, the precipitates found in hot deformed samples could be roughly grouped into three sizes - nano-sized (< 100 nm), submicron-sized (< 1 μm) and micron-sized (> 1 μm) precipitates, the compositions of which are shown in Figure 4.2 and Table 4.1. The coarse precipitates contained Cu, Mg and Si, which were widely observed in both the low and high Mn deformed samples but were absent in homogenized samples.

As shown in Figure 4.3, these coarse rods could grow to micron size larger than 1 μm, and many of them were fractured during upsetting, which caused stress concentration by twisting with dislocations (Figures 4.3(b,d), ADF mode in STEM), seriously decreasing the alloys' mechanical properties. It was very possible that these precipitates were formed due to rapid heating before upsetting which may be avoided by using slow heating rate to attain the upsetting temperature after homogenization. The other two sizes of precipitates contained Si, Fe and Cr (Mn), which were α-dispersoids formed during previous high temperature annealing, as described in the following section. As shown in Figure 4.4, the thin rod-like dispersoids were found in high Mn samples but absent in low Mn samples, which was in consistence with homogenized high/low Mn comparison group in last chapter.

4.3.2 Formation of α-Al(MnCrFe)Si dispersoids

In these as-cast commercial Al-Mg-Si-Cu alloy ingots, a part of Mn and Cr content could form the coarse α-AlFe(Mn,Cr)Si phase in the interdendritic channels upon solidification, but the remaining Mn and Cr content might dissolve into the Al matrix, forming supersaturated solid solution, due to fast cooling in casting. During homogenization after casting, coarse α-constitutes fragmented and spheroidized, and fine Mn and Cr-containing α-dispersoids were formed due to the low solubility of Mn and Cr in the matrix. Figures 4.5(a,b) are STEM micrographs showing the fine dispersoids formed during homogenization in the two alloys used in this work before upsetting, respectively. It was found that finely distributed dispersoids were precipitated in both low and high Mn comparative alloys. In the alloy containing trace amount of Mn (alloy A) shown in Figure 4.5(a), the shape of the dispersoids was more square-like, meaning that the aspect ratio was close to 1. Whereas the aspect ratio of the dispersoids was much larger than 1 in high Mn alloy (alloy B), as illustrated in Figure 4.5(b). As discussed in previous chapter, it was possible that the dispersoids with low aspect ratio served as precursors for the high aspect ratio ones. As the square-like dispersoids were precipitated during homogenization, the insufficiency of Mn restrained the formation of new structure. When Mn was adequate, the square-like dispersoids could evolve into rod-like or plate-like shapes. The statistical results of the size and number density of the dispersoids in low/high Mn comparative group were measured (Figure 3.11). The aspect ratio of the dispersoids in high Mn alloy was

much higher judging from the STEM micrographs (Figures 3.8 and 4.5). In addition, the high Mn alloy possessed larger number density and equivalent size of dispersoids after the same annealing treatment as the low Mn alloy. It thus could be concluded that alloying element Mn had a major effect of controlling the shape, equivalent size and number density of dispersoids. Higher Mn content could effectively increase the length/width ratio, number density and equivalent size of dispersoids.

The composition analysis by EDS (Figures 4.5(c,d) shows that the dispersoids in the two alloys both contained the same type of elements: Mn, Si, Cr, Fe and Cu. And it indicates that Mn was the dominant element in the Mn-containing dispersoids in the high Mn alloy, while in the low Mn alloy, higher Cr and Fe peaks were detected in those dispersoids. Cu could not be considered as a certain element in the dispersoids, since the Cu content in the matrix was also high. Based on their morphology and the composition measurements, these dispersoids were all α-dispersoids.

4.3.3 Inhibiting effects of dispersoids on recovery and recrystallization

In an alloy with high stacking fault energy, like most Al alloys, dislocations could more readily rearrange themselves, leading to dislocation annihilation and formation of subgrain boundaries during hot deformation, which is so called dynamic recovery (DRV). As a result, the conventional discontinuous dynamic recrystallization, consisting of nucleation and long-distance growth of new grains, does not commonly take place in commercial Al alloys except in high purity Al and in Al alloys containing coarse particles [89,92,87]. However, continuous dynamic recrystallization (CDRX) may occur in Al alloys during high temperature deformation [91,201]. The authors of this paper have verified the happening of dynamic recovery and continuous dynamic recrystallization during hot deformation in an Al-Mg-Si-Cu alloy with similar composition as the alloys used in this work [88]. The fine Mn and Cr-containing dispersoids with high number density and high thermal stability could effectively inhibit dislocation movement and pin subgrain/grain boundaries, which led to a high resistance to dynamic recovery and continuous dynamic recrystallization during upsetting at elevated temperature.

The distinct pinning effect of the α-dispersoids during upsetting of the alloys A and B is shown in Figures 4.6 and 4.7, illustrating that dislocations were effectively pinned by α-dispersoids in the two alloys. In Figure 4.6(a), the intertwining dislocations in alloy A are evidently revealed. The finely distributed square-like (low aspect ratio) dispersoids became effective inhibitors of the moving dislocations. While in alloy B, the plate-like (high aspect ratio) dispersoids interacted with dislocations as well as the square-like ones, as shown in Figure 4.7. The high number density of dispersoid obstacles in both alloys made the dislocations almost impossible to move long distance. Figures 4.8(a,b) illustrate that dislocations intertwined with each other and formed dislocation cells during hot deformation. These dislocation cells interacted with α-dispersoids during hot deformation and were thus effectively dragged to form (sub)grain boundaries. Figures 4.8(c,d) show α-dispersoids dragging a (sub)grain boundary to inhibit its growth. The dark and bright field contrast in Figure 4.8(d) was due to crystallographic orientation difference between the two grains. Recovery is not a single microstructural change but a series of events which includes dislocations tangle, cell formation, subgrain formation and growth [87]. Therefore, based on the results above, α-dispersoids could be very good inhibitors of dislocation movement and effectively pin (sub)grain boundaries to stabilize the microstructure by inhibiting dynamic recovery during hot deformation. To further understand the dislocation pinning effect of different dispersoids, a combination of annular dark field (ADF) and Z-contrast technique was applied. Under STEM annular dark field (ADF) mode (Figure 4.9(a)), both dislocations and dispersoids were clearly revealed. In Figure 4.9(b), the Z-contrast micrograph eliminated the contrast of dislocations. Two imaging modes in the same area provided a more explicit view of the pinning effect. As indicated by the yellow circles, the little block-like nano-sized dispersoids (< 50 nm) were clean of dislocations, which were simply too small to pin dislocations effectively. Therefore, there existed an optimum size (~0.1-1μm) of dispersoids, which should be neither too small nor too big to effectively interact with dislocations.

As shown in Figure 4.10, quantitative analysis has been made using EBSD to measure the recrystallization fractions of alloy B after upsetting and following solution heat treatment, in which the newly formed grains were revealed, besides the rest of well-developed

subgrains in the unrecrystallized elongated grains. In the EBSD orientation map, red, green and blue lines represent boundaries with misorientations between 2° and 5°, between 5° and 15° and over 15°, respectively. High angle grain boundaries, of misorientation > 15°, were considered as recrystallized grain boundaries. Whereas the boundaries with misorientation under 15° were considered as low angle boundaries, and the grain with such a boundary was thus treated as a subgrain. Using software provided by TexSem Lab Inc., the average fractions of recrystallization of five selected areas in alloy B were calculated after upsetting and following solution heat treatment, respectively. The upsetting microstructure consisted of about 23.5% of the newly formed grains (Figure 4.10(a)) which might be attributed to continuous recrystallization taking place during upsetting. Continuous dynamic recrystallization involves the formation of arrays of low-angle boundaries by progressive accumulation of dislocations and a gradual increase in boundary misorientation until high-angle boundaries are formed, i.e., new grains are finally developed [89,90,93]. The occurrence of dynamic continuous recrystallization could be inhibited by the α-dispersoids due to their obvious pinning effects on dislocations and grain boundaries.

After hot deformation, 6xxx series Al alloys are usually processed by solid solution heat treatment followed by artificial aging to obtain the desired strength. Grains/subgrains may be coarsened during this heat treatment, in which static recrystallization will occur. As shown in Figure 4.10(b), the average fraction of recrystallization in alloy B after solution heat treatment was calculated to be 26.6%. This implied that the finely distributed α-dispersoids could effectively retard recrystallization and therefore, lead to low recrystallization fraction after solid solution heat treatment. Conventional static recrystallization is a reconstruction process of the grain structure in which the deformed grains are replaced by undeformed new grains through nucleation and nucleus growth during heat treatment after deformation. Generation and motion of high angle grain boundaries are necessary to remove the deformed grains. For successful nucleation, three important instability criteria have to be met [10]. (1) Thermodynamic instability: the recrystallization nucleus needs to exceed a critical value due to the requirement of Gibbs free energy decrease for nucleus growth. The heterogeneous nucleation on the existed supercritical nucleus like dislocation cell or subgrain is more favorable than the

homogeneous nucleation with low driving force. (2) Mechanical instability: the driving force should be in local imbalance to move the nucleus boundary in a defined direction, which can be achieved by e.g., an inhomogeneous dislocation distribution. (3) Kinetic instability: generation of high angle grain boundaries which have a sufficiently high mobility to make the nucleus grow. Finely dispersed particles can hinder dislocation motion and migration of (sub)grain boundary. When a particle contacts the grain boundary and its surface replaces part of the grain boundary, the energy of the grain boundary is decreased. However, during the separation of the particle and grain boundary, retarding force (Zener force) is generated due to the increase of energy. In this work, the finely distributed α-Al(MnCrFe)Si dispersoids retarded dislocation movement (Figures 4.6 and 4.7) and dislocation cell (Figures 4.8(a,b)) to form subgrain boundary, leading to the low existence of supercritical nucleus. The dispersoids also gave rise to a homogeneous distribution of dislocations due to their high number density and high thermal stability. Moreover, the formation of high-angle grain boundaries was hindered by α-dispersoids pinning the subgrain boundaries and retarding the transformation of subgrain boundaries to high-angle grain boundaries. Therefore, the three instability criteria of nucleation were hardly fulfilled, and the nucleation of recrystallization was effectively inhibited. In addition, the grain growth of recrystallized grain was also prevented, because of the retardation of high-angle grain boundary migration by these dispersoids (Figures 4.8(c,d)). Consequently, both the nucleation and growth of recrystallized grains were retarded during solution heat treatment in the case of small α-dispersoids with high number density.

4.3.4 Influence of Mn content on recrystallization behavior

Figure 4.11 plots out the non-recrystallized area fraction for the deformation temperature of the two alloys after hot compression at different temperatures and T6 heat treatment. This plot indicates that, for a given alloy, as the deformation temperature increased, the non-recrystallized area fraction increased, the reason of which was that the rise of deformation temperature reduced the stored energy of dislocations, which was the driving force for recrystallization. In addition, the effect of Mn content on recrystallization behavior was studied by examining the non-recrystallized area fraction of the two variant Mn alloys with Mn content of 0.04 and 0.64 wt%, respectively. For alloy A with 0.04 wt%

Mn, the samples were fully recrystallized with deformation temperature of 420 °C and fully non-recrystallized with 500 °C after T6 heat treatment. Whereas, in alloy B with higher content of Mn (0.64 wt%), both the deformation temperatures when fully recrystallization or non-recrystallization occurred after T6 treatment, significantly decreased, meaning larger driving force for recrystallization were needed. This indicates that the addition of higher content of Mn could prevent recrystallization more effectively, due to the formation of higher amount of recrystallization inhibitors - Mn-containing α-dispersoids.

In the modified AA6061 Al alloys studied in this work, a certain amount of Mn and Cr tend to remain in supersaturated solid solution after solidification and precipitated as fine α-Al(MnCrFe)Si dispersoids during following high temperature annealing step. These dispersoids could effectively inhibit recrystallization by pinning dislocations and (sub)grain boundaries. Increasing the Mn content increased the amount of α-Al(MnCrFe)Si dispersoids and therefore, increased the resistance to recrystallization in these alloys. However, part of Mn and Cr interacted with Fe and Si to form coarse constituent α-Al(FeMnCr)Si particles upon solidification, which were divided and spheroidized but not dissolved after homogenization. These coarse constituent particles (> 1 μm) could promote recrystallization through particles stimulated nucleation (PSN), since they could act as preferential sites for nucleation of recrystallization due to the increased strain of the matrix around these particles, especially in PFZs. Increasing the content of Mn also increased the volume fraction of these coarse constituent particles, which could promote the formation of recrystallization grains. In this work, the result shown in Figure 4.11 illustrates that the increased volume fraction of the small dispersoids in the alloys compensated more for the increase in the volume fraction of the coarse constituent particles, resulting in an increase in the recrystallization resistance with increased Mn content.

4.4 Conclusions

(1) Three sizes of precipitates, i.e., nano-sized (< 100 nm), submicron-sized (< 1 μm) and micron-sized (> 1 μm), existed in the alloys after upsetting. The Cu-containing coarse precipitates (> 1 μm), formed during rapid heating before upsetting, could be fractured during hot deformation, which was detrimental to the mechanical properties

of the alloys. The other two sizes of precipitates were fine α-Al(MnCrFe)Si dispersoids that were formed during previous high temperature annealing.

(2) Fine α-Al(MnCrFe)Si dispersoids with high number density and thermal stability were formed during homogenization before upsetting in the two alloys with various Mn contents. It was found that Mn could strongly affect the formation of dispersoids. By increasing the content of Mn, the aspect ratio, number density and equivalent size of the dispersoids were increased in the alloys.

(3) Mn and Cr-containing α-dispersoids with a high number density and thermal stability could effectively retard recovery and recrystallization, and stabilize the microstructure of the alloys during hot deformation and the subsequent solution heat treatment by pinning movement of dislocations and migration of (sub)grain boundaries. A higher content of Mn led to a higher number density of dispersoids, and thus an enhanced retardation effect on recrystallization. An optimum dispersoid size, approximately 0.1~1 μm, was suggested to have the best dislocation pinning effect.

Table 4.1 Compositions of precipitates found in hot deformed samples

Alloy	Size	Major Elements	Other Elements
Alloy A	Coarse	Cu	Si, Mg
	Submicron	Cr	Fe, Si, Mn
	Nano	Cr	Fe, Si, Mn
Alloy B	Coarse	Cu	Si, Mg, Mn, Cr
	Submicron	Mn, Cr	Fe, Si
	Nano	Mn, Cr	Fe, Si

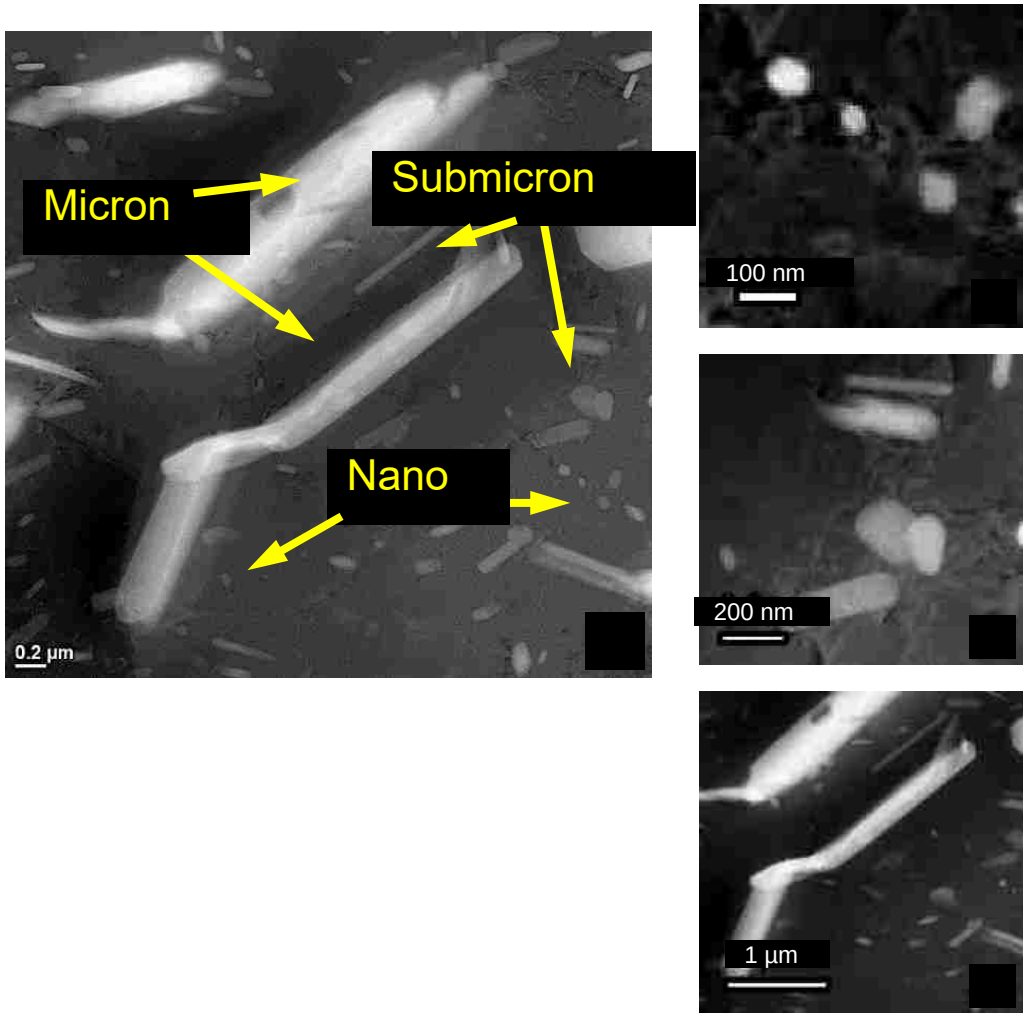

Figure 4.1 Precipitates in alloy B after upsetting at the temperature of 450 ˚C. (a) Different sizes of precipitates; (b) nano-sized precipitates (< 100 nm); (c) submicron-sized precipitates (< 1 µm); (d) coarse micron-sized precipitates (> 1 µm).

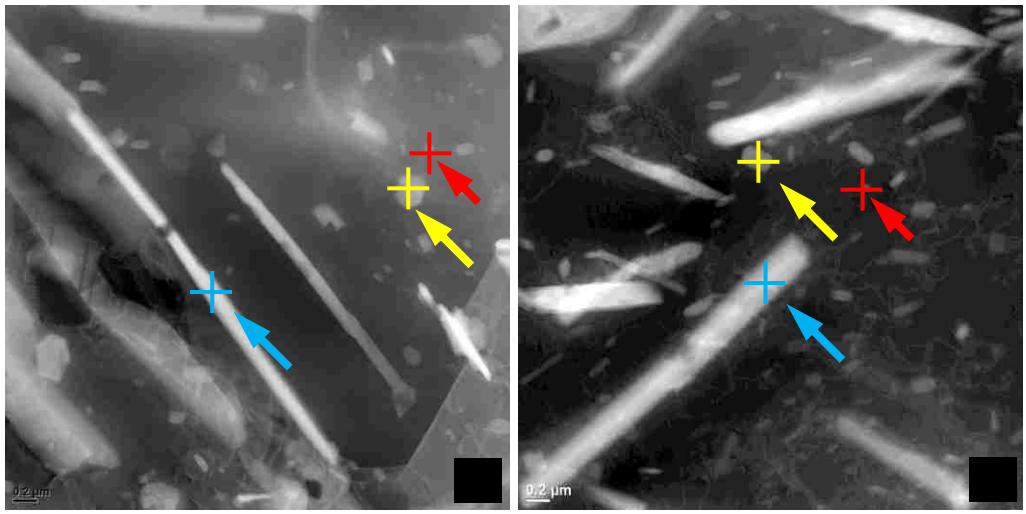

Figure 4.2 Three sizes of precipitates (red color for nano-sized, yellow color for submicron-sized and blue color for coarse-sized ones) in (a) low Mn alloy (alloy A) and (b) high Mn alloy (alloy B) after upsetting at the temperature of 450 ˚C.

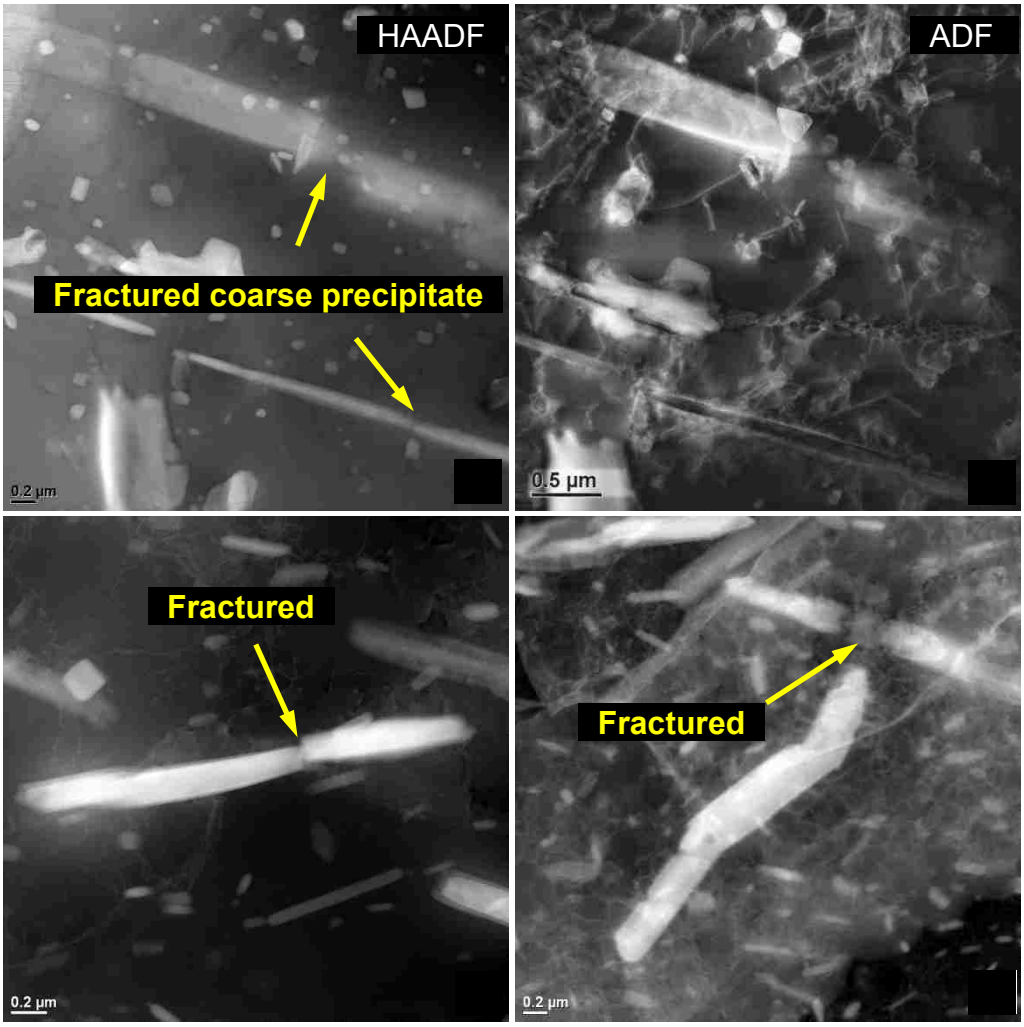

Figure 4.3 STEM micrographs showing fractured coarse precipitates found in (a) and (b) alloy A and (c) and (d) alloy B after upsetting at the temperature of 450 ˚C.

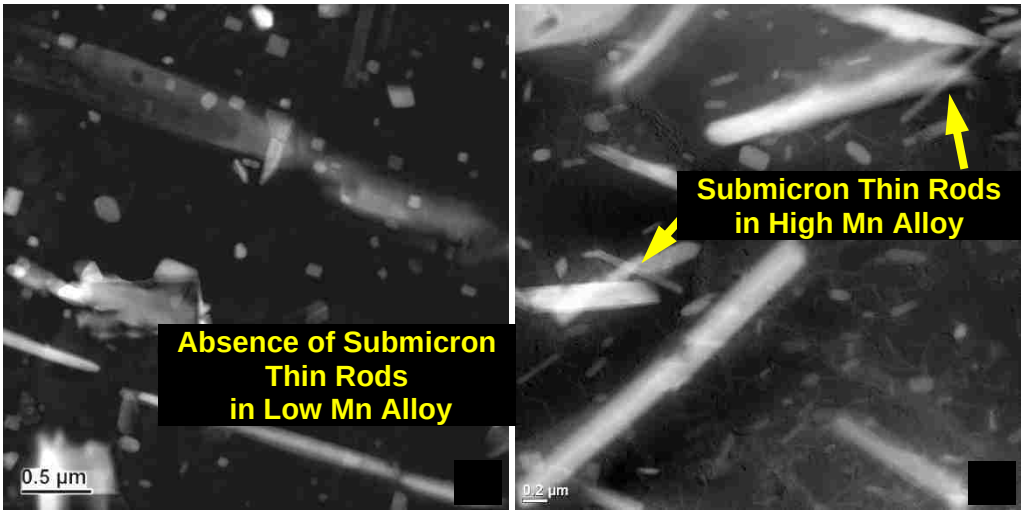

Figure 4.4 STEM micrographs showing (a) absence of submicron-sized thin rods in alloy A and (b) thin rod-like dispersoids distributed inside alloy B after upsetting at the temperature of 450 ˚C.

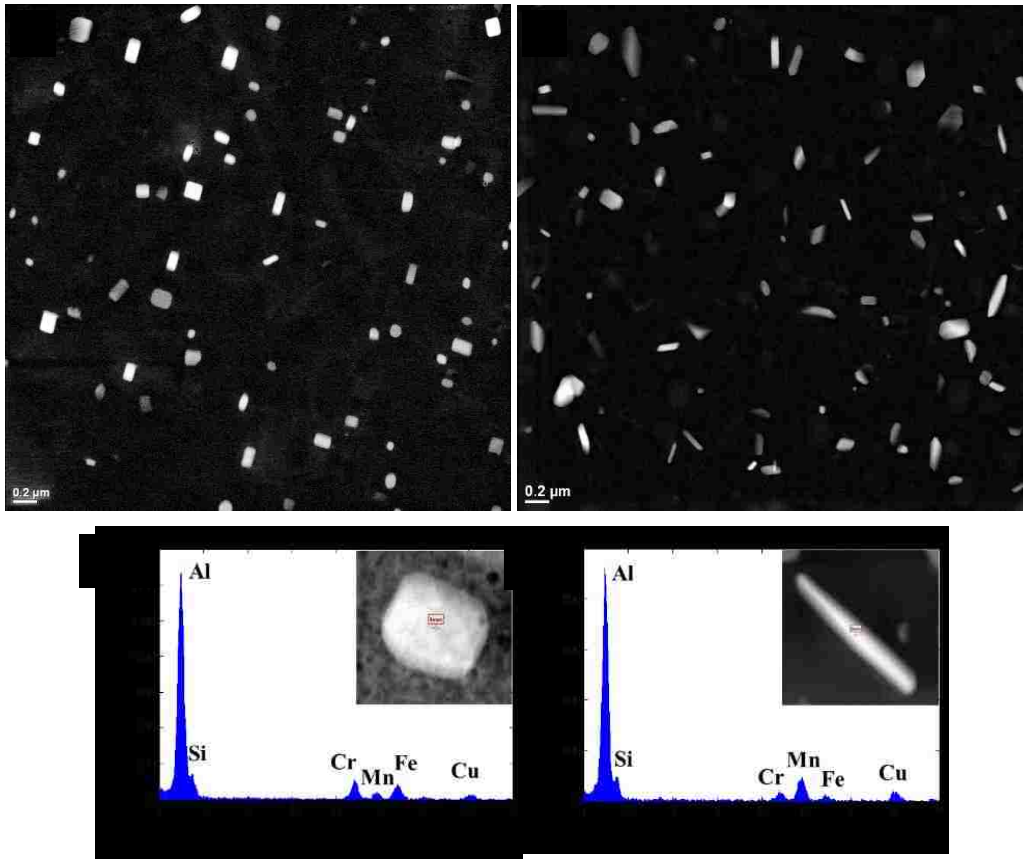

Figure 4.5 STEM micrographs showing precipitation of α-dispersoids after homogenization at 560 ˚C for 4 hours in (a) alloy A and (b) alloy B; EDS of α-dispersoids in (c) alloy A and (d) alloy B.

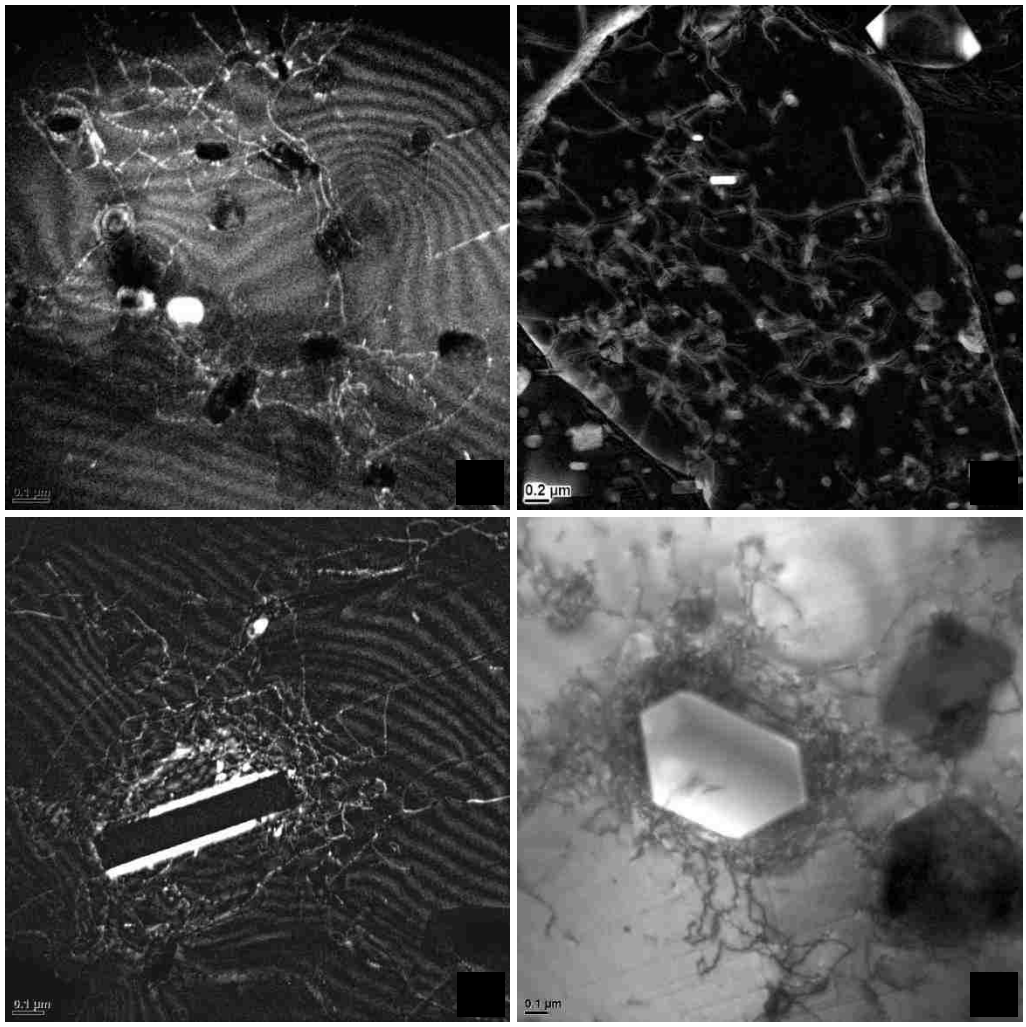

Figure 4.6 micrographs showing pinning effect of α-dispersoids on dislocations after upsetting at the temperature of 450 ˚C in (a) alloy A (WBDF mode) and (b) alloy B (DF mode); dislocations interaction with submicron-sized dispersoids in (c) alloy A (WBDF mode) and (d) alloy B (BF mode).

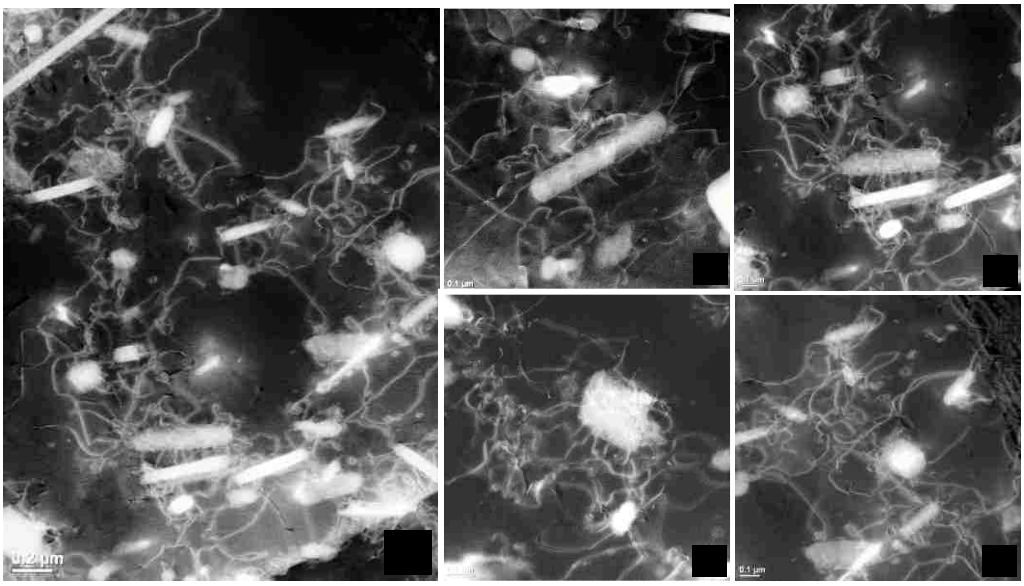

Figure 4.7 (a) STEM micrographs of alloy B showing pinning effect of α-dispersoids on dislocations; (b)-(e) magnification of (a), showing details of submicron-sized dispersoids interacting with dislocations after upsetting at the temperature of 450 ˚C.

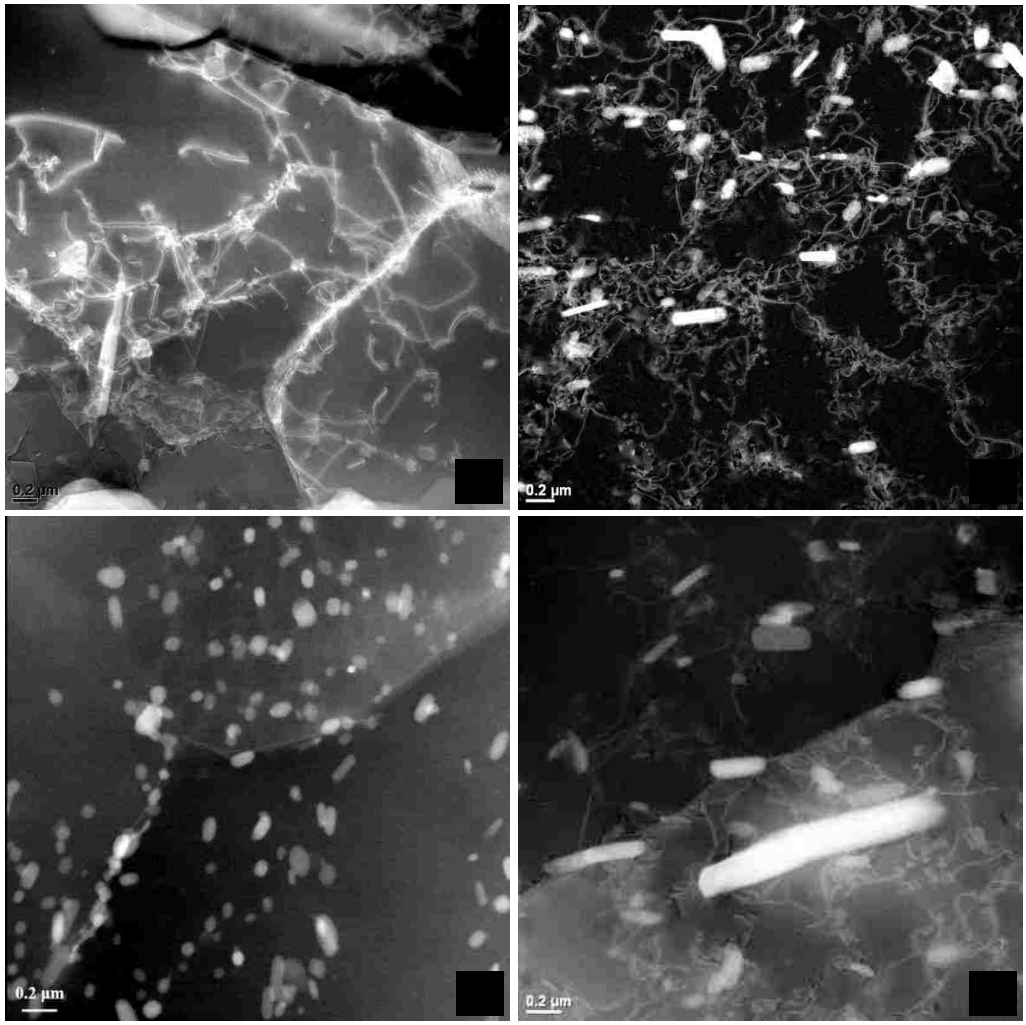

Figure 4.8 STEM micrographs showing pinning effect of α-dispersoids on dislocation cells and grain boundaries in (a) and (c) alloy A and (b) and (d) alloy B after upsetting at the temperature of 450 ˚C.

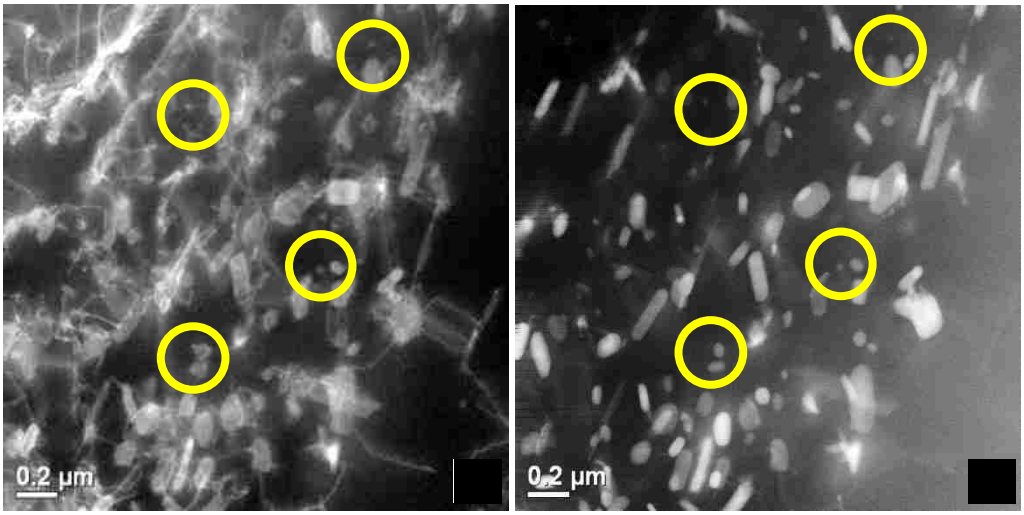

Figure 4.9 STEM micrographs showing interaction of submicron-sized dispersoids with dislocations in alloy B using (a) ADF mode (dislocations revealing) and (b) HAADF mode (Z contrast).

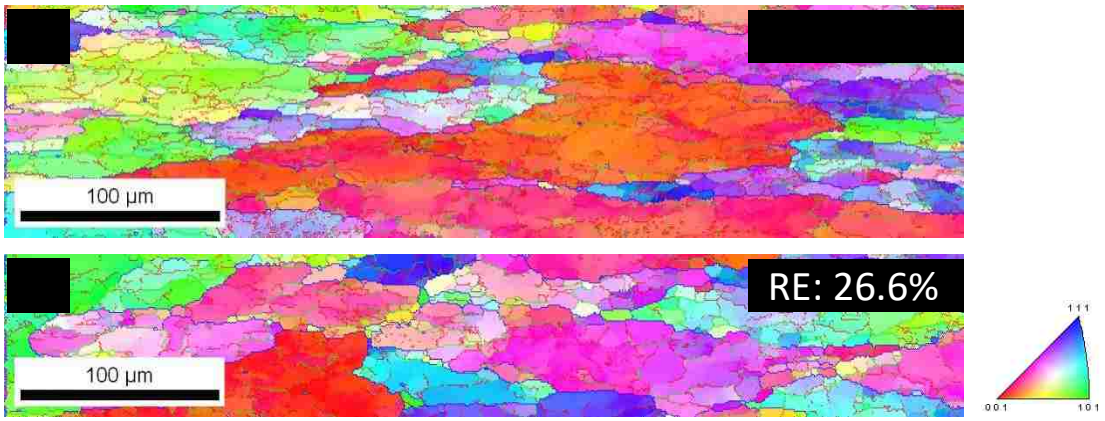

Figure 4.10 Orientation maps of alloy A after (a) upsetting at 450 °C and (b) following solid solution heat treatment at 560 °C for 1 h. Red lines correspond to misorientation angle > 2°, green lines > 5°, and blue lines > 15°, respectively.

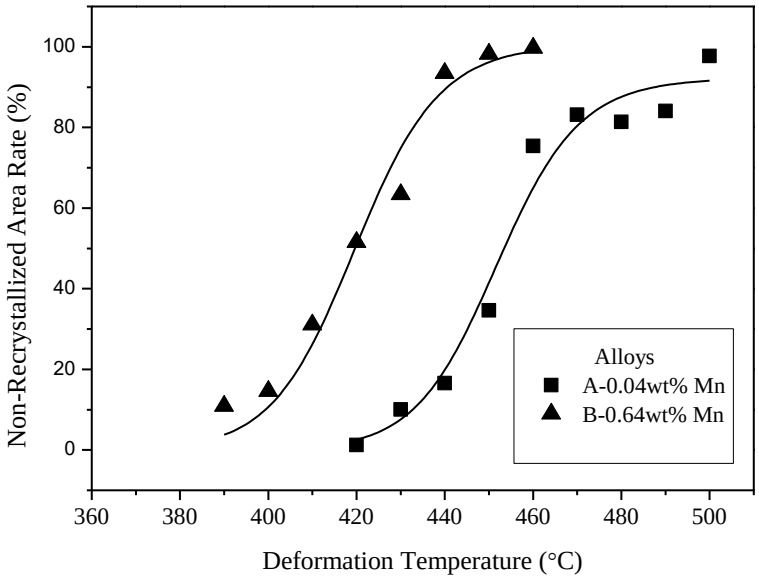

Figure 4.11 The relationship between non-recrystallized area fraction and upsetting temperature in the two alloys.

Chapter 5 The formation mechanism of Manganese-induced precipitation in a modified AA6061 (Al-Mg-Si-Cu) Al alloy during homogenization

5.1 Introduction

As previously described, nucleation of α-dispersoids is often believed to be heterogeneous. Several sites for heterogeneous nucleation have been suggested. Hirasawa [54] proposed that β”-and β’-Mg_2Si needles or even plate-like β-Mg_2Si phase could act as the preferential nucleation sites for the Mn-containing α-dispersoids in Al-Mg-Si alloys containing Mn. Hu et al. [48] suggested that, during homogenization of an AA6082 Al alloy with the addition of Mn, the needle shaped β’-Mg_2Si phase was first formed along <100> directions in the Al alloy, and at higher temperature, α-dispersoids were preferentially nucleated on β’-Mg_2Si needles, leading to the dissolution of the β’-phase. However, there has still been a lack of sufficient experimental evidence to support these suggestions. Lodgaard and Ryum [20,45] studied the nucleation mechanism of α-dispersoids in Al-Mg-Si alloys with various amounts of Mn and Cr during high temperature annealing. It was found that a rod-shaped intermediate phase, called ‘u-phase’ with a hexagonal structure and containing dispersoids-forming elements, was nucleated on the pre-formed β’-phase. Consequently, it was suggested that the u-phase was the precursor phase for the formation of α-dispersoids. Despite the formation of α-dispersoids in 6xxx series Al alloys has been investigated for two decades, its mechanism is still not fully understood. For example, the role of each of the elements (Mn, Cr, Fe and Si) involved in forming the dispersoids is still unclear. In addition, it is also desirable to understand how Cu influences the precipitation process of the dispersoids in a 6xxx series Al alloy with an addition of Cu.

In this chapter, the formation mechanism of α-dispersoids during homogenization in an AA6061 Al alloy modified with the addition of Mn, Cr and Cu was investigated using STEM and 3-D atom probe tomography (APT). It was found, for the first time, that Mn played a critical role in the formation of the α-dispersoids by first segregating to the interface of Q-phase, triggering dissolution of the Q-phase and then formation of a string of Mn-rich clusters which soon grew into α-dispersoids by participation of Si, Fe and Cr,

respectively. The strengthening of the alloy due to high temperature annealing was also quantitatively discussed.

5.2 Experimental details

The ingot of a Mn and Cr-containing Al-Mg-Si-Cu alloy, with 127 mm in diameter and 1500 mm in length, was prepared by direct-chill (DC) casting at Suzhou Research Institute for Nonferrous Metals, China. The nominal chemical composition of the alloy includes Mg 0.81, Si 0.80, Cu 0.43, Mn 0.64, Cr 0.26 and Fe 0.15 (in wt%). The cast alloy ingot was machined to make the billet with 100 mm in diameter and 250 mm in length, which was then homogenized in air at 460 or 550 $^{\circ}$C for 4 hours with a constant heating rate of 0.6 $^{\circ}$C min^{-1}, followed by water quenching. To investigate the early stage of precipitation during homogenization, several cast samples were directly heated to 460 $^{\circ}$C for isothermal annealing of 15 minutes and 2 hours, followed by water quenching. Optical microscopy, electron probe microanalysis (EPMA) and scanning electron microscopy (SEM) equipped with an energy dispersive spectroscopy (EDS) system were employed to investigate the microstructures in the as-cast and homogenized samples. Electrical conductivity and Vickers hardness measurements were performed on the alloy after 4 hours of homogenization between 460 and 550 $^{\circ}$C. Scanning transmission electron microscopy (STEM) and 3-D atom probe tomography (APT) were used to study the formation mechanism of fine α-dispersoids. STEM investigation was performed using a Hitachi 3300 scanning transmission electron microscope operated at 300 kV. TEM thin foils of the alloys were prepared by mechanical grinding, before twin-jet electropolishing at -10 $^{\circ}$C and 20 V in an electrolyte containing 70% methanol and 30% nitric acid. Energy dispersive spectroscopy (EDS) attached to the STEM was used to measure the composition of the precipitates observed. The thickness of TEM foils, where images were taken, was measured using electron energy loss spectroscopy (EELS), in order to determine the number density of α-dispersoids. The area fractions of precipitation free zones (PFZs) were measured with optical microscopy in the alloys etched with a Keller reagent. The statistic characteristics of dispersoids and area fractions of PFZs were analyzed using Image-Pro from the STEM and OM micrographs, respectively.

The specimens of 0.5 x 0.5 x 12 mm^3 for APT measurements were electropolished first in acetic acid with 30% perchloric acid at 20 V and second in an electrolyte of 5% perchloric acid in 2-butoxyethanol at 20 V until a sharp tip was formed. The tip sample was further sharpened using focus ions beam (FIB) to get rid of apex of specimens where few precipitates were left due to electropolishing. The radius of the milled needle was around 300 nm when the region of interest was located. A helium ion microscope was then used to remove the surface layer with Ga implantation resulting from FIB processing, to reduce the tip radius to less than 100 nm. The tip sample was analyzed in a local electrode atom probe (CAMECA LEAP 4000SI ®) under ultrahigh vacuum (~10^{-10} torr) and ultralow specimen temperature (20 ~ 26 K), UV laser energy of 30~50 pJ, pulse rate of 250~500 KHz. Reconstruction and analysis of APT data was conducted using Integrated Visualization and Analysis Software (IVAS®3.6.8). In order to identify the boundary between matrix and precipitates or dispersoids, isosurfaces with different Mg or Mn concentration were defined, which related the observed distribution of composition to theoretical models [177].

5.3 Results

5.3.1 The microstructure and distribution of Mn in the as-cast alloy

As shown in Figure 5.1(a), the as-cast alloy studied in this work showed a multi-phase dendritic microstructure which typically comprised of three types of intermetallic phases, mostly formed along grain boundaries (GBs). In SEM, these particles on GBs were in either a dark or a bright contrast (Figure 5.1(b)). As shown in Figures 5.1(c-i), EPMA measurements revealed that the particles of dark contrast contained mainly Si and Mg, thereby likely to be Mg_2Si phase, while the particles in a lighter contrast were mainly consisted of Fe, Cr, Si and Mn. They should be α-Al(FeMnCr)Si phase formed during solidification, since only the primary α-Al(FeMnCr)Si (or $Al_{15}(Fe,Mn)_3Si_2$ [22,189]) phase could be formed due to a relatively high content (0.64 wt. %) of Mn and its inhibiting effect on the formation of β-platelets in cast Al alloys. In addition, a small amount of roundish particles with a lighter contrast contained mainly Al, Mg, Si, and Cu, likely to be Q-phase inside grains [74]. It was interesting to note that Cu tended to segregate at GBs during homogenization (Figure 5.1(g)), though no Cu-containing phase existed at the

homogenization temperature, and that there were Mn depleted regions (i.e., the dark regions in Figure 5.1(i)) along the GBs where Mg_2Si phase was formed (Figures 5.1(f,i)). However, the Mn-depleted regions did not occur around a Mn-rich phase on a GB (Figure 5.1(i)). The average width of the Mn-depleted regions was about 6 μm. There were no depleted regions for Fe and Cr in the alloy after solidification. As will be discussed later in the paper, the formation of α-Al(FeMnCr)Si dispersoids was delayed in the Mn-depleted regions, indicating that Mn could play a significant role in triggering the dissolution of Q-phase, followed by the formation of α-Al(FeMnCr)Si dispersoids.

5.3.2 STEM analyses of precipitation at high temperature

5.3.2.1 Homogenization at 460 and 550 ˚C for 4 hours

Figure 5.2(a-c) are STEM micrographs showing the typical morphologies of the dispersoids formed in the alloy after homogenization at 460 ˚C and 550 ˚C for 4 hours, respectively. As shown in Figure 5.2(a), three typical morphologies of these dispersoids could be observed, i.e., thin rods, platelets, and fine blocks, after 4 hours of annealing at 550 ˚C. The dispersoids formed at 460 ˚C are illustrated in Figures 5.2(b,c). Similar to homogenization at 550 ˚C, rod-, plate- and fine block-like dispersoids were also observed at 460 °C. Some thin rod-shaped dispersoids (such as disperoids A and B in Figure 5.2(b)) were found to be actually platelets in shape, as their thickness were broadened by tilting the specimen by 25˚ around the axis shown in Figure 5.2(c). Meanwhile, a plate-like dispersoid labeled C in Figure 5.2(b) was shrunk to a smaller width, confirming that it was also a inclined platelet in shape. In contrast, a string of the fine block-like dispersoids circled in Figures 5.2(b,c) did not change their shape after the tilting, and therefore, they were likely to be blocks in shape.

EDS elemental analysis on STEM revealed that the three types of dispersoids formed at 460 ˚C (Figure 5.2(d)) were all consisted of mainly Al, Mn, Cr, Fe and Si, as shown in Figures 5.2(e-j). Cu was found to be almost uniformly distributed inside a grain and no Cu-rich phases existed in the alloy at this temperature (Figure 5.2(j)). All the fine block dispersoids within a string contained the almost same chemical composition, as illustrated in Figure 5.3. The dispersoids formed at 550 ˚C were also consisted of the same

composition as those at 460 °C. Because the dispersoid thickness (< 100 nm) were much smaller than the thickness (typically around 200 nm) of a TEM sample, the crystal structure of these dispersoids could hardly be analyzed using STEM in this work since the diffraction patterns from the selected area containing these dispersoids were dominated by the matrix. However, they were believed to be α-Al(MnCrFe)Si dispersoids, according to their morphologies and composition which were almost identical with those of α-Al(MnCrFe)Si dispersoids formed during high temperature homogenization treatment in AA6xxx Al alloys, as reported in literature [45,50].

5.3.2.2 Early stage of precipitation

In order to investigate the formation mechanism of these α-dispersoids during homogenization, the alloy was heated to 400 °C at a heating rate of 0.6 °C min^{-1}, or heated directly to 460 °C, for 15 minutes. The morphology of the precipitates formed in this early stage of precipitation is shown in Figure 5.4. Two distinct types of precipitates were observed, which were long lath-shaped particles along the $<100>_{Al}$ directions and little block-like particles. The corresponding EDS elemental mapping, as illustrated in Figure 5.5, indicates that the long lath-shaped precipitates contained Al, Mg, Si and Cu, which is considered to be Q-phase as explained in the discussion section, while Mn was a dominant element in the little block-like precipitates.

As shown in Figure 5.4(a), the existence of two distinct regions could be observed. It was found that, in region I, the lathe-shaped Q-AlMgSiCu phase was transferred into strings of Mn-rich precipitates, the details of which is illustrated in Figure 5.4(b), indicating that in the early stage of precipitation, the Q-phase provided nucleation sites for the strings of little block-like Mn dispersoids. In contrast to region I, the lathe-shaped Q-AlMgSiCu phase still remained in region Π, the reason of which will be explained in the following section with the help of APT. Similar results are also illustrated in Figure 5.4(d), and it is observed that some Q-precipitates remained unchanged in the surrounding area of the Mg_2Si constituent particle.

The different stages of the decomposition of Q-phase are shown in Figures 5.6 - 5.8. According to the EDS elemental mappings in Figures 5.5 and 5.6, the long lathe-like phase contained Mg, Si, Cu and Al, which was referred to as the Q-phase as mentioned before. The formation of Mn clusters on the Q-phase was observed at the beginning of the decomposition. In addition, Cu clusters were found on the Q-AlMgSiCu phase which was almost decomposed (Figure 5.8), indicating that upon the decomposition of the Q-phase, Mg and Si atoms first diffused away into the matrix, followed by Cu.

5.3.2.3 Intermediate stage of precipitation

The intermediate stage of precipitation of α-dispersoids was studied after homogenization of the directly heated alloy at 460 ˚C holding for 2 hours. As shown in in Figure 5.9, the small rod-, plate- and little block-like dispersoids were found to be formed at this stage of precipitation. In addition to these fine dispersoids, several large particles were observed, which were either located on the grain boundary or in the matrix. According to the corresponding EDS elemental mappings shown in Figures 5.10-5.12, all the three types of fine dispesoids contained Si besides Mn, and there was no obvious Fe and Cr existed in these dispersoids, which illustrates that after Mn cluster formation on the decomposing Q-phase, Si atoms subsequently participated, followed by Cr and Fe in the process of α-dispersoids formation. The large particles found at this stage could be classified into two types based on their compositions. Particle 2 was big α-Al(MnCrFe)Si constituent formed during casting, whereas particles 1, 3 and 4 were large Cu-bearing particles.

5.3.3 APT analyses of precipitation at the early stage

The 3-dimensional atom probe tomography (APT), with the capability of analyzing materials at the (sub)-nanometer scale, is unique in its ability to measure chemical composition of individual precipitate and solute segregation.

5.3.3.1 Heating to 350 ˚C (0.6 ˚C min^{-1}) or 460 ˚C (holding 15 min) and quenching

Lath-shaped Q-phase precipitates were observed in the specimen after heating to 350 ˚C with a heating rate of 0.6 ˚C min^{-1}. Figure 5.13(a) shows a typical three-dimensional (3-D) reconstruction of an analyzed volume in the specimen, and only Mg (red) atoms are

displayed for clarity. The Q-phase precipitates A and B are delineated by Mg isoconcentration surfaces. Figures 5.13(b-e) display the proximity histograms showing concentrations of Al, Mg, Si, Cu, Mn and Cr, which were used to analyze the composition of Q-phase precipitates as a function of distance normal to the 25 at% Mg isoconcentration surfaces. The location of the heterophase interface between the Q-phase precipitates and the Al matrix is indicated by the solid vertical line. On the right- and left-hand sides of the line, the spatial composition profiles of the Q-phase precipitates and the Al matrix are displayed, respectively. According to the proximity histograms, the Q-phase precipitates were rich in Cu, Mg and Si, the chemical composition of which was close to17Al-10Cu-46Mg-27Si at%. Compared to earlier reports [22,39,72,73], this composition was rich in Mg and lean in Al, which is similar to that of Wolverton - $Al_3Cu_2Mg_9Si_7$ (14.3Al-9.5Cu-42.9Mg-33.3Si at%) [69], obtained by first-principles calculations. This stoichiometry is identified as the most stable stoichiometric composition for the Q-phase, containing higher concentrations of Mg and Si at the expense of Al. In addition, the striking result is definitive evidence for localized Mn interfacial segregation within ~2 nm of the Al/Q-phase heterophase interface at this heating condition, as shown in Figures 5.13(c,e).

Figure 5.14(a) demonstrates another typical 3-D reconstruction after direct heating the specimen to 460 $^{\circ}$C holding for 15 minutes, which contains Q-phase precipitates. Q-phase precipitates are highlighted using a 4.5 at% Mg isoconcentration surface. Compositional analyses of the Q-phase precipitate using the proxigram methodology, displaying concentrations of Al, Mg, Si, Cu, Mn and Cr, are shown in Figures 5.14(b,c). The chemical composition of the precipitate A was approximately 29Al-4Cu-34Mg-32Si at%, similar to that of Matsuda et al. [77], with quite low concentration of Cu. However, compared to the precipitates in Figure 5.14, no obviously localized Mn solute segregation at the Al/Q-phase heterophase interface was detected. According to the APT results, higher concentration of Mn in the matrix near the Q-precipitates in Figure 5.13 could be obtained, compared with that in Figure 5.14. Calculations of the amount of Mn in the vicinity of the Al/Q-phase heterophase interfaces (-2 nm to 2 nm distance from the interfaces) were performed for the Q-phase precipitates labelled A in Figures 5.13 and 5.14, in order to quantitatively

differentiate the segregation effect of Mn, which were about 2.2 at%·nm for that in Figure 5.13 and 0.9 at%·nm for that in Figure 5.14, respectively.

Figure 5.15(a) displays another Q-phase precipitate in the 3-D reconstruction in the specimen after heating to 350 ˚C at a heating rate of 0.6 °C min^{-1}. Only Mg (red) atoms are displayed and the Q-phase precipitate is delineated by 1 at% Mg isoconcentration surface. Composition analyses of the Q-phase precipitate were performed, with the proxigrams displayed in Figures 5.15(b,c), in which considerable partitioning of Mn to the Q-phase precipitate could be observed. The Mn partitioning coefficients at positions A (3.95 nm from the heterophase interface) and B (5.55 nm from the heterophase interface) were calculated to be about 8 and 3, respectively. The Mn partitioning coefficient $K_{Mn}^{Q/Al} = \frac{c_{Mn}^{Q}}{c_{Mn}^{Al}}$ is the ratio of the Mn concentration in Q-phase precipitate divided by its value in the Al matrix, where c_{Mn}^{Q} and c_{Mn}^{Al} are the concentrations of Mn in the Q-phase precipitate and Al matrix, respectively. It could be thus predicted that after segregation of Mn at the Q/matrix interface, the partitioning of Mn to Q-phase could further accelerate the dissolution of Q-phase, and the corresponding transformation to Mn-bearing α-dispersoids.

5.3.3.2 Heating to 400 ˚C (0.6 ˚C min^{-1}) and quenching

Heating the specimen to 400 ˚C with a heating rate of 0.6 ˚C min^{-1} gave rise to both Q-phase precipitates and α-dispersoids, as illustrated in the 3-D reconstructions in Figures 5.16(a,d), in which the presence of Q-phase precipitates and α-dispersoids is indicated by arrows, and for clarity, only Mg (red) and Mn (green) atoms are displayed, respectively. Q-phase precipitates are delineated by 20 at% Mg isoconcentration surfaces, while α-dispersoids are highlighted by 7 at% Mn isoconcentration surfaces. Compositions of the Q-phase precipitates and α-dispersoids were analyzed employing the proximity histogram method as a function of distance normal to the 20 at% Mg and 7 at% Mn isoconcentration surfaces, respectively, as shown in Figures 5.16(b,c,e,f). The solid vertical lines indicate the locations of the heterophase interfaces between the Al matrix and the Q-phase precipitates or the Al matrix and the α-dispersoids. The spatial composition profiles of the Al matrix and Q-phase precipitates/α-dispersoids are illustrated on the left-and right-hand

sides of the lines, respectively. The atomic ratio of each precipitate is shown in these figures. It has been found that the decomposed Q-phase precipitate had the chemical composition of 17Al-9Cu-45Mg-29Si at%, almost the same as those in Figure 5.13. In addition, the formation of α-dispersoids proceeded, with the participation of other dispersoids-forming elements besides Mn, and notably, the atomic ratio of Mn/Si in α-dispersoids was close to 1, which could be kept until the end of the homogenization process.

Figure 5.17(a) demonstrates α-dispersoids in the 3-D reconstruction in the specimen after heating to 400 $^{\circ}$C with a heating rate of 0.6 $^{\circ}$C min^{-1}. Only Mn (yellow) atoms are displayed and the α-dispersoids are delineated by Mn isoconcentration surfaces. The proxigram methodology was used for the analysis of an α-dispersoid, by which the concentration was measured with respect to the distance from a 2.5 at% Mn isoconcentration surface. The proxigrams calculated based on this 2.5 at% Mn isoconcentration surface are displayed in Figures 5.17(b,c). The chemical composition of the dispersoid is 67.79Al-0.23Mg-12.75Si-1.98Cu-16.42Mn-0.70 Cr at% at position A (1.85 nm from the heterophase interface), and 66.37Al-0.22Mg-16.26Si-1.22Cu-15.60 Mn-0.22 Cr at% at position B (5.35 nm from the heterophase interface). It could be found that the atomic ratio of Mn/Si was also close to 1, and Mg almost diffused away into the matrix with little Cu remained, indicating its slow diffusion effect.

5.3.4 Influence of homogenization treatment on mechanical properties

As shown in Figure 5.18(a), after 4 hours of annealing at 550 $^{\circ}$C, the dispersoids have grown in size, while the amount of dispersoids decreased compared to those annealing at 460 $^{\circ}$C, due to the increased solubility and diffusion speed of Mn (Cr) at higher temperature, resulting in faster growth and coarsening of dispersoids. This is confirmed by the electrical conductivity measurement on the alloy after homogenization at different temperatures, as shown in Figure 5.18(b). According to Matthiessen's law [100,193], Mn, Cr and Fe have relatively greater contributions to increase the electrical resistivity (reciprocal of electrical conductivity) as compared to other elements. In the alloy studied, nearly all the Fe content formed constituent particles. The reduction of electrical conductivity after homogenization at 550 $^{\circ}$C compared to 460 $^{\circ}$C was due to the increased solubility of Mn (Cr) in the matrix,

which made plenty of finer dispersoids dissolve into the Al matrix. As described in [15,16], a remarkable dispersoid strengthening effect can be achieved by the precipitation of a large amount of fine dispersoids. However, the measured hardness of the alloy after annealing at 550 °C (with lower amount of dispersoids) was higher than that annealed at 460 °C (with higher amount of dispersoids), which should be attributed to the increased solute strengthening as a result of the dissolution of dispersoids and thus the increase of the concentration of solute elements in solid solution during higher temperature annealing. The strengthening mechanisms of the alloy will be discussed in the following section.

5.4 Discussion

5.4.1 Formation of Q-phase precipitates

It has been found that the quaternary Q-phase could be formed in a wide variety of Al alloys, including 2xxx series Al-Cu-Mg-Si alloys, 6xxx series Al-Mg-Si wrought alloys with Cu additions, and Al-Si-Mg-Cu casting alloys [30]. The crystal structure of Q-phase is generally considered to be hexagonal, with lattice constants a = 1.035-1.04 nm, c = 0.402-0.405 nm, and 21 atoms per unit cell [69,71,202]. The most detailed description of the structure was given by Arnberg and Aurivillius [71] based on Th_7S_{12} structure using single-crystal X-ray diffraction, in which Si atoms took the place of Th atoms, Al and Mg atoms replayed S atoms, and Cu atoms located at other sites that are not occupied in the Th_7S_{12} structure. The related Q'-phase is a metastable version of the equilibrium Q-phase and has the same crystal structure with slightly different lattice parameters and composition of $Al_4CuMg_6Si_6$ by Matsuda et al. [77]. The Q-phase usually forms as long laths or rods with their long axes parallel to $<001>_{Al}$ directions, and $\{150\}_{Al}$ is generally accepted as the habit plane [64,74]. The exact stoichiometry has been found to vary between different studies, for example, stated as $Al_4CuMg_5Si_4$ [22], $Al_5Cu_2Mg_8Si_6$ [39] and $Al_4Cu_2Mg_8Si_7$ [71] based on analyses of bulk alloys. First principles calculations were also used by Wolverton [69], which suggested an energetically preferred composition of $Al_3Cu_2Mg_9Si_7$. Additionally, the compositions of Q-phase in precipitate form have been reported to be $Al_5Cu_2Mg_8Si_6$ by Cayron et al. [72], and $Al_3CuMg_4Si_3$ by Biswas et al. [73], respectively. However, studies of the chemical compositions of the Q-phase precipitates are still limited. In the current study, STEM with EDS examination of the early stage of precipitation

indicates the formation of Al, Mg, Si and Cu-containing long lath-shaped particles along $<001>_{Al}$ directions, as shown in Figures 5.5 and 5.7. 3-D APT analysis of the particles were also performed in the alloy, presented in Figures 5.13-5.16. According to the lath-shaped morphology along $<001>_{Al}$ directions and the composition of Q-phase described in literature [64,69,73,74,77], the long lath-shaped particles observed are believed to be Q-phase precipitates formed during heating. Based on the APT results, various chemical compositions of the Q-phase precipitates were obtained. It was either rich in Mg and lean in Al, which is similar to that of Wolverton [69], or like that of Matsuda et al. [77], with quite low Cu concentration. In addition, localized segregation of Mn at the Al/Q-phase heterophase interface was observed after heating the alloy to 350 ˚C with a heating rate of 0.6 °C min^{-1}, illustrated by the shape of the Mn concentration profiles in Figure 5.13.

5.4.2 The triggering effect of Mn on the formation of α-dispersoids

As mentioned in Figures 5.4(a,d), two different regions could be identified by using STEM, and the reason why some lath-shaped Q-phase still remained in region Π while most of them were transferred into strings of Mn-rich nano-sized precipitates in region I could be explained based on the APT results obtained. In the early stage of homogenization, Mn tended to segregate to the interface between the Q-phase and the matrix (Figure 5.13) in Mn-rich region (region Π), where the lathe-shaped Q-AlMgSiCu phase was transferred into strings of Mn-rich precipitates, indicating that excess Mn was essential to induce the phase transformation from Q-phase to α-dispersoids. In contrast, the lathe-shaped Q-AlMgSiCu phase remained unchanged in Mn-poor region (region I), where Mn segregation could hardly occur at the Q/matrix interface (Figure 5.14), since there was insufficient Mn to trigger the transformation of Q-phase to α-dispersoids. The EPMA results in Figure 5.2(h) confirmed this analysis, which indicated the non-uniform distribution of Mn in the alloy, corresponding to the STEM result in Figures 5.4(a,d). Therefore, first in the areas rich in Mn, segregation of Mn at the Q/matrix interface led to the dissolution of lathe-shaped Q-AlMgSiCu phase, i.e., triggering the formation of α-dispersoids in the early stage of homogenization. Lodgaard and Ryum [45] investigated the nucleation mechanism of Mn and/or Cr-containing dispersoids in Al-Mg-Si alloys. An intermediate phase with hexagonal structure and rich in Mn and/or Cr, referred to as the ‘u-phase", was considered

to be the initial stage for formation of the dispersoids. In the present study, Cu was added into the Al-Mg-Si alloy, in which new phases, e.g., Q-phase, were formed during heating, and the dispersoids formation mechanism could be thus changed. Based on the results obtained above, the Q-phase was the precursor phase for the formation of α-dispersoids, and Mn played a key role during this process.

5.4.3 Formation mechanism for α-dispersoids during homogenization

According to the results obtained above, a description of the formation mechanism for the α-dispersoids during homogenization could be given. Since the α-dispersoids formed during homogenization have an incoherent interface to the Al matrix, homogeneous nucleation are practically impossible, and thus heterogeneous nucleation sites need to be found. In the current study, during continuous heating, the Q-AlMgSiCu phase was first precipitated into the matrix, with the driving force of the supersaturation of Mg, Si and Cu. When reaching ~350 ˚C, Mn atoms were segregated at the interface between the lathe-shaped Q-AlMgSiCu phase and the Al matrix in regions highly enriched with Mn, and subsequently Mn-rich clusters were formed in the place of the Q-phase upon its dissolution, which acted as the precursor phase for the formation of α-dispersoids. With increasing temperature, more Mn precipitated from the supersaturated solid solution, and the precipitation of Mn-rich dispersoids extended to the Mn-depleted regions with the increase of the diffusion speed of Mn, where lath-shaped Q-phase still remained due to the insufficiency of Mn to trigger the transformation of Q-phase to α-dispersoids. With the increase in the temperature and time, α-dispersoids gradually evolved with the participation of other dispersoids-forming elements besides Mn, and finally the Q-phase precipitates completely dissolved. Therefore, the final result was a breaking up of the original Q-phase precipitate into a string of α-Al(MnCrFe)Si dispersoids (Figure 5.3). After nucleation, the α-dispersoids grew at the expense of supersaturated dispersoids-forming elements in the surrounding matrix, and some of the block-like α-dispersoids evolved into rods and platelets. The number density of the dispersoids increased with the increase in temperature and time, reaching a maximum at ~460 ˚C (Figure 5.18). At higher temperature, coarsening occurred, resulting in the number density decrease and size increase of the dispersoids due to the increase of the solubility of Mn (Cr).

In the current study, Q-phase was considered to be the precursor phase for the formation of α-dispersoids, and Mn was essential to trigger the phase transformation from Q-phase to α-dispersoids. The segregation and partitioning of Mn to Q-phase might be energetically favorable to induce α-dispersoids formation. Heterophase interfacial Si solute segregation at the (semi)-coherent Al/θ'-Al_2Cu interface was studied by Biswas et al. [203,204]. First-principles calculations were employed to provide an energetic basis for the measured segregation behavior. Segregation energy as a function of position relative to the interface was assessed for each substitution site by Si near the interface in either the Al matrix or the θ'-precipitates based on the existed interface structure models, and certain sites were thus predicted to be energetically preferable for segregation of Si. The energetics of Zn solute partitioning to the Q-phase from the Al matrix were also assessed using first-principles calculations by Biswas et al. [73]. In the calculations, the crystal structure and $Al_3Cu_2Mg_9Si_7$ stoichiometry proposed by Wolverton [69] were adopted, which were obtained based on first-principles calculations on the partial structure suggested by Arnberg and Aurivillius [71]. Nine distinct sites regarding Al, Cu, Mg and Si in the unit cell of the Q-phase were possible sites for Zn substitution, and the partitioning energy of Zn for each site was calculated. Although the Zn partitioning to the Q-phase was energetically unfavorable, the partitioning of Mn was probably energetically favorable in the present study, since Mn automatically diffused into the Q-phase, which was different to the presence of Zn in Q-phase in [73], explained by trapping of Zn within the Q-phase precipitate due to slow diffusion after participation of Zn to the nucleation of Q-phase. The critical role of Mn partitioning in the formation of ordered NiAl nanoparticles in ferritic steels has been examined by Jiao et al. [205]. Atomistic structural analyses, with the help of first-principles calculations, revealed a strong thermodynamic driving force favoring Mn atom partitioning to Al sublattice in NiAl nanoparticles. The similar calculations could be performed in our study as the next step to provide quantitative explanations of segregation and partitioning of Mn to the Q-phase, observed in the experimental results, which induced the formation of α-dispersoids during homogenization process.

5.4.4 Strengthening mechanisms

In current high temperature homogenization treatments, the evolution of mechanical properties could be mainly attributed to the synthetic effect of solid solution and dispersoid hardening, with negligible influence of other strengthening mechanisms. As shown in Figure 5.18(b), the Vickers hardness ($HV_{0.1}$) was measured to be 57.6 ± 5.2 and 66.4 ± 2.7 after 4 hours of annealing at 460 ˚C and 550 ˚C, respectively. According to the relationship between the indentation hardness and the flow (yield) stress of materials, $HV = 3\sigma_{flow}$ [206], the enhanced strength was calculated to be about 29 MPa (3 to 56 MPa based on deviations) after higher temperature annealing (550 ˚C).

The strengthening effect caused by dispersoids (dispersoid hardening), due to the Orowan bowing mechanism, could be estimated by the Ashby-Orowan equation [207]

$$\sigma_P = \frac{0.84MGb}{2\pi(1-\nu)^{1/2}\lambda} ln\frac{r}{b} \quad (5.1)$$

where σ_P is the increase of yield strength; M is the Taylor factor, M = 3.06 for FCC Al; G is the shear modulus of Al matrix, G = 27.4 GPa; b is the Burgers vector of dislocations in Al, b = 0.286 nm; ν is the Poisson ratio, ν = 0.33 for Al; and λ is the interspacing of dispersoids, which depends on the radius r and volume fraction V_V of dispersoids

$$\lambda = r\left(\frac{2\pi}{3V_V}\right)^{1/2} \quad (5.2)$$

The volume fraction (V_V) of dispersoids was calculated using the same procedure as described by Li and Arnberg [188] and shown in Equation 5.3

$$V_V = A_A \frac{\bar{K}\bar{D}}{\bar{K}\bar{D}+t}(1 - A_{PFZ}) \quad (5.3)$$

where $\bar{K}$ is the average shape factor of dispersoids, accounting for the shape of the dispersoids; $\bar{D}$ is the average equivalent diameter of dispersoids measured from STEM images, which is defined as the diameter of a circle with equivalent area, and given by [208],

$$\bar{D} = \frac{1}{n}\sum\left(\frac{4A_p}{\pi}\right)^{1/2} \quad (5.4)$$

Where A_p is the dispersoids area; n is the number of measured dispersoids; t is the TEM foil thickness; and A_A and A_{PFZ} are the area fractions of dispersoids from STEM observation and PFZs from OM measurements, respectively. In this study, $\bar{K}$ was modified to equal

0.41 at 460 ˚C and 0.38 at 550 ˚C according to the shape of dispersoids in TEM observations [188].

By using the measured parameters of dispersoids in the alloy after homogenization at 460 ˚C and 550 ˚C holding for 4 hours, the contribution of the dispersoids to the yield strength could be calculated, which is listed in Table 5.1 with the values of dispersoids parameters. According to Eqs. (5.3) and (5.4), the yield stress due to dispersoid strengthening increased with increasing volume fraction and decreasing size of dispersoids.

The solid solution strengthening contribution to the yield stress was determined using the atom probe results for the concentration of solute atoms in solid solution. The individual contributions of the solutes are obtained from the recent calculations of Leyson et al. [13]

$$\tau_{sol}^{i}(T) = \tau_{y0}^{i}\left[1 - \left(\frac{kT}{\Delta E_b} ln \frac{\dot{\varepsilon_0}}{\dot{\varepsilon}}\right)^{2/3}\right] \quad (5.5)$$

where

$$\tau_{y0}^{i} = k_i C_i^{2/3},\ E_b = k_i' C_i^{1/3} \quad (5.6)$$

C_i is the concentration (in at%) of the different solute elements determined from the atom probe analysis, as shown in Table 5.2, and the values of k_i and k_i' are listed in [13]. The values of $\dot{\varepsilon}$ and $\dot{\varepsilon_0}$ have been assumed to be 2 x10^{-3} s^{-1} and 10^7 s^{-1}, respectively [209]. For the multi-solute case, the zero-temperature strength and characteristic energy barrier are

$$\tau_{y0} = \left[\sum_i \left(\tau_{y0}^{(i)}\right)^{3/2}\right]^{2/3}, \Delta E_b = \left[\sum_i \left(\Delta E_b^{(i)}\right)^3\right]^{1/3} \quad (5.7)$$

Using Eqs. (5.5) - (5.7), the flow stress of the alloy, which contains the solutes of Mn, Cr, Cu, Mg and Si, could be predicted. The predicted shear flow stresses were multiplied by the Taylor factor, *M* = 3.06, to obtain the flow stresses values, as shown in Table 5.1.

According to the calculated results (Table 5.1), the general trends for solid solution and dispersoid strengthening during homogenization were captured, and the predicted strength change of the alloy after annealing at 460 ˚C and 550 ˚C is approximately 5 MPa, barely lying in the range of the measured change of strength. As mentioned in [13], the presence of ppm Fe may also have an influence on the strength, which could further increase the

solid solution strengthening effect in the alloy. However, no peak corresponding to Fe was observed in APT and this is probably because its intensity was too weak by comparison with the tail of the Al peak since the Fe concentration in the matrix was extremely low. In addition, the difference between predicted and experimental flow stresses still exists [13], and more accurate model for prediction of solid solution hardening effect thus needs to be developed. In sum, although some improvement should be achieved in the future, the current predicted results shows generally reasonable agreement with the experiments, which provides a useful analysis method to quantitatively estimate the solid solution and dispersoid strengthening effects during homogenization of Al alloys.

5.5 Conclusions

(1) Three typical morphologies of fine α-Al(MnCrFe)Si dispersoids, i.e., rods, platelets and fine blocks, were observed in the alloy after 4 hours of homogenization treatment at 460 and 550 °C, respectively. Strings of fine block-like α-dispersoids were also found after the homogenization treatment at 460 °C.

(2) Mn distributed non-uniformly with a Mn-depleted region surrounding the Mg_2Si constituent at GBs in the as-cast alloy. In the early stage of homogenization, in Mn-rich regions, Mn segregated at the interface between the long lath-shaped Q-phase and the matrix, which triggered the transformation of Q-phase into strings of Mn-rich precipitates. Meanwhile, Q-phase still remained unchanged in the Mn-depleted regions without segregation of Mn at the Q-phase/matrix interface. This indicated that the segregation of Mn was essential to induce the transformation of Q-phase into α-dispersoids, and that Q-phase was considered to be the precursor phase for the formation of α-dispersoids.

(3) With further increase in the homogenization temperature and time, α-dispersoids gradually evolved, with the participation of other dispersoids-forming elements in addition to Mn. The atomic ratio of Mn/Si was found to be close to 1 in the α-dispersoids when the dispersoids were fully developed.

(4) A significant dispersoid hardening effect could be achieved in the alloy after 4 hours of annealing at 460 ˚C, while after annealing the alloy at 550 ˚C for 4 hours, strengthening by a higher level of solid solution of alloying elements, such as Mn, Cr, Fe, Si, etc., played a more important role in determining the strength of the alloy, as a result of increasing dissolution of dispersoids thereby increasing the supersaturation of the alloying elements in the alloy at 550 ˚C.

Table 5.1 Characteristic of dispersoids and various contributions to the yield strength

Condition	Average equivalent diameter of dispersoids (nm)	Volume fraction of dispersoids (vol.%)	Dispersoids contribution to yield strength (MPa)	Solid solution contribution to yield strength (MPa)
460 °C/4 h	36	0.85	57	19.5
550 °C/4 h	80	1.29	38	43.5

Table 5.2 Solid solution compositions measured by atom probe after different annealing treatments (in at%)

Condition	Cr	Cu	Mg	Si	Mn
460 °C/4 h	0.073	0.214	0.564	0.256	0.09
550 °C/4 h	0.049	0.201	0.99	0.381	0.441

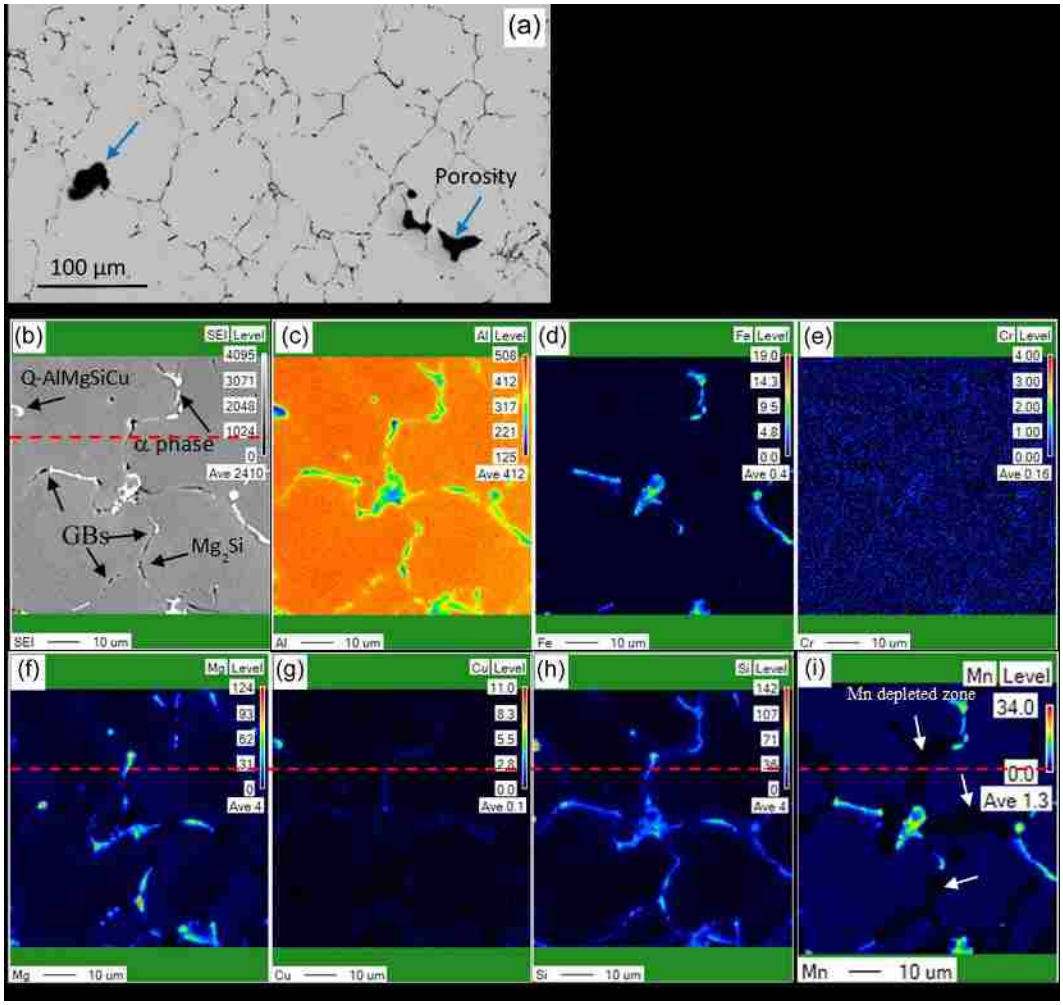

Figure 5.1 (a) Optical micrograph of the multi-phase dendritic structure in the as-cast alloy; EPMA maps for the as-cast alloy, (b) SEM micrograph of the alloy at higher magnification; and EPMA elemental maps: (c) Al distribution; (d) Fe distribution; (e) Cr distribution; (f) Mg distribution; (g) Cu distribution; (h) Si distribution and (i) Mn distribution with a line scan along the line.

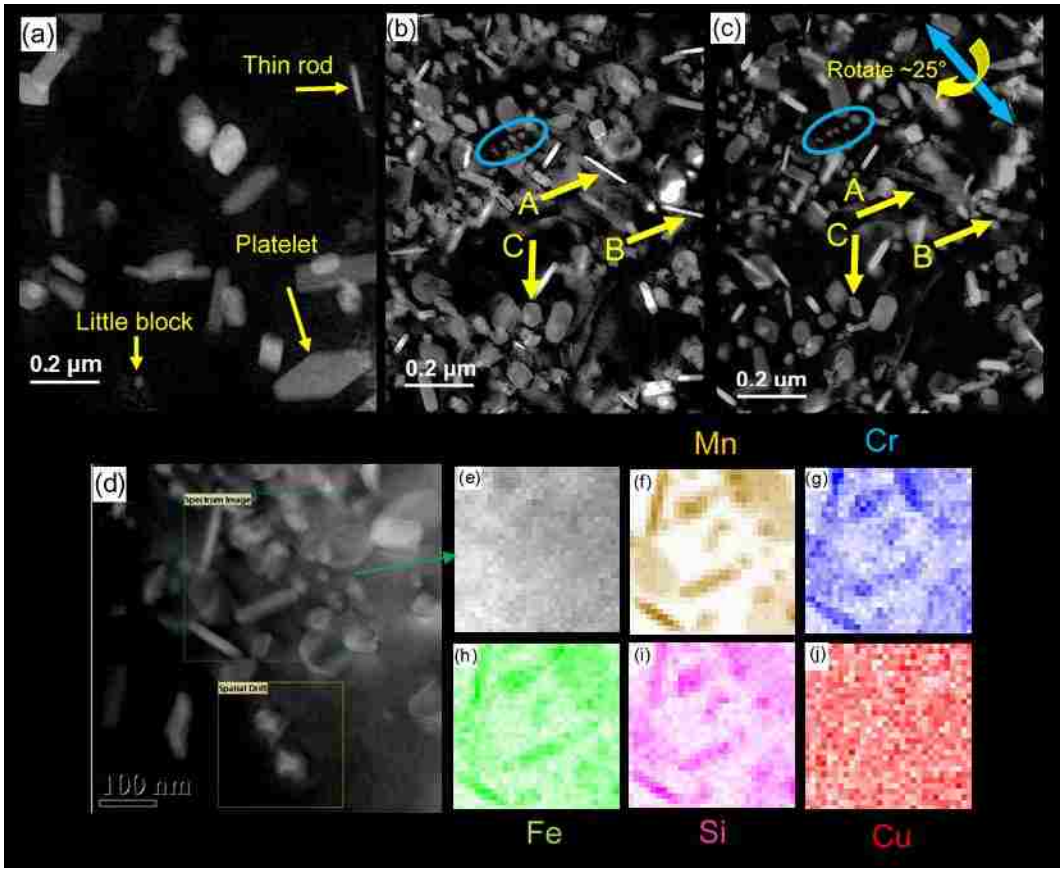

Figure 5.2 Dispersoids with different morphologies after homogenization. (a) Homogenization at 550 ˚C for 4 hours; (b) homogenization at 460 ˚C for 4 hours; (c) rotation by 25˚ of the same area in (b), some of the dispersoids changed morphology; EDS mapping of various types of high temperature dispersoids after homogenization at 460 ˚C holding for 4 hours with a heating rate of 0.6 ˚C min^{-1}; (d) STEM micrograph showing dispersoids; (e-j) EDS elemental maps of Al, Mn, Cr, Fe, Si and Cu, respectively, in the same area as the green frame in (d).

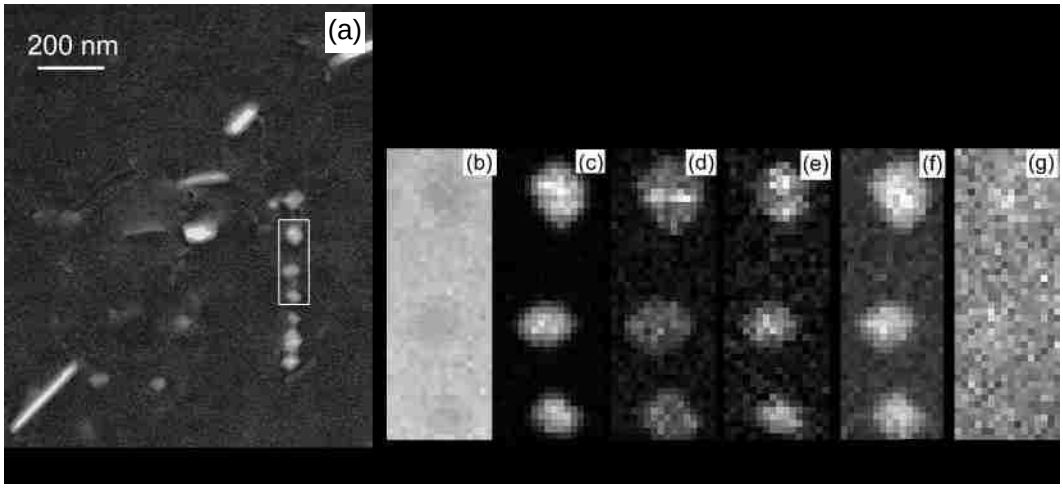

Figure 5.3 EDS mapping of a string of little block-like high temperature dispersoids after homogenization at 460 ˚C holding for 4 hours with a heating rate of 0.6 ˚C min^{-1}. (a) STEM micrograph showing dispersoids; (b-g) EDS elemental maps of Al, Mn, Cr, Fe, Si and Cu, respectively, in the same area as the white frame in (a).

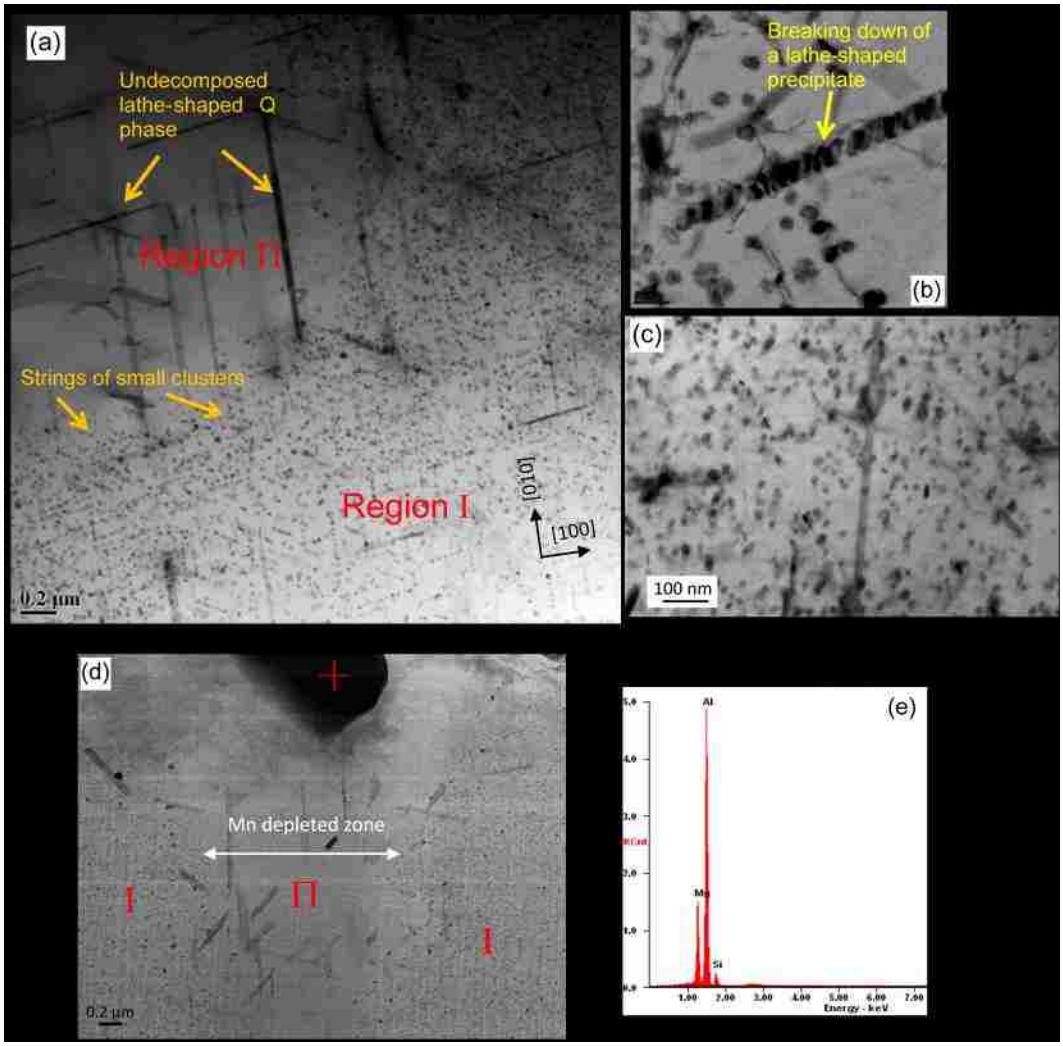

Figure 5.4 Morphology of the precipitates in the early stage of precipitation. (a) and (d) Two distinct types of precipitates - long lathe-like phase and little block-like phase existed after direct heating the alloy to 460 ˚C holding for 15 min, and then quenching in water; (b) magnified decomposed lathe-like phase with small clusters on it; (c) two distinct types of precipitates existed after heating the alloy to 400 ˚C with a heating rate of 0.6 ˚C min^{-1}, and then quenching in water; (e) EDS of the Mg_2Si particle in (d).

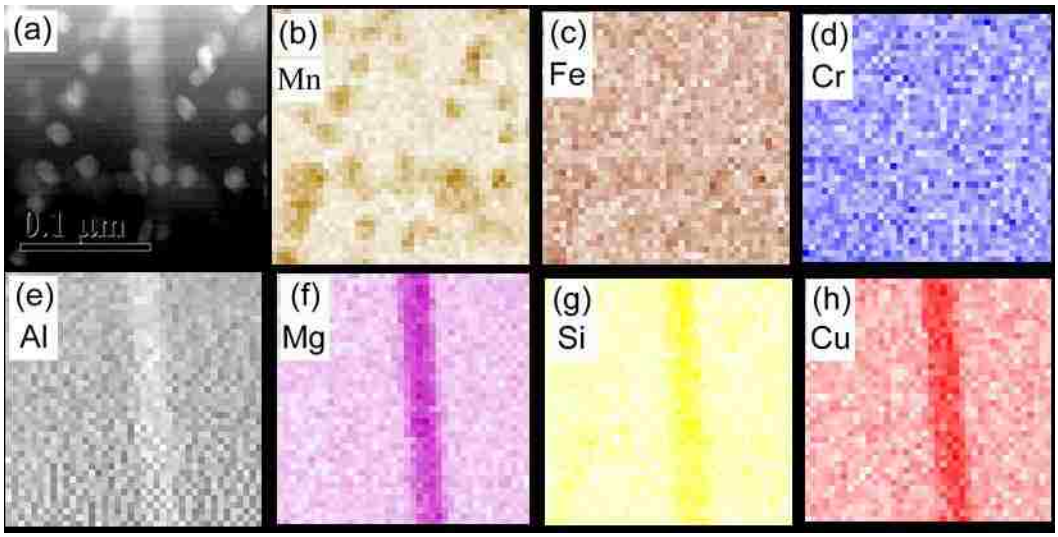

Figure 5.5 EDS mapping of the two types of precipitates. (a) STEM micrograph showing the precipitates; (b-h) EDS elemental maps of Mn, Fe, Cr, Al, Mg, Si and Cu, respectively, in the same area as in (a).

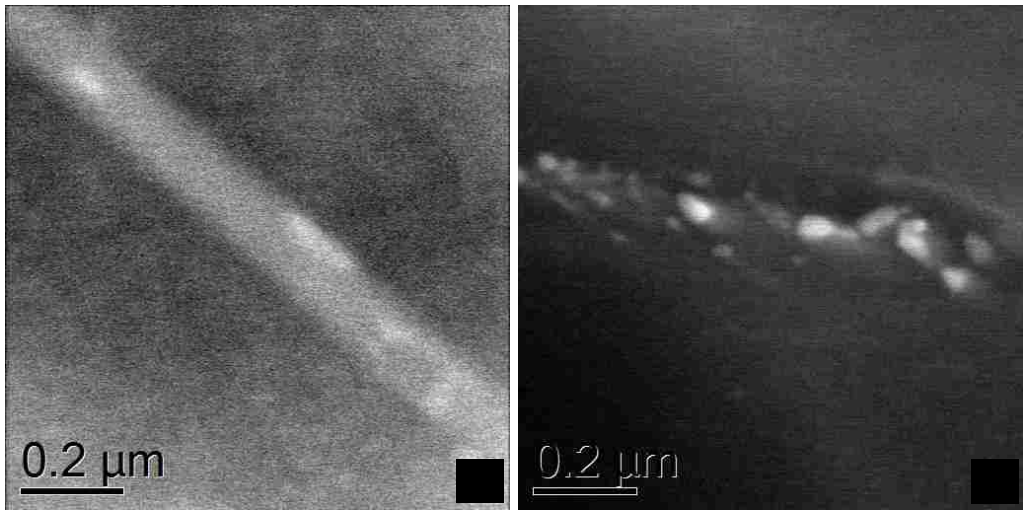

Figure 5.6 (a) Beginning and (b) end stages of the decomposition of Q-phase.

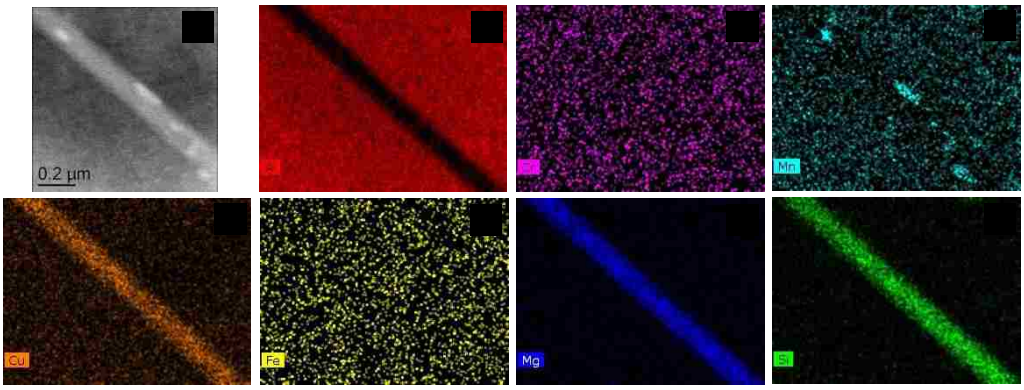

Figure 5.7 EDS mapping of the beginning of Q-phase decomposition corresponding to Figure 5.6(a). (a) STEM micrograph showing the phase; (b-h) EDS elemental maps of Al, Cr, Mn, Cu, Fe, Mg and Si, respectively, in the same area as in (a).

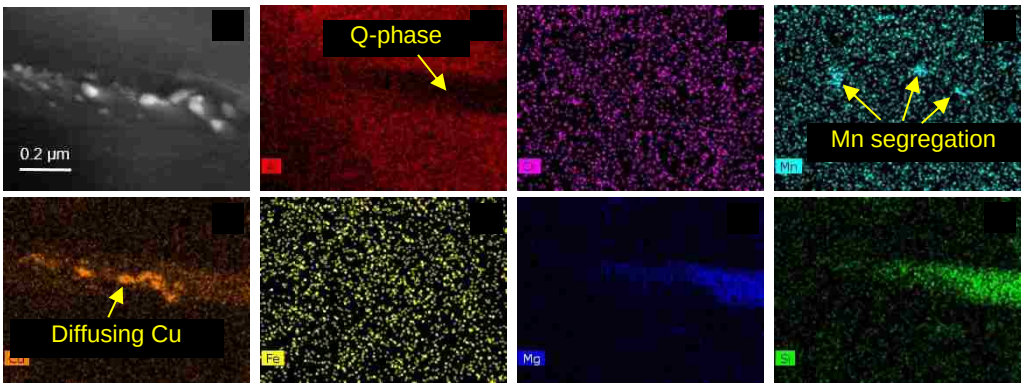

Figure 5.8 EDS mapping of the decomposed long-lath like Q-precipitate corresponding to Figure 5.6(b). (a) STEM micrograph of the decomposed precipitate; (b-h) EDS elemental maps of Al, Cr, Mn, Cu, Fe, Mg and Si, respectively, in the same area as in (a).

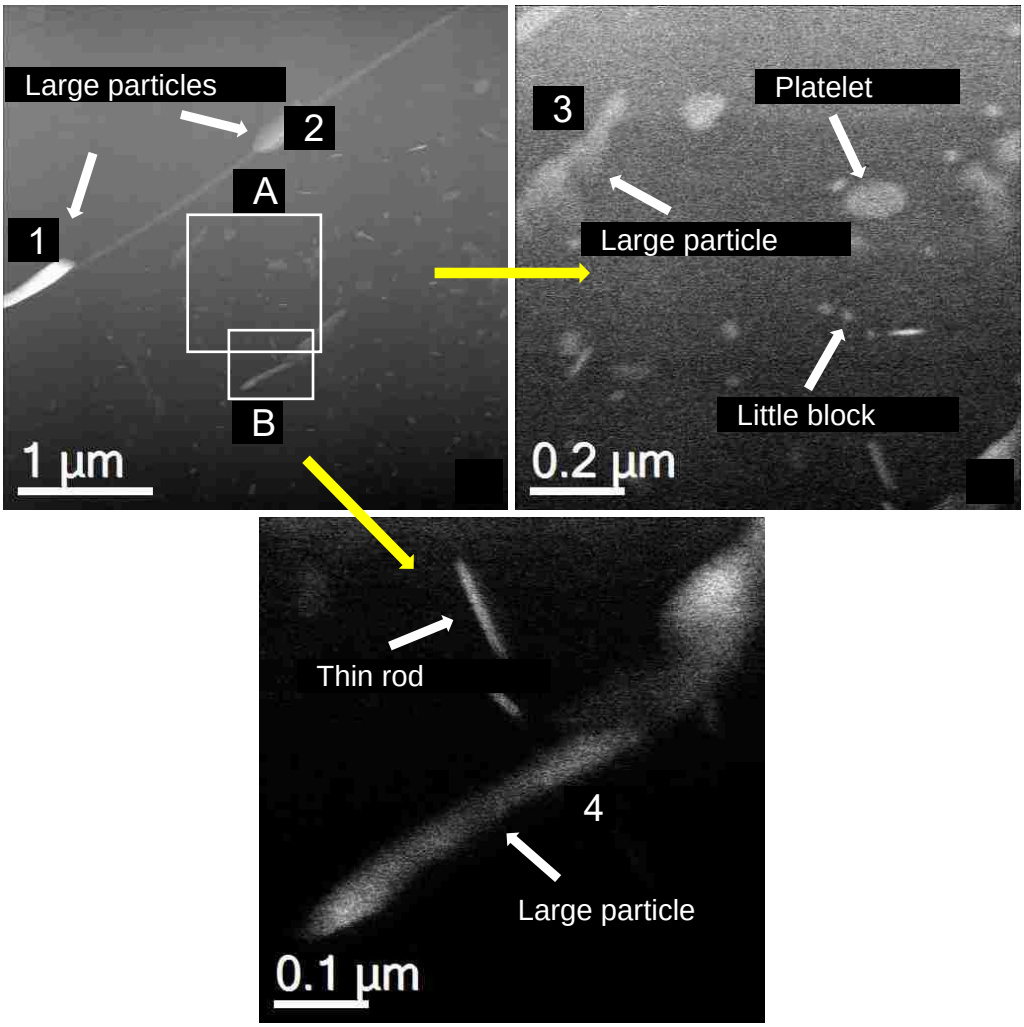

Figure 5.9 STEM micrographs showing precipitates after homogenization at 460 ˚C holding for 2 hours through direct heating. (a) Low magnification micrograph showing various types of precipitates; (b-c) higher magnification of areas A and B in (a), showing large particles and rod-, plate-, little block-like dispersoids.

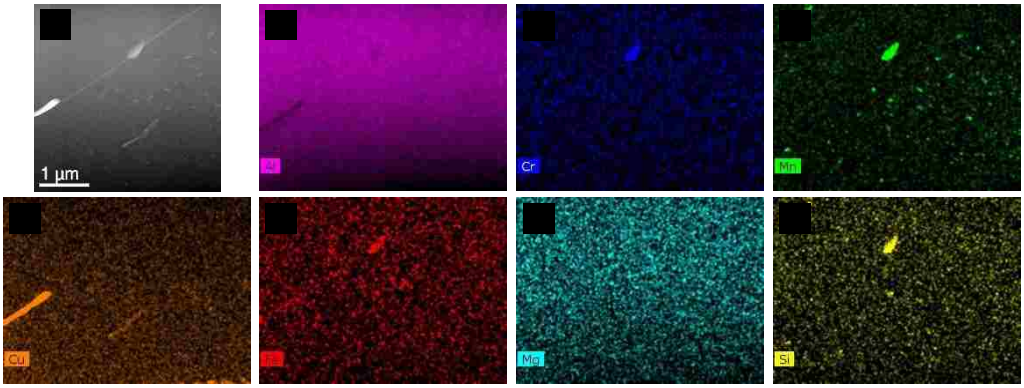

Figure 5.10 EDS mapping of the precipitates corresponding to Figure 5.9(a). (a) STEM micrograph of the precipitates; (b-h) EDS elemental maps of Al, Cr, Mn, Cu, Fe, Mg and Si, respectively, in the same area as in (a).

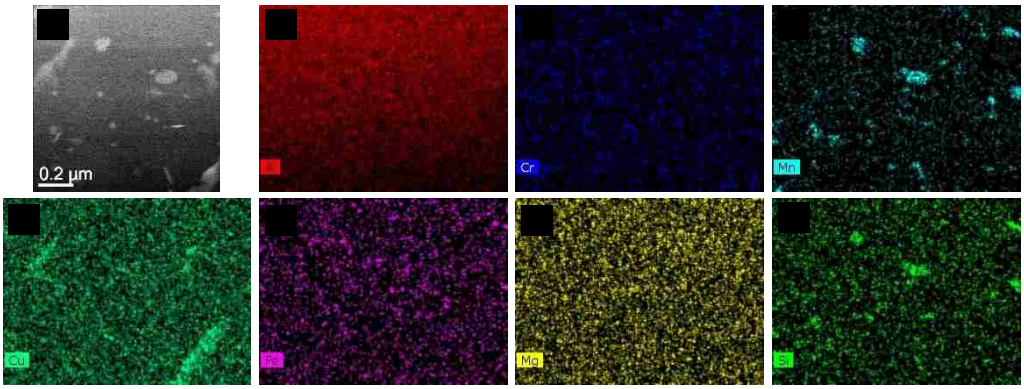

Figure 5.11 EDS mapping of the precipitates corresponding to Figure 5.19(b). (a) STEM micrograph of the precipitates; (b-h) EDS elemental maps of Al, Cr, Mn, Cu, Fe, Mg and Si, respectively, in the same area as in (a).

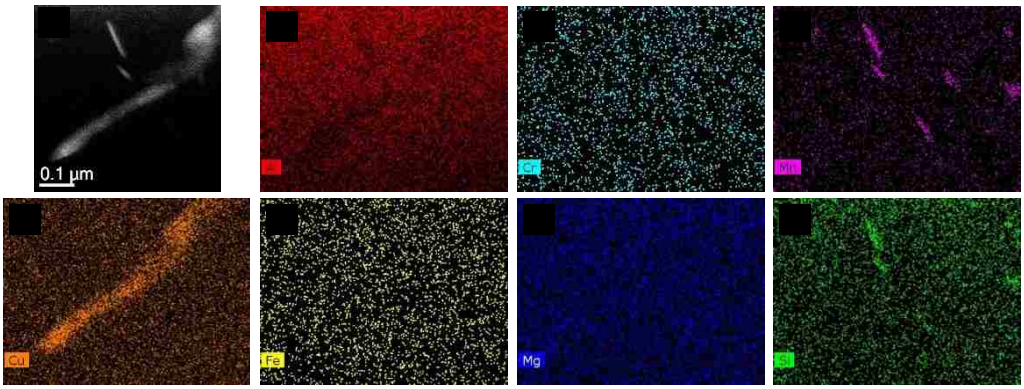

Figure 5.12 EDS mapping of the precipitates corresponding to Figure 5.9(c). (a) STEM micrograph of the precipitates; (b-h) EDS elemental maps of Al, Cr, Mn, Cu, Fe, Mg and Si, respectively, in the same area as in (a).

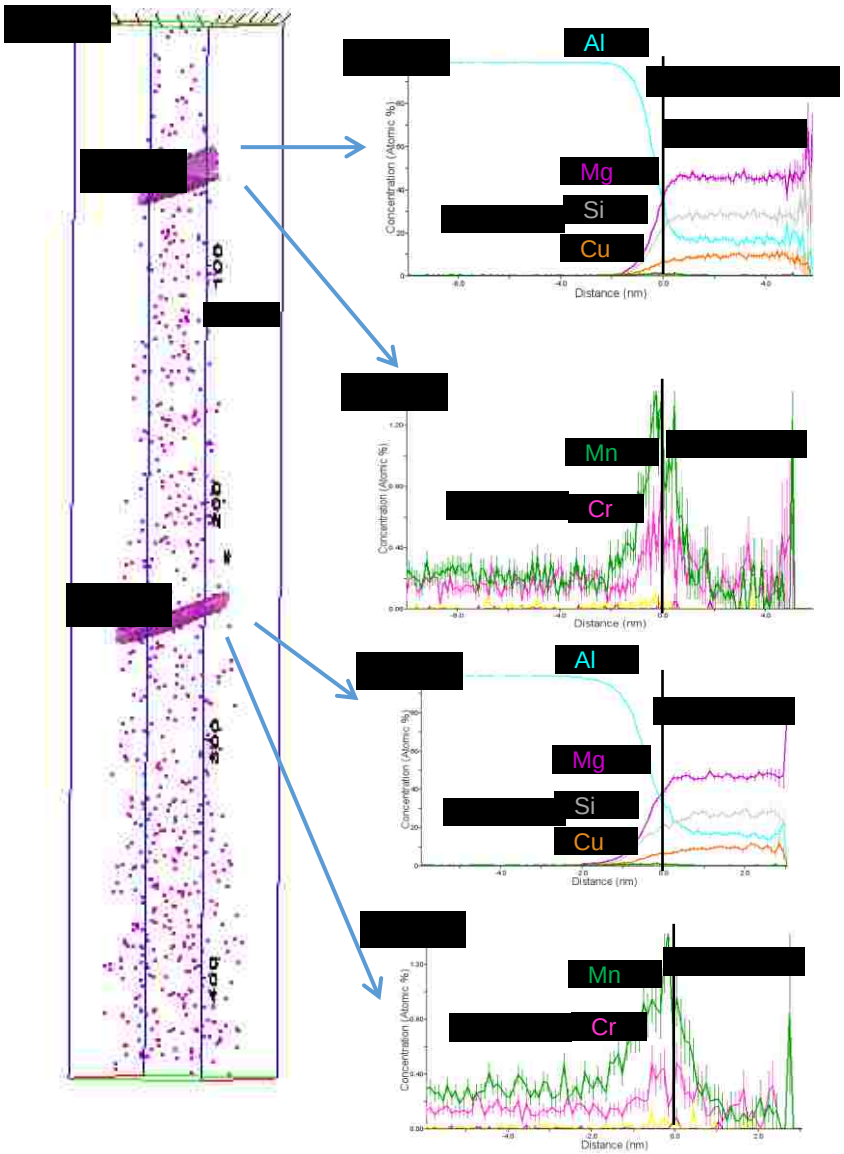

Figure 5.13 3-D reconstruction of the specimen after heating to 350 ˚C with a heating rate of 0.6 ˚C min^{-1} and quenching. (a) Mg isoconcentration surface delineates two Q-phase precipitates; (b) and (d) proximity histograms used to analyze the composition of the two Q-phase precipitates; (c) and (e) proximity histograms showing the segregation of Mn at the heterophase interfaces of Al matrix/Q-phase precipitates.

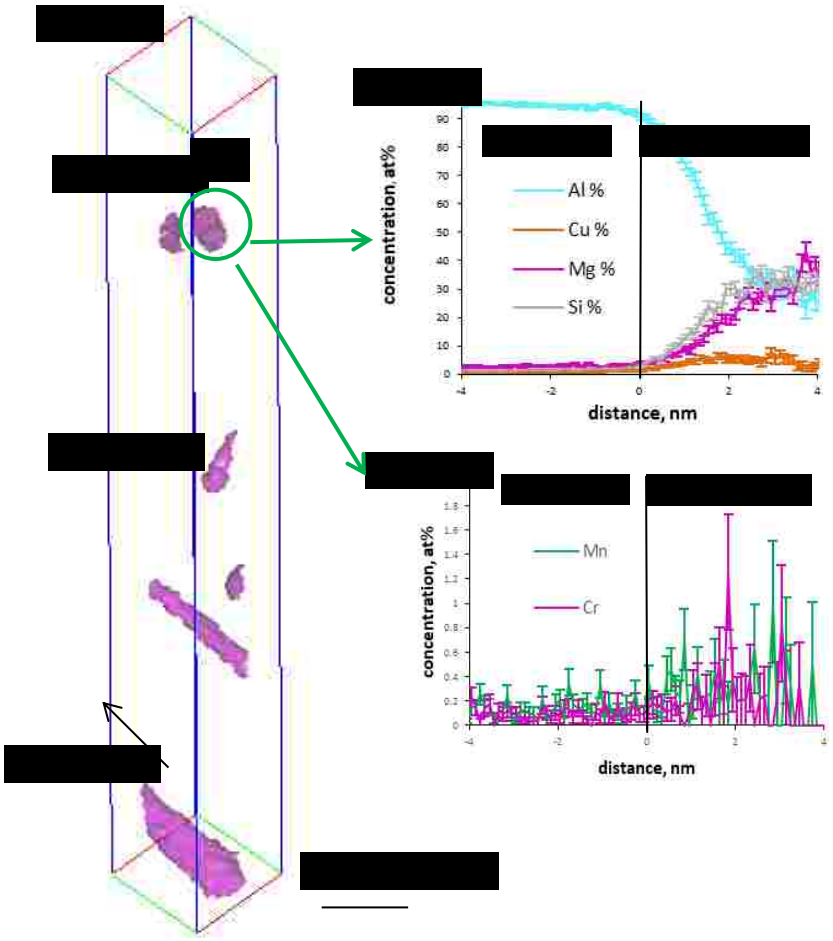

Figure 5.14 3-D reconstruction of the specimen after direct heating to 460 ˚C holding for 15 min and quenching. (a) Mg isoconcentration surface delineates Q-phase precipitates; (b) proximity histogram used to analyze the composition of the Q-phase precipitate; (c) proximity histogram showing the concentration profile of Mn in the vicinity of the heterophase interface of Al matrix/Q-phase precipitate.

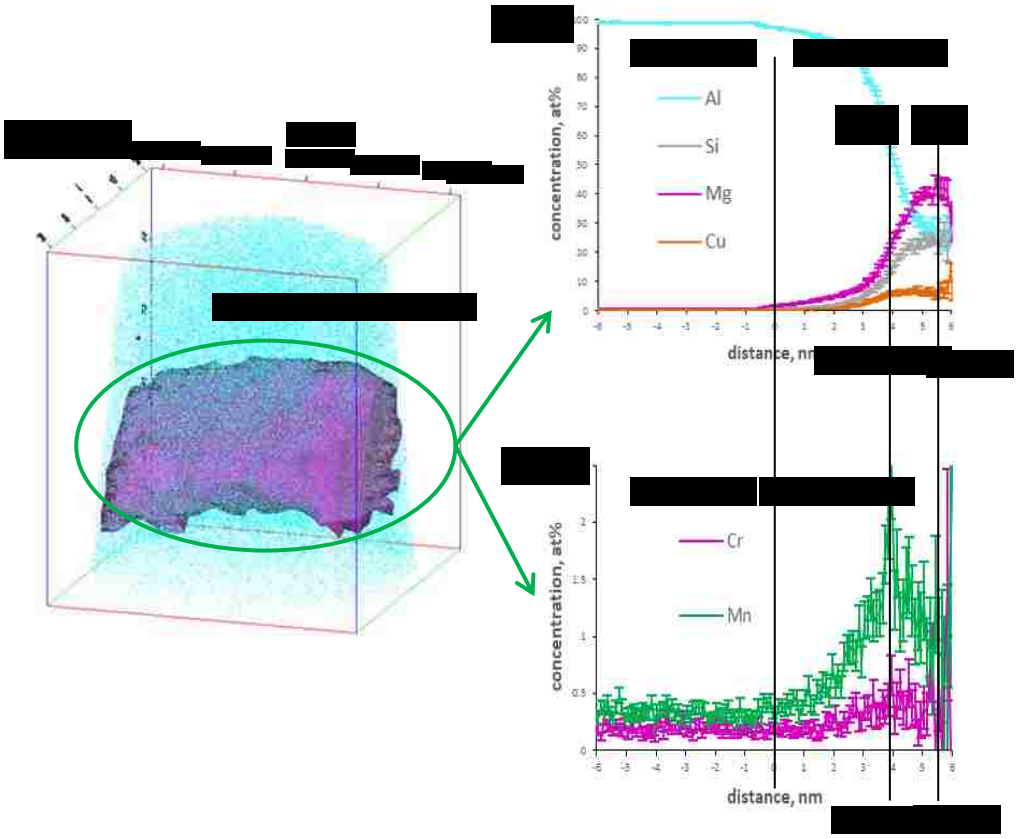

Figure 5.15 3-D reconstruction of the specimen after heating to 350 ˚C with a heating rate of 0.6 ˚C min^{-1} and quenching. (a) Mg isoconcentration surface delineates the Q-phase precipitate; (b) proximity histogram used to analyze the composition of the Q-phase precipitate; (c) proximity histogram showing the partitioning of Mn to the Q-phase precipitate.

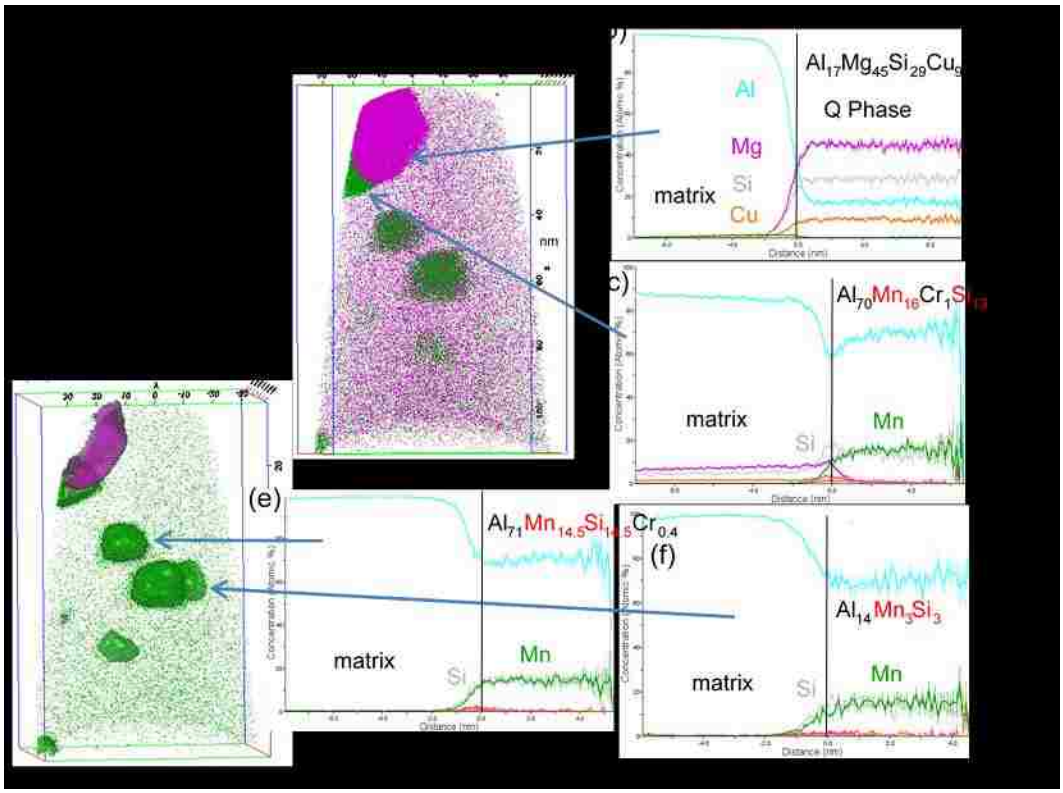

Figure 5.16 3-D reconstruction of the specimen after heating to 400 ˚C with a heating rate of 0.6 ˚C min^{-1} and quenching. (a) and (d) Mn (green) and Mg (red) isoconcentration surfaces delineate the α-and Q-phases, respectively; (b) proximity histogram used to analyze the composition of the Q-phase precipitate; (c), (e) and (f) proximity histograms used to analyze the composition of the α-dispersoids.

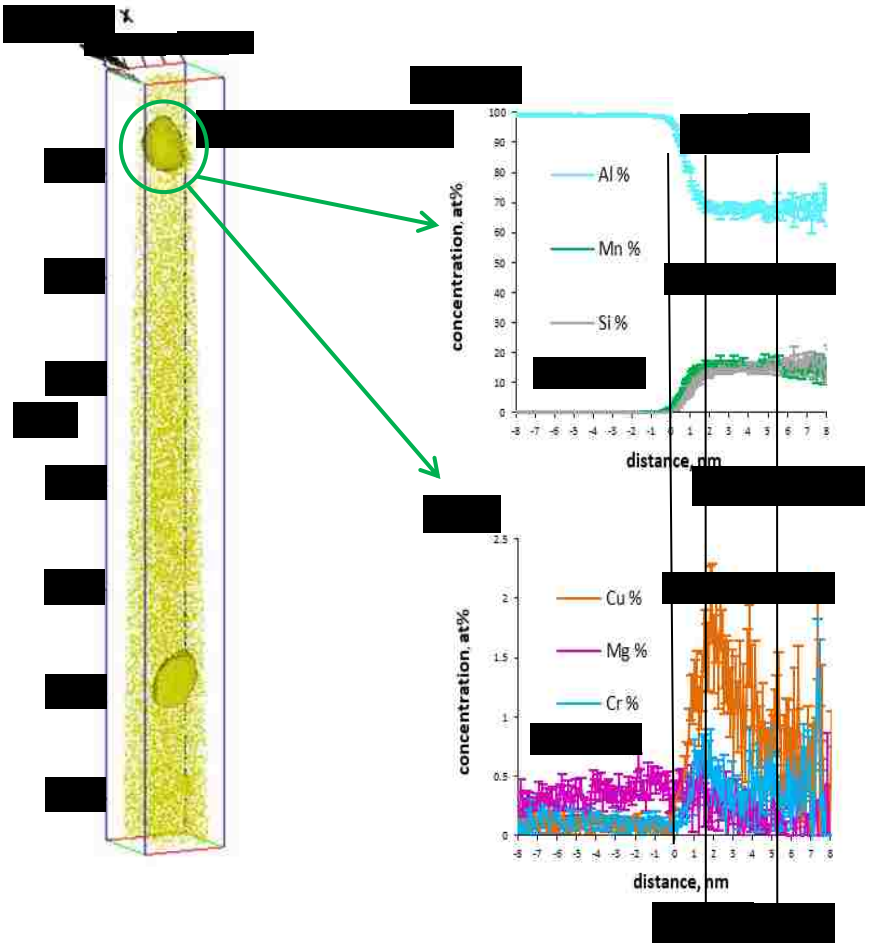

Figure 5.17 3-D reconstruction of the specimen after heating to 400 ˚C with a heating rate of 0.6 ˚C min^{-1} and quenching. (a) Mn isoconcentration surface delineates the α-dispersoids; (b) and (c) proximity histograms used to analyze the composition of the α-dispersoid.

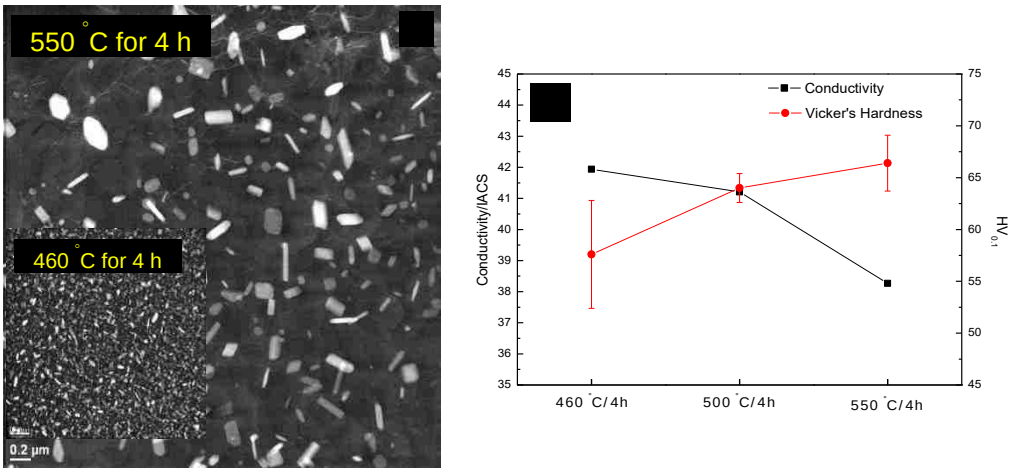

Figure 5.18 (a) STEM micrographs showing formation of dispersoids in the alloy after homogenization at 550 °C and 460 °C holding for 4 hours (0.6 °C min^{-1}); (b) Vickers hardness and electrical conductivity of the alloy annealed at different temperatures holding for 4 hours.

Chapter 6 Four-point bend fatigue properties of modified AA6061 (Al-Mg-Si-Cu) Al alloys with various Si contents

6.1 Introduction

Owing to the high strength, favorable formability, good corrosion resistance and lower costs, 6xxx series Al-Mg-Si(-Cu) alloys such as AA6061 are widely used in automotive industry to lighten the weights of automobiles and thus improve the fuel efficiency [1]. However, due to dynamic loading over the fatigue limit in service conditions and the presence of microstructural inhomogeneities such as porosities, inclusions, second phase particles, grain/phase boundaries and slip bands in engineering metallic materials, the fatigue properties of Al alloys are important in the design of engineering structures that use the alloys. Over 90% of the fatigue life of Al alloy components was reported to be consumed in the initiation and early growth of a dominant fatigue crack, and therefore, thorough and quantitative understanding of crack initiation behaviors is of paramount importance for enhancement of the fatigue properties of Al alloys [101-103].

The fatigue crack initiation behaviors in 6xxx series Al alloys has been studied by some researchers [210-213]. Gungor and Edward [210] investigated the effect of surface texture on the initiation of cracks in a forged T6 AA6082 Al alloy. It was found that cracks were initiated predominantly from slip bands on polished specimen surfaces, many of which were nucleated by subsurface coarse constituent particles (4 - 10 μm). Whereas for forged surface specimens, crack initiation mainly occurred at large particles (20 - 80 μm) with the help of surface roughness, including silica, titania or graphite, resulting from the contamination from the forging process. Zeng et al. [211] conducted fatigue tests on a 6061-T6 Al alloy with the addition of 0.53% excess Mg. The fatigue cracks were mainly initiated at the root of the small pits due to the severe stress concentration, which were generated in the electro-polishing after the dropping off of intermetallic particles on the specimen surface. Grain orientations around the defects also influenced the crack initiation by considering the angle between the maximum shear stress directions and the favorable slip planes at the defects root. The very-high-cycle fatigue (VHCF) behavior of a precipitation hardened Al-Mg-Si alloy was investigated by Takahashi et al. [212]. It was

suggested that the cracks in smooth specimen were formed within surface persistent slip bands (PSBs), which were found exclusively in {100} textured grains. Azzam et al. [213] studied the cyclic fatigue fracture behavior of light poles that were made of the 6063Al-Mg-Si alloy. It was observed that cracks were easily initiated at the recrystallized grain boundaries due to a mutually competitive interactions of GB Mg_2Si second phase and local stress concentration coupled with the tendency for the occurrence of slip and sliding between the neighboring grains. In addition, fatigue crack initiation could be modified by varying the aging condition [214-217]. For example, Edwards et al. [214] reported that the slip distribution and grain boundaries under different aging conditions could influence crack initiation in Al-Mg-Si alloys. A coarse slip distribution in the UA alloy aided crack nucleation, whereas coarse precipitates on the GBs were potent crack nucleation sites in the OA alloy. However, despite the studies were carried out, the fatigue crack initiation behaviors, especially crack initiation at pores, in 6xxx series Al alloys have not been extensively investigated.

In this chapter, four-point bend fatigue tests were carried out on two modified AA6061-T6 (Al-Mg-Si-Cu) Al alloys with different Si contents to study the effects of porosity on fatigue crack initiation behavior of the alloys. The S-N curves and number of fatigue cracks initiated at different stress levels were measured. The fatigue crack initiating pores were investigated using SEM. The results obtained demonstrated that the tunnel-shaped pores showed a major effect on the fatigue crack initiation behavior in the alloys.

6.2 Experimental details

The materials used in this work were two modified Mn and Cr-containing AA6061 (Al-Mg-Si-Cu) Al alloys with different Si contents. The nominal chemical compositions are shown in Table 6.1. The as-received condition was solution heat treated, water quenched and peak aged (T6). Its yield and ultimate tensile strengths were measured to be 345 MPa and 390 MPa for alloy A, and 400 MPa and 435 MPa for alloy B, respectively. In order to study the fatigue crack initiation behavior of the alloys, four-point bend fatigue tests were employed on an Instron-8802 servo-hydraulic materials testing machine. The dimensions of the specimens for the fatigue tests were chosen to be 36.5 mm x 10 mm x 4.6 mm, and

the testing geometry in the fatigue tests is illustrated in Figure 2.1. The loading and supporting spans were 6 and 30 mm, respectively, and the testing geometry was optimum for a uniform stress distribution on the sample surface with the sample thickness of 4.5 - 4.7 mm, providing the convenience of surface crack measurement and sample preparation, as the sample surface was flat, and the sample cross-section was uniform as well. Four-point bend fatigue tests were carried out at a stress ratio R of 0.1, a frequency of 20 Hz, with a sinusoidal waveform and at room temperature in laboratory air. The run-out point was set as 5500000 cycles in S-N curve measurements. Before fatigue tests the surfaces of the samples loaded in compression during the tests were ground using waterproof SiC abrasive papers gradually from grit 240 to 1200, followed by mechanical polishing using alumina powders of 1 μm, 0.3 μm and 0.05 μm in size, respectively, and finally silica colloidal suspension liquid. The fatigue machine was stopped automatically by setting up the top limit of sample deflection at about 0.4 mm. As a result, the sample surface still remained reasonably flat for examining fatigue crack initiation sites on an optical microscope and to avoid extra crack initiation on the surface due to the sudden release of energy at final failure. The maximum stress used in these tests ranged from 60 to 110% of the yield strength of the alloys. Two samples were tested at each stress level and the fatigue data were the average over the two samples. Optical microscopy (OM) was employed to count the number of initiated cracks on the surfaces of the fatigued samples. The crack initiation sites on sample and fracture surfaces were examined using HITACHI S-4300 and Zeiss EVO MA10 scanning electron microscopes.

6.3 Results and discussion

6.3.1 Microstructure and pore size distribution

As shown in Figures 6.1 and 6.2, pores were observed in the two modified AA6061-T6 Al alloys. After statistical quantification from optical micrographs taken randomly from well-polished specimens using software ImagePro, it was measured to be the average pore diameters of 3.2 and 2.64 μm, the average area fractions of the pores of 0.24% and 0.35%, and the average pore densities of 218 and 449 mm^{-2} for alloys A and B, respectively. Figure 6.3 shows the histogram plot of pore size distribution. It is evident in Figure 6.3 that the size of the pores found in these alloys was quite small that was mostly below 10 μm in

diameter. The size distributions of the pores responsible for fatigue crack initiation are presented in Figure 6.4. The mean valuse of initiation pore size were found to be 7.7 and 6.2 μm in alloys A and B, respectively. Evidently, the pores that were fatigue crack initiators were generally the larger ones among the porosity population which shows the presence of a low number density of large pores. Similar results were reported by other researchers [152]. It should be noted that the pore sizes were measured from the two-dimensional (2-D) metallographic samples, which were highly dependent upon where the random section was made, leading to the underestimation of the average sizes of the pores present in these alloys [218]. In addition, an experimental error in detecting the pores might be caused, because small amount of undissolved Mg_2Si particles, also shown in black color on optical micrographs, might be mistakenly counted as pores by the software [219]. As a result, the measured number of pores could be larger than the actual value. In order to obtain more reasonable results, methods to characterize the 3-D morphology of the pores for the measurement of the pore size should be developed in the future.

The SEM observation demonstrated that the majority of Mg_2Si and AlCuMgSi phases dissolved into the Al matrix, and α-Al(FeMnCr)Si phase became fragmented and spheroidized as illustrated in Figure 6.5. With the help of EDS in SEM, the chemical compositions of the second phase particles were analyzed, which showed the existence of fragmented α-Al(FeMnCr)Si phase and small amount of undissolved Mg_2Si phase in the alloys.

6.3.2 S-N curves and crack population

The maximum stress and logarithm of cycles to failure (S-N) curves of the two modified AA6061-T6 Al alloys were measured by four-point bend tests and plotted in Figure 6.6. In general, the fatigue life increased as the stress level decreased. The scatter in fatigue life was because all failures were observed to initiate at pores. The fatigue limits could then be determined to be approximately 243.6 MPa and 280.6 MPa for alloys A and B, respectively. It can be seen that alloy B had a fatigue limit higher than that of alloy A, which was consistent with their tensile properties that the yield and ultimate strengths (435 MPa and 400 MPa) of alloy B were higher than those (345 MPa and 390 MPa) of alloy A. No cracks

were observed on the specimens' surfaces which fatigued bellow the fatigue limit, and cracks were often found after the fatigue tests at a stress level over the fatigue limit, as shown in Figure 6.7, which were initiated predominantly from pores in surface. Porosity in the alloys could influence the fatigue limits of the alloys, which might have different effects on different stages of the fatigue process. The effects of pores on the crack initiation behaviors in the two alloys will be described in the following sections.

Figure 6.8 shows the number of cracks generated on the surfaces of the fatigued samples at failure with regard to the applied maximum cyclic stress in the two alloys. The number of cracks found on surface was very small (1~3) and barely increased with the applied stress when the applied stress was below the yield strength. However, it was increased sharply with the increase of the applied stress to approximately the ultimate tensile strength. In addition, alloy A (low Si content) had much less weak-links at UTS than alloy B (high Si content), indicating that partial melting (i.e., overheating) of Si-containing phase led to the formation of micro-pores, as described in the following section. Although pores were the predominant crack initiation sites, only a very small percentage of them was found to lead to crack formation. It is therefore significant to understand the factors that determine crack initiation from pores in the alloys.

6.3.3 Crack initiation characteristics

Figures 6.7 and 6.9 represent the fatigue crack initiation sites in the fatigue samples of the two alloys, obtained by scanning electron microscope. As shown in Figure 6.7, several small cracks were observed on the surface of the fatigued sample after four-point-bend test. These cracks were mainly initiated at pores (Figure 6.9), which might be formed during solidification or due to melting of the Si-containing particles during homogenization. Porosity could be formed during solidification, which may originate from hydrogen gas evolution, microshrinkage, or a combination of both [1,151]. Shrinkage pores results from insufficient metal flow into the space between connected dendrites during the solidification process, while gas pores (mainly hydrogen) attribute to the decrease in gas solubility in solid metal compared to the liquid during solidification. The shrinkage pores have very irregular three-dimensional shapes and varied sizes, whereas the gas pores are usually

roughly spherical (circular in cross-section). Shrinkage pores are observed as groups of pores surrounded by primary dendrites and eutectic phase, and gas pores are found as isolated entities. However, the distinction of shrinkage vs. gas pores in a given casting sample is not always straightforward and difficult to make. An example of typical shrinkage and gas pores in the alloys studied in as-cast state is shown in Figure 6.10. Other pores formed during casting are illustrated in Figure 6.11. Melting of the Si-containing particles (i.e., overheating) could also cause porosity in the alloys during high temperature annealing that had a negative impact on the mechanical properties of the alloys [220]. It is interesting to note the sharp increase in porosity after homogenization at 560 $^{\circ}$C for 4 hours, as shown in Figure 6.12, indicating the formation of micro-pores was very likely due to the overheating. The melting at the temperature of 560 $^{\circ}$C was most likely caused by the following reaction [221]: Al + Si + Mg_2Si → Liquid, as illustrated in Figure 6.13. This can explain the higher density of pores in alloy B than in alloy A, since alloy B had more Si content to form Si-containing particles during casting. Figures 6.9(k,l) illustrate the existence of other minor crack initiation sites. Small cracks could also initiate from an Mg_2Si particle (Figure 6.9(k)) or the interface between Mg_2Si particle and Al matrix (Figure 6.8(l)), indicating that the particle or interface was weak and prone to be cracked or debonded during the fatigue cycling. In addition, all the cracks observed did not grow simultaneously. Only a minority of cracks could grow into long cracks.

6.3.4 Fractography

The fatigue fracture surfaces of the two T6 Al alloys were examined using scanning electron microscopy to identify the crack initiation sites. Figure 6.14 shows a global view of the broken specimen in the condition of high stress (110% σ_y) with evidence of multiple initiation sites at different pores with the details presented in Figure 6.15. Other critical pores where fatigue cracks were initiated in different conditions are illustrated in Figure 6.16. It was observed that the pores responsible for fatigue crack nucleation were generally located at or very close to the specimen surface due to the high stress concentration introduced at these pores which were almost always aspheric in shape with the larger dimension in depth from the sample surface. These pores gave rise to an inhomogeneous distribution of stresses and strains at the micro-scale, and the local micro-stresses were

higher than the average and might exceed the local yield stress in specific regions around the pores. The magnitude of this micro-plastic deformation was dependent on both the far-field stress level and the nature of the pores. Under cyclic loading, with increasing number of cycles the micro-plastic deformation could be accumulated to a critical local value which was large enough to initiate fatigue cracks. As described by Zhang et al. [110], the pore size distribution could not be directly used to evaluate the fatigue crack initiation behaviors in the alloy, meaning that cracks could be nucleated from smaller pores instead of larger ones on the surface. In addition, crack nucleation might not even be associated with the pores on the surface, and it could be caused by the pores in the subsurface. Analogous to coarse second phase particles in high strength wrought Al alloys [222], many factors such as the size, shape, orientation, surface distance as well as nearest-neighbor distance of pores have a synthetic influence on the initiation of fatigue cracks in the Al alloys, which indicates the strong 3-D character of the damage mechanism. Further work thus needs to be done to understand the factors that determine crack initiation from pores in the alloys.

6.4 Conclusions

(1) The micro-pores were observed and statistically characterized in the two modified AA6061-T6 Al alloys with various Si contents. The average diameters of the pores on the surface were 3.2 and 2.64 μm, the average area fractions of the pores were 0.24% and 0.35%, and the average pore densities were 218 and 449 mm^{-2} for the alloys with low and high Si content, respectively. These pores were formed during solidification or due to overheating that partially melted the Si-containing particles at GBs in the alloys during homogenization.

(2) The fatigue limits were measured to be approximately 224 and 283.5 MPa for the alloys with low and high Si content, respectively, at a run-out number of 5.5×10^6 cycles in four-point bend fatigue tests.

(3) The number of cracks observed on surface was found to be very small (1~3) and barely increased with the applied stress when the applied stress was below the yield

strength. However, it was increased sharply with the increase of the applied stress to approximately the ultimate tensile strength.

(4) The fatigue crack initiation behaviors of the alloys were dramatically influenced by the tunnel-shaped pores in the alloys. Fatigue cracks were predominantly initiated at the pores at or very close to surface, which were always aspheric in shape with the larger dimension in depth from the sample surface, with the minority of the cracks being initiated at the second phase Mg_2Si particles or at the interface between the Mg_2Si particles and the matrix.

Table 6.1 The chemical compositions of Al-Mg-Si-Cu alloys studied in the present work (in wt%)

Alloy	Mg	Si	Cu	Mn	Cr	Fe
A	0.81	0.80	0.43	0.64	0.26	0.15
B	0.85	1.24	0.43	0.63	0.26	0.15

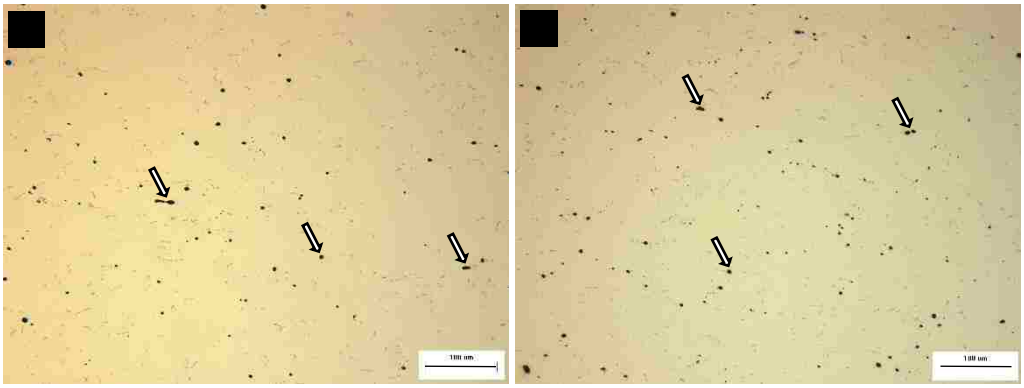

Figure 6.1 Pores in the two modified AA6061-T6 Al alloys. (a) Alloy A and (b) alloy B.

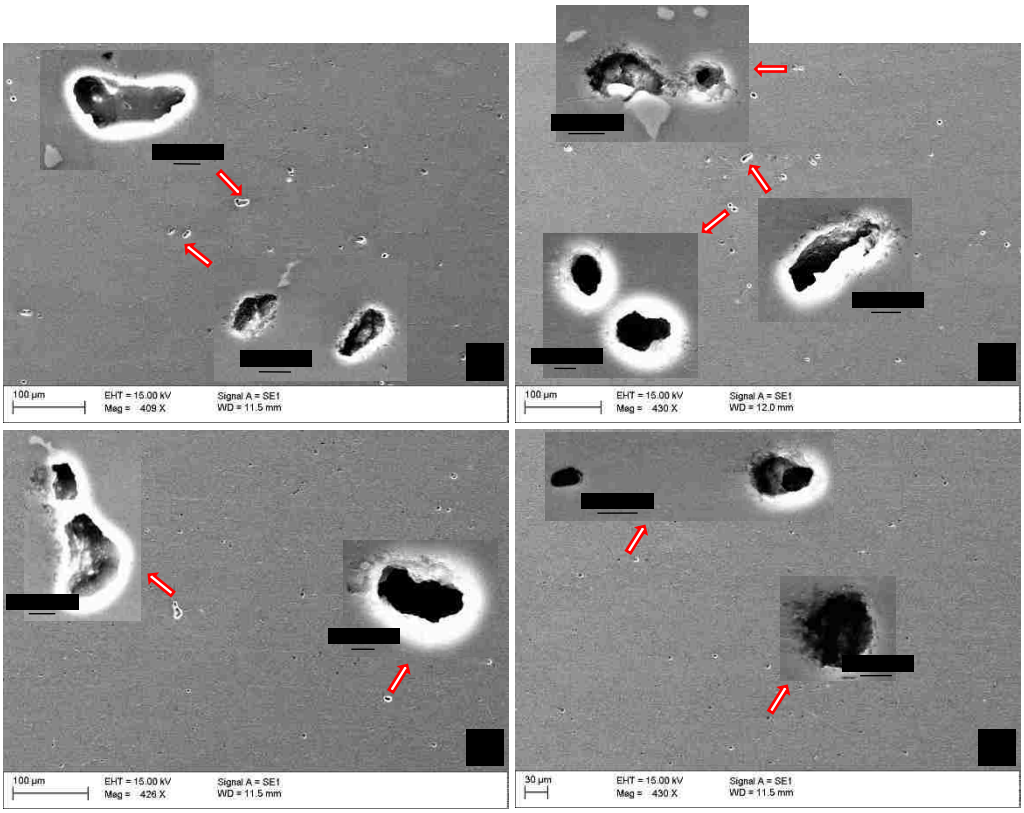

Figure 6.2 SEM micrographs showing pores in (a) and (b) alloy A and (c) and (d) alloy B in T6 state.

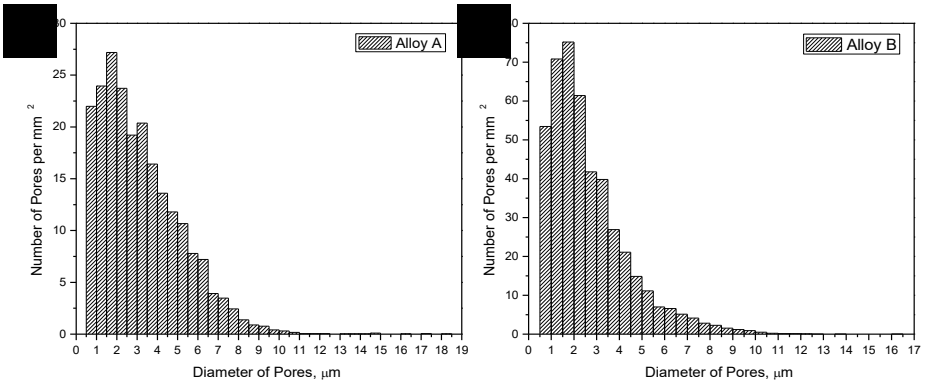

Figure 6.3 Histogram plot of pore size distribution in (a) alloy A and (b) alloy B in T6 state.

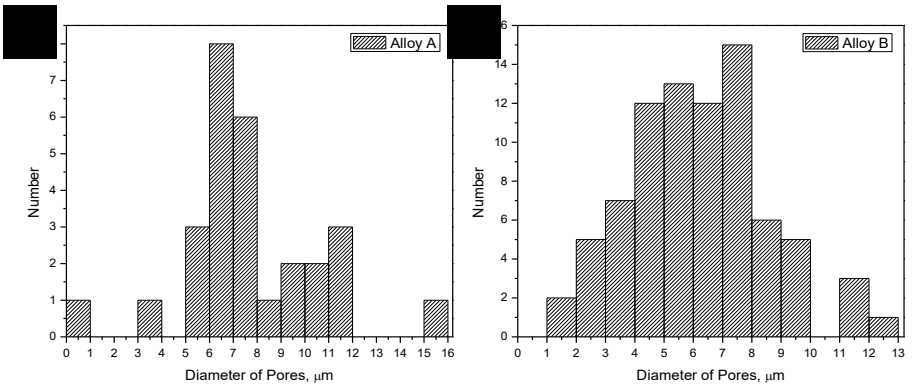

Figure 6.4 Histogram plot of measured crack initiation pore size distribution in (a) alloy A and (b) alloy B in T6 state.

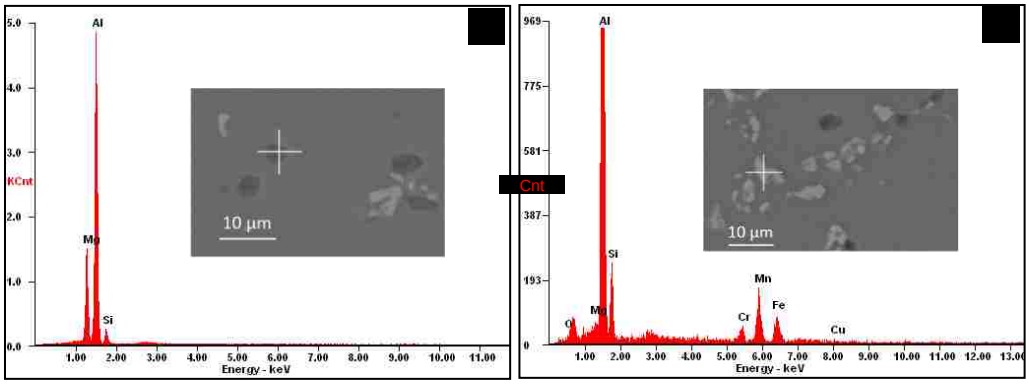

Figure 6.5 EDS spectra of the particles in the modified AA6061-T6 Al alloys.

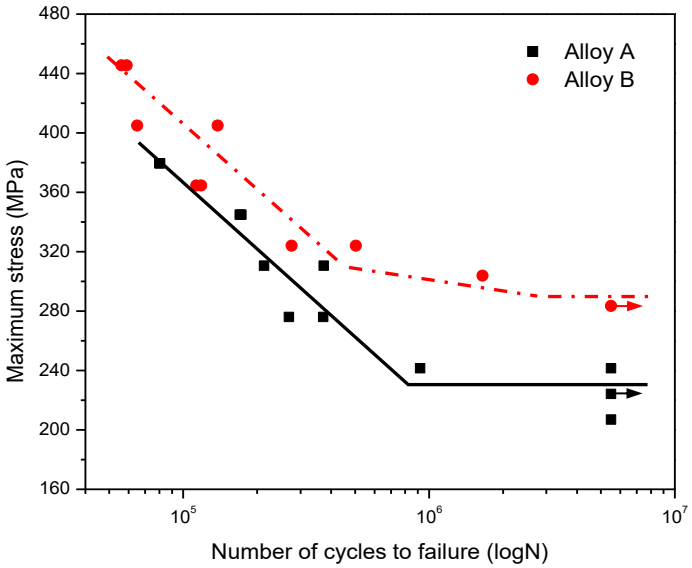

Figure 6.6 S-N curves of the two modified AA6061-T6 Al alloys.

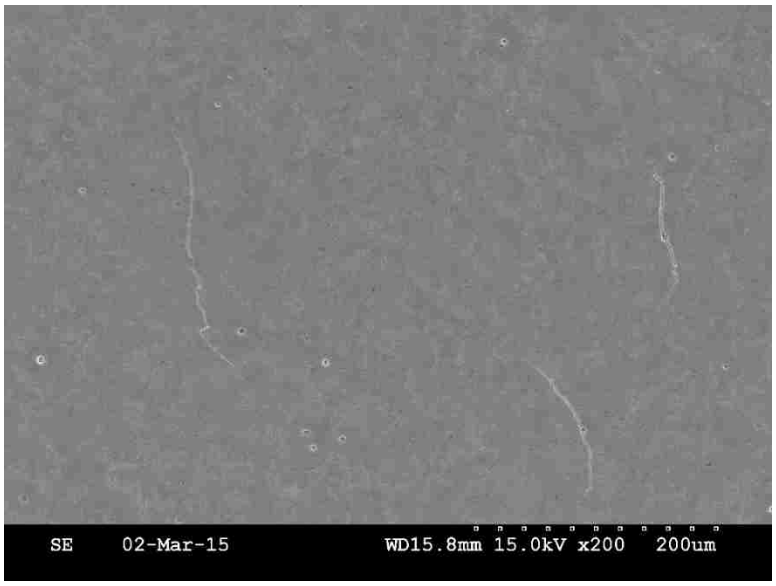

Figure 6.7 Surface cracks initiated from pores at stress level of 110% σ_y in alloy B.

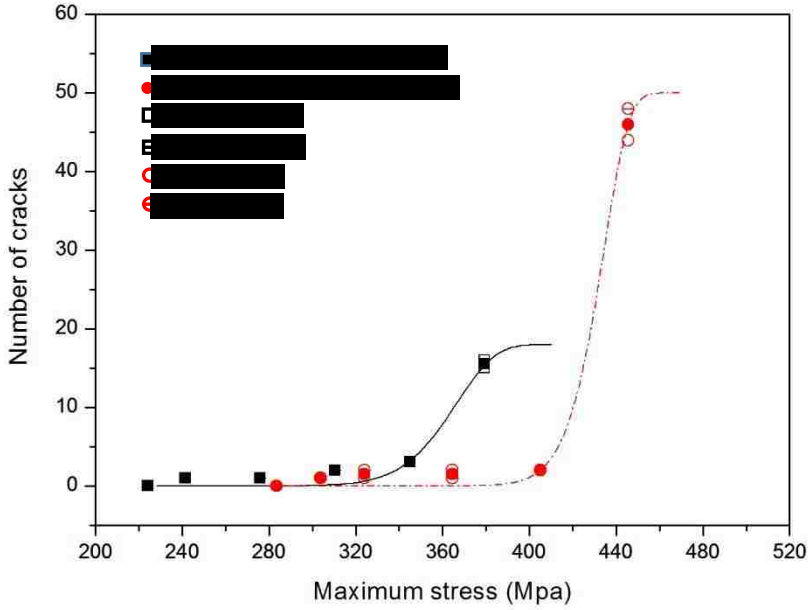

Figure 6.8 Crack numbers at different maximum stresses in the two modified AA6061-T6 Al alloys.

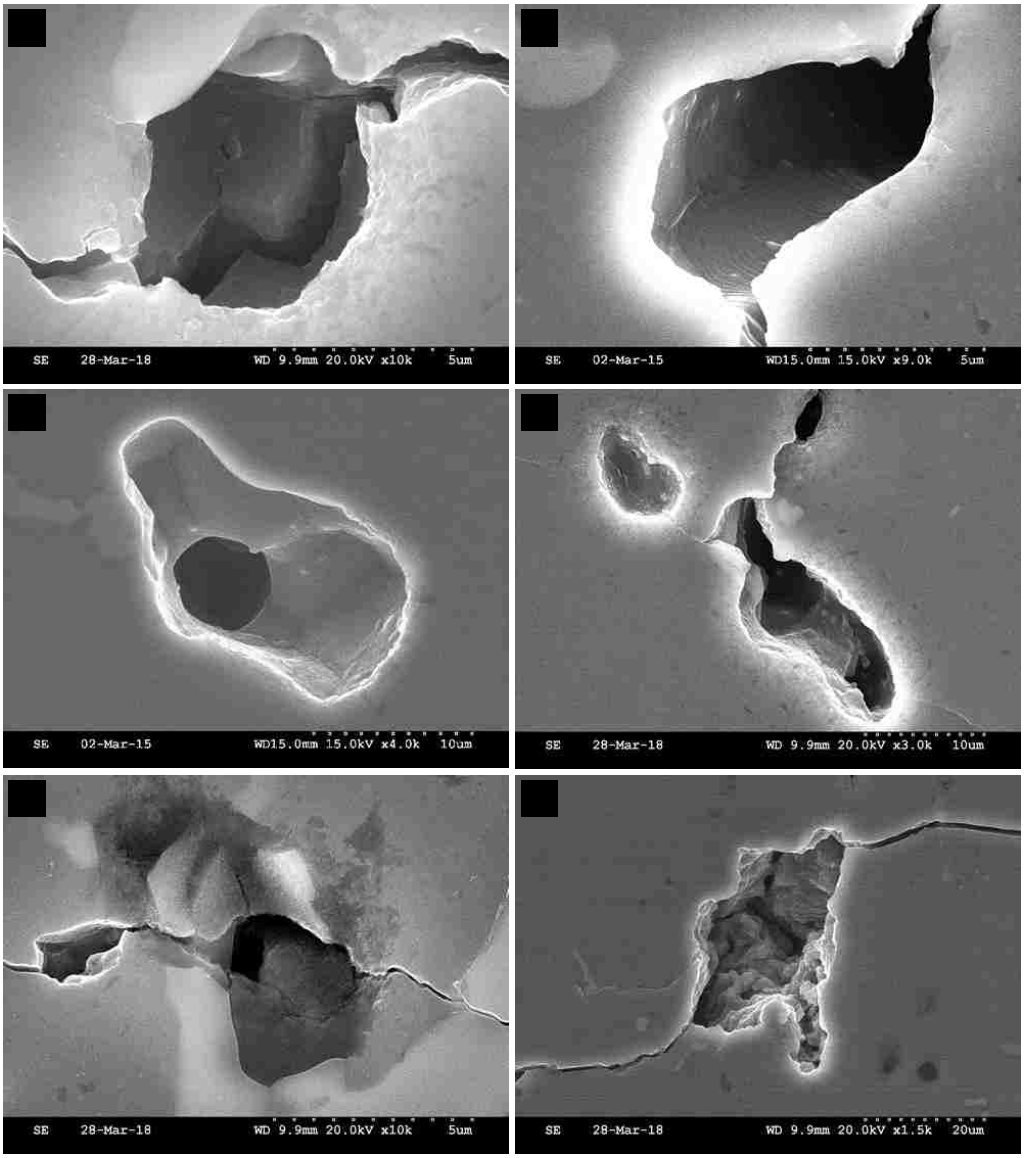
SE 28-Mar-18 WD 9.9mm 20.0kV x10k 5um
SE 02-Mar-15 WD15.0mm 15.0kV x9.0k 5um
SE 02-Mar-15 WD15.0mm 15.0kV x4.0k 10um
SE 28-Mar-18 WD 9.9mm 20.0kV x3.0k 10um
SE 28-Mar-18 WD 9.9mm 20.0kV x10k 5um
SE 28-Mar-18 WD 9.9mm 20.0kV x1.5k 20um

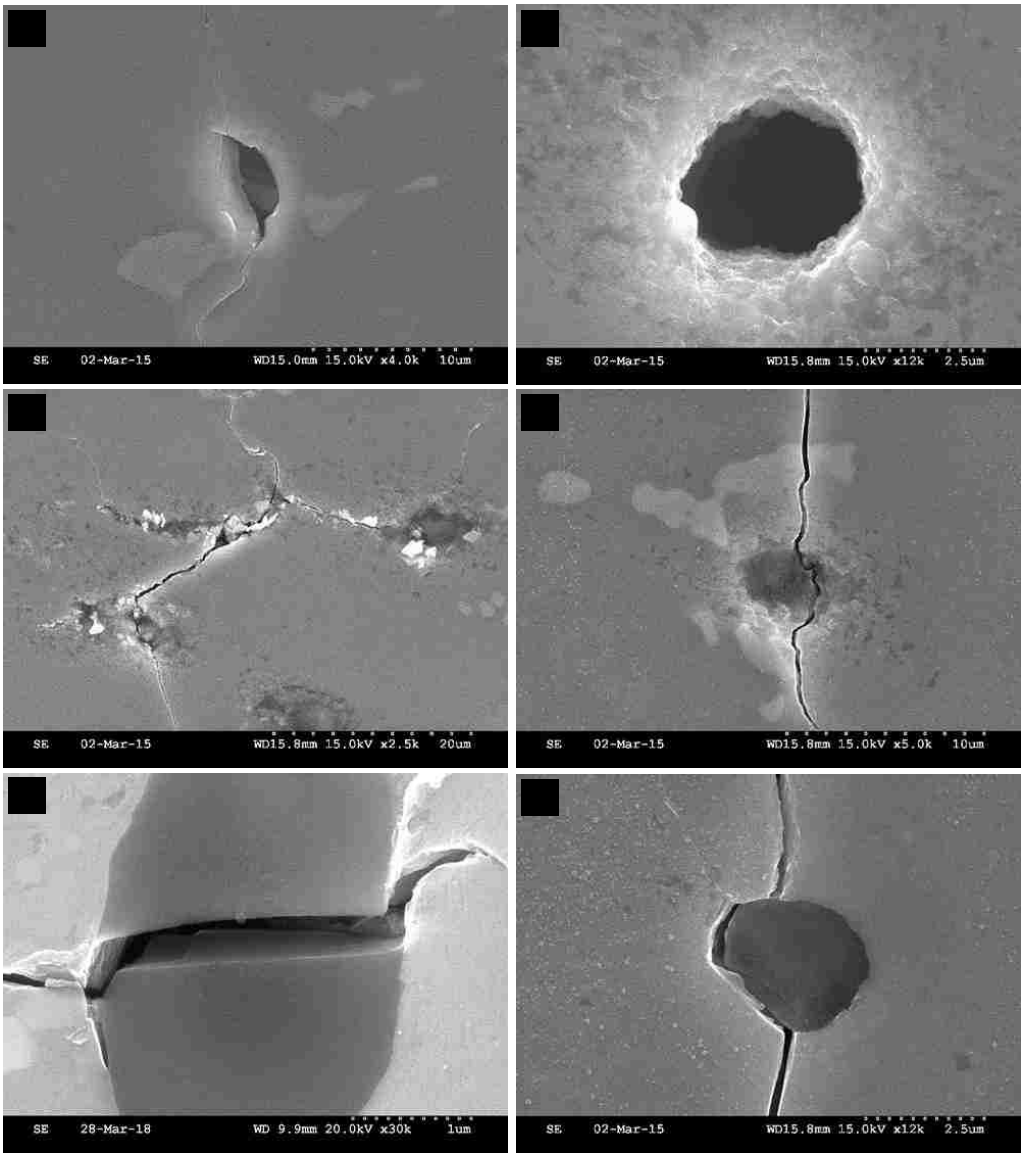

Figure 6.9 SEM micrographs showing fatigue crack initiation sites. (a)-(j) Cracks initiated at pores; (k) a crack initiated at a Mg_2Si particle; (l) a crack initiated at the Mg_2Si particle/matrix interface.

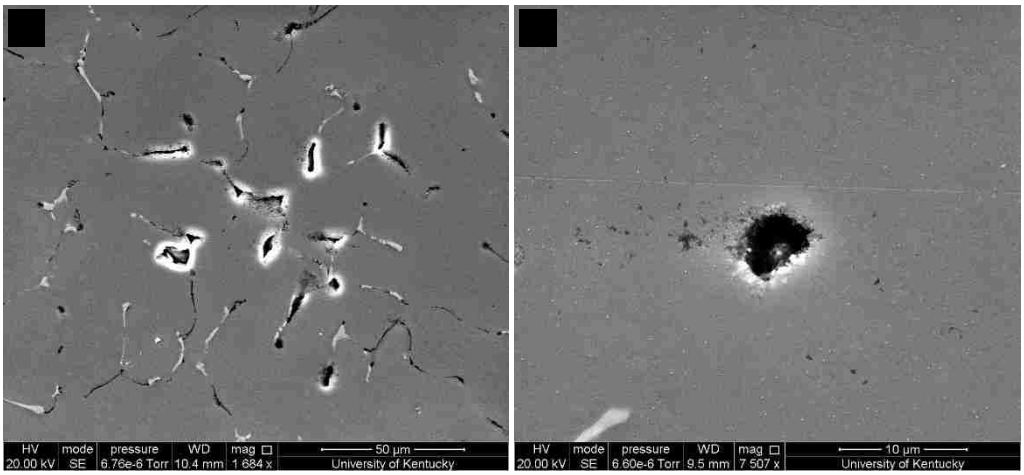

Figure 6.10 (a) Shrinkage pore and (b) gas pore in as-cast state of the alloys.

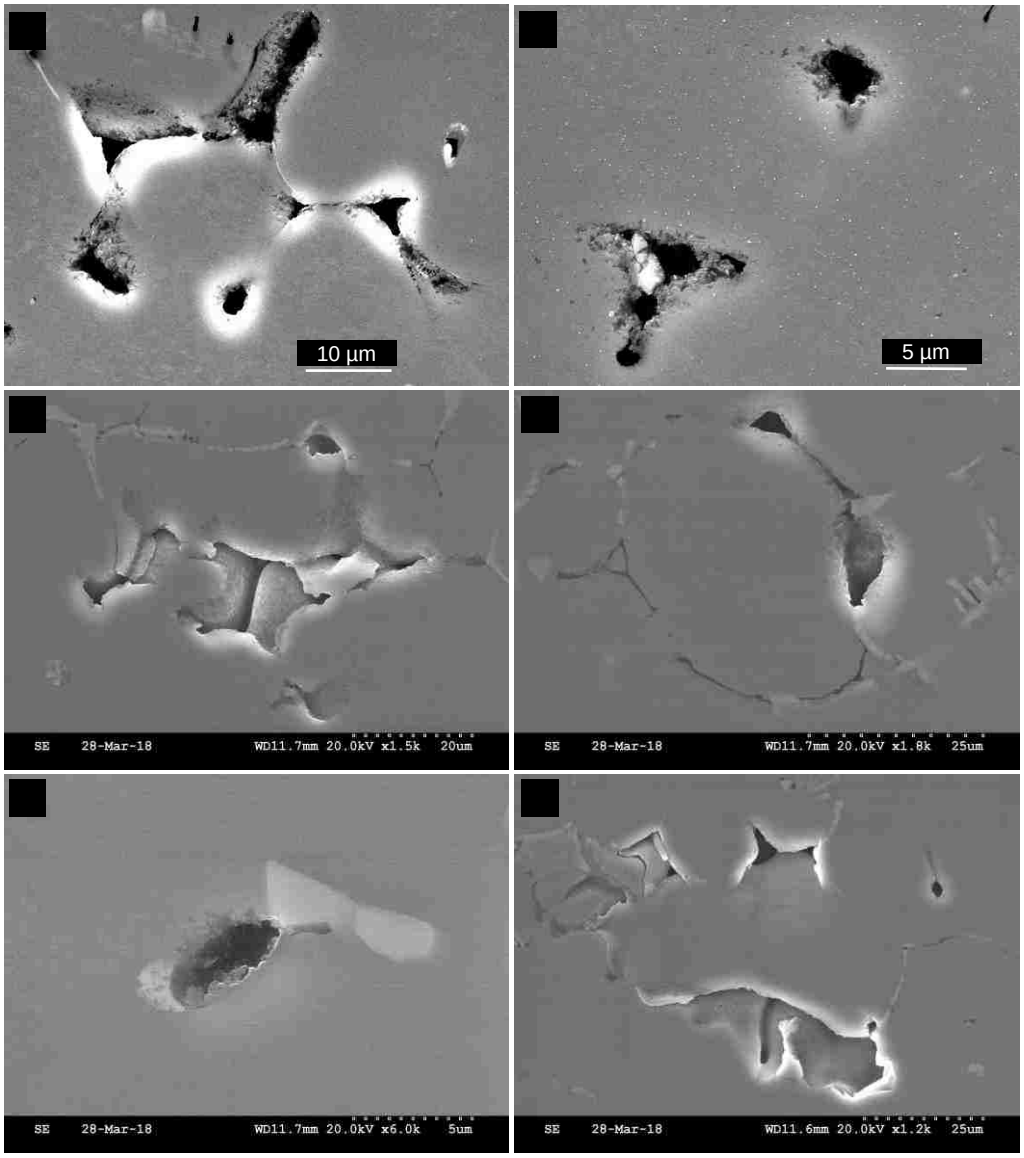

Figure 6.11 Pores in as-cast state of the alloys.

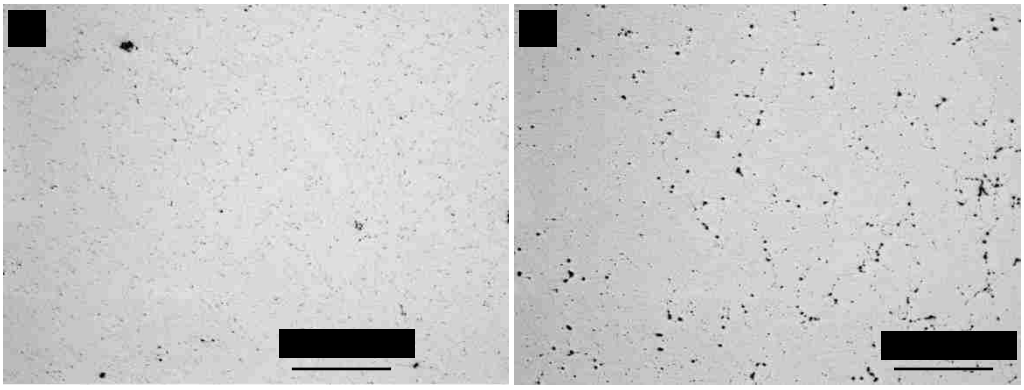

Figure 6.12 Porosity in alloy B (a) in as-cast state and (b) after homogenization.

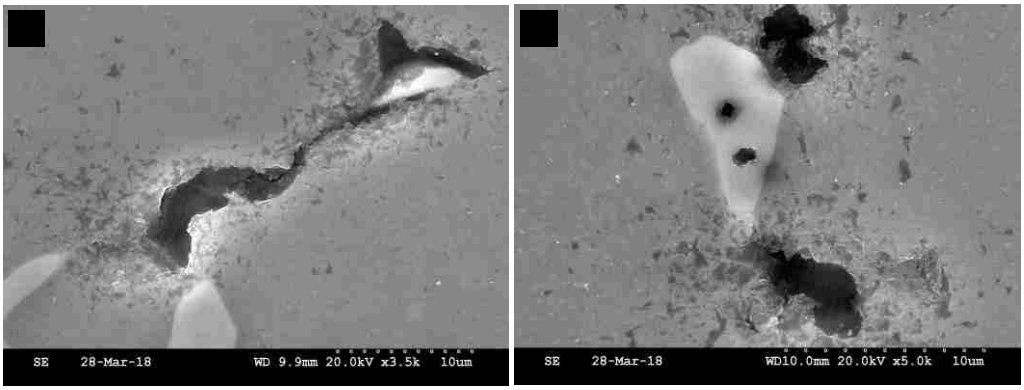

Figure 6.13 Melting of the Si-containing particles after homogenization at 560 °C for 4 hours.

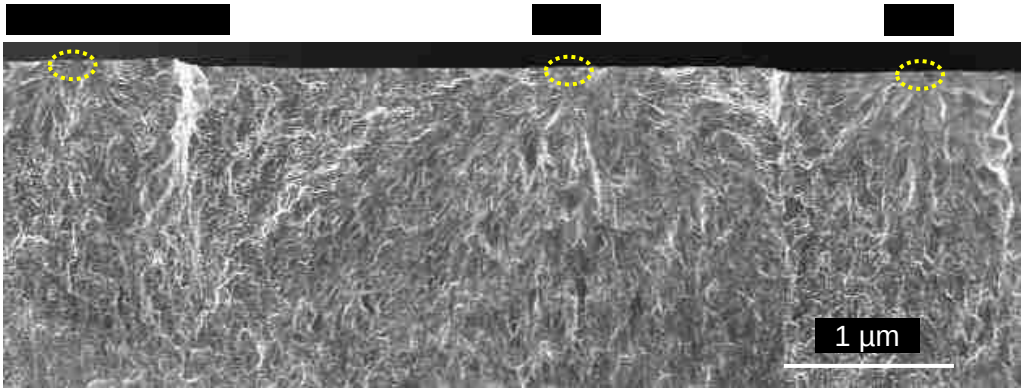

Figure 6.14 SEM observation of a fracture surface showing the coalescence of fatigue cracks initiated at different pores in alloy A in high stress (110% σ_y) condition.

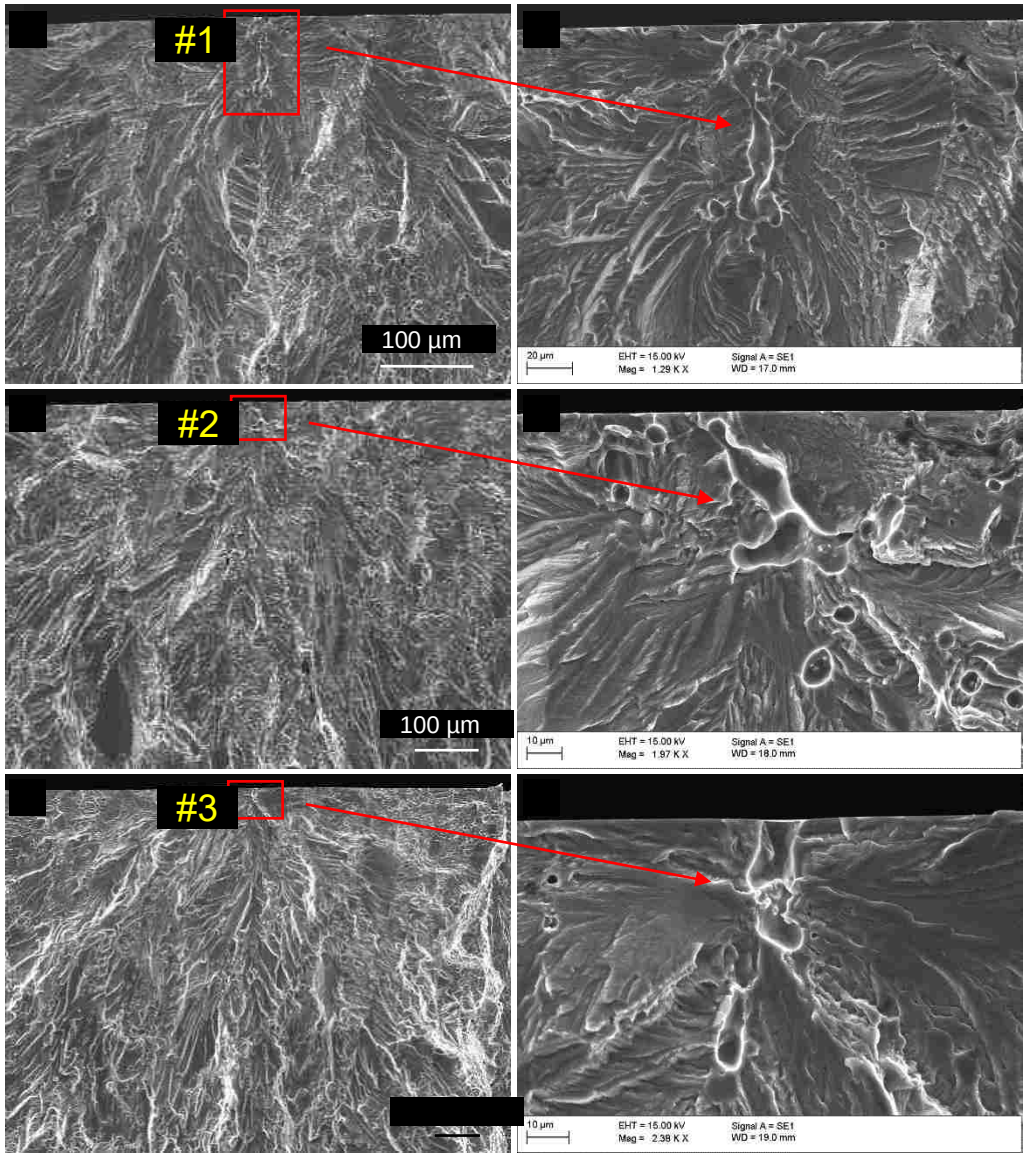

Figure 6.15 SEM observation of fracture surfaces showing the details of the fatigue crack initiation pores in Figure 6.13.

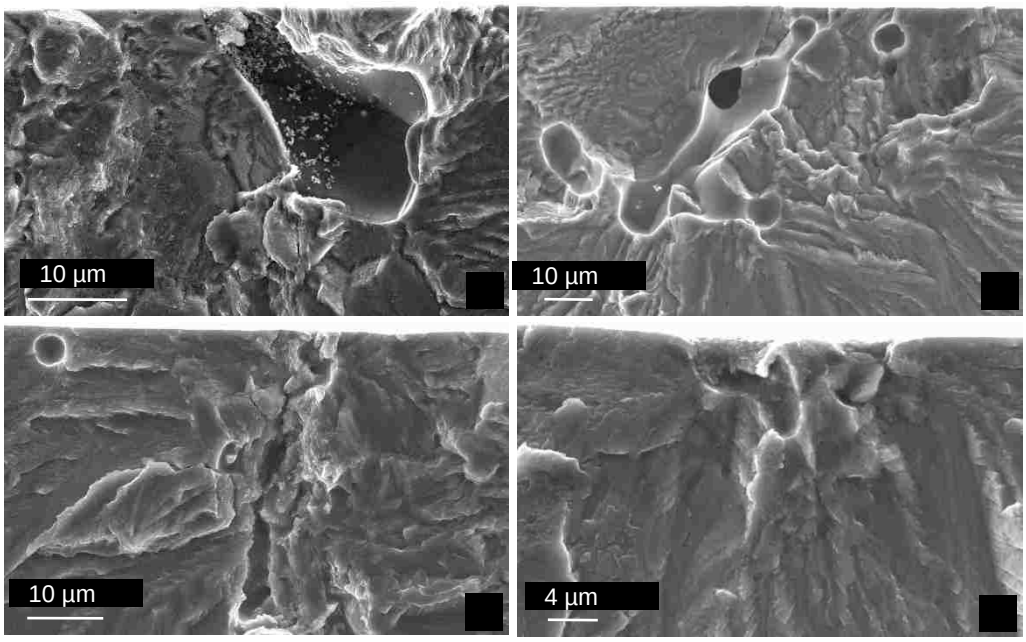

Figure 6.16 SEM observation of fracture surfaces showing the details of the fatigue crack initiation pores in (a) alloy A in low stress (80% σ_y) condition; (b) alloy A in high stress (110% σ_y); (c) and (d) alloy B in high stress (110% σ_y) condition.

Chapter 7 Numerical modeling for fatigue crack initiation in a modified AA6061 (Al-Mg-Si-Cu) Al alloy

7.1 Introduction

As described in the first chapter, finite element analysis (FEA) method was used in various cast Al alloys to study the effects of porosity (pore size, pore position, pore shape and clustering) on fatigue crack initiation behaviors [155,157,161,165,167-171]. However, the quantitative analysis of the correlation of microstructure (pores) with the fatigue crack initiation behaviors in 6xxx series Al alloys is still scare and far from satisfaction. In this chapter, the relationship of the fatigue crack incubation life with the pore position was analyzed by a 3-D finite element analysis in a modified AA6061 Al alloy. The pores were assumed to be 7 μm in diameter for simplicity in the model. A 3-D pore-sensitive model was consequently developed to quantitatively identify the effects of pores on the fatigue crack initiation behavior in the alloy. The details of the FEA and Matlab simulations were introduced.

7.2 Details of numerical modeling

7.2.1 FEA modeling for crack initiation from pores

The stress and strain fields around a micro-pore were quantified as a function of pore position in depth from the surface using a three-dimensional (3-D) finite element model under different stress levels in a modified AA6061 Al alloy (alloy B in Table 6.1), which was developed by the commercial finite element analysis (FEA) software ABAQUS 6.11. In the FEA model, the alloy was assumed to be an elasto-plastic isotropic solid with a Young's modulus of 65 GPa and Poisson ratio of 0.3. Experimentally determined value of yield stress of 400 MPa was used for the alloy. The engineering stress-strain relationship was measured from tensile tests at room temperature, as shown in Figure 7.1(a). Based on the experimentally measured tensile stress-strain curve, the constitutive behavior of the material could be simulated by the cyclic stress-strain curve which was modeled with a nonlinear isotropic hardening law.

The pores used in the model were spherical in shape, for simplicity, with the same size of 7 μm in diameter to avoid the time-consuming simulation of pores with irregular shape. This size of the pores was assumed since the average size of the crack initiation pores was around 7 μm in diameter based on the pore size distribution measurement shown in Figure 6.3. As shown in Figure 7.2(a), the alloy was in a shape of a cube of 70 μm^3, and a spherical micro-pore, 7 μm in diameter, was located in the middle of the alloy. Because of the symmetry of the structure, only a quarter of the pore in a quarter of the alloy was used in FEA simulation to minimize the calculation time. The maximum cyclic stresses of 80%, 100% and 110% of the yield stress were applied along the X axis of the cube as a sinusoidal wave with an R ratio ($R = \sigma_{min}/\sigma_{max}$) of 0.1, respectively (Figure 7.1(b)). In the FEA modeling, the global mesh was used for the whole material and the region surrounding the pores was modelled with a refined mesh to increase the accuracy of the calculation of stress and strain fields around the pores. The position of a pore in the matrix is illustrated in Figure 7.2(b). The distance between the pore origin and the free surface was defined as D, and the pore radius was r. The D/r ratio was used to represent the pore location in Z direction. When the pore center was inside the surface, D was negative; otherwise, it was positive. With D/r = 1, 0, and -1, the pore was located just below the surface, half inside the alloy and totally out of the surface, respectively. In the present work, the pore locations were assumed to be in the range of 0 to 2 in D/r, since the effect of pore position on the stress concentration around the pore was relatively small when D/r < 0 or D/r > 2 [62,167].

The local stress/strain distributions around pores were calculated and the results were presented in terms of normalized maximum principal stress ($\sigma_{max}/\sigma_{nss}$) and strain ($\varepsilon_{max}/\varepsilon_{nss}$) where the superscripts '*nss*' represent the nominal far-field values. The stress and strain concentration factors due to a pore were denoted by $K_{t,\sigma} = \sigma_{max}/\sigma_{nss}$ and $K_{t,\varepsilon} = \varepsilon_{max}/\varepsilon_{nss}$ respectively. In the range of elastic deformation, $K_{t,\sigma}$ and $K_{t,\varepsilon}$ had the same value. Whereas $K_{t,\varepsilon}$ was greater than $K_{t,\sigma}$ if the local plastic deformation occurred around the pores. In the present model, the effective plastic concentration factor, K_t, defined as the geometric mean value of $K_{t,\sigma}$ and $K_{t,\varepsilon}$ ($K_t = \sqrt{K_{t,\sigma}K_{t,\varepsilon}}$), was used to represent the stress/strain concentration around the pores, since yielding could occur due to sufficiently high local stress. The stress and strain were analyzed after 30 cycles because of their corresponding stable values.

7.2.2 Prediction of crack incubation life

The application of the Manson-Coffin law is a traditionally useful method to predict the fatigue life of a material under a strain-controlled fatigue experiment, which relates the number of strain reversals to fatigue failure to the applied plastic strain amplitude. It was found that the fatigue crack initiation can be evaluated by the plastic strain accumulated around the crack nucleation site. Nowadays, a modified Coffin-Manson equation was developed to calculate the fatigue crack incubation life when the cross-section of the material is scaled down to a microscopic range, which is expressed as [168]

$$CN_{inc}^{\alpha} = \frac{\Delta\gamma_{max}^{p*}}{2} \tag{7.1}$$

where N_{inc} is the incubation life of a fatigue crack at a micro-pore, $\Delta\gamma_{max}^{p*}$ is the local maximum cyclic plastic shear strain range around a micro-pore, and C and α are materials constants which were determined from experimental S-N data. For an AA6061-T6 Al alloy, α = -0.95, and C = 0.3 [223], which was used in the current modelling.

For example, the crack incubation life at a surface pore could be estimated by the modified Coffin-Manson equation in cast Al alloys [155,168], in which finite element model was employed to calculate the local maximum cyclic plastic shear strain range $\Delta\gamma_{max}^{p*}$. In this work, the incubation life of a fatigue crack nucleated at a surface pore was estimated using the modified microscopic-scale Coffin-Manson equation. 3-D FEA was applied to calculate $\Delta\gamma_{max}^{p*}$ by averaging the plastic shear strain range over a cross-section that was equivalent to the micro-crack plane, the procedure of which is illustrated in Figure 7.3. The contours of the simulated maximum plastic shear strain γ_{max}^{p} around a surface pore is illustrated in Figure 7.3(a), in which the "+" and "-" signs represent clockwise and anti-clockwise directions of the shear strain, respectively. Figure 7.3(b) shows the region to average $\Delta\gamma_{max}^{p*}$ that was the area LMN on the critical plane close to 45 degree with the loading direction, which was selected by the maximum absolute value of the shear strain in dark blue color. The intercept line (MN) between the free surface and the critical plane was set to be 1.5 μm [167], and the tangent line (NL) with the pore was then determined. The area LMN varied with pore positions and the applied cyclic stresses. Based on the contour of γ_{max}^{p} on the critical plane, γ_{max}^{p} in region LMN could be determined, and

$\Delta\gamma_{max}^{p*}$was thus calculated by averaging γ_{max}^{p} range over the area LMN. Figure 7.4 shows the simulated maximum cyclic plastic shear strain γ_{max}^{p} in the region surrounding a micro-pore after 50 cycles, which was generally stabilized after 20 cycles. In the present study, the values between 25 and 30 cycles were used for the calculation of the local maximum cyclic plastic shear strain range $\Delta\gamma_{max}^{p*}$.

7.2.3 3-D pore-sensitive model for crack initiation

A quantitative model, which took into account the 3-D effects of pores on the local stress/strain fields in surface, was applied to quantification of the fatigue crack population. In order to construct a 3-D digital pore structure, the stereology theory was applied to determine the 3-D volume fraction of the pores from the 2-D area fraction of the pores measured experimentally in the alloy, which shows that the volume fraction of a second phase (pores) in a 3-D specimen equals the area fraction of the second phase (pores) on the randomly selected surface of the specimen. The basic process to quantify fatigue crack initiation behavior in the modeling is summarized as follows [167].

(1) The area fraction of porosities was experimentally measured from more than 100 optical micrographs randomly taken from 12 well-polished specimens at magnification of 200x;
(2) The area number density of pores was converted into volume number density using the stereology principle that the pores volume fraction ≈ measured area fraction of pores;
(3) A 3-D digital pore structure was constructed by random distribution of spherical pores in a cube of 1,000×1,000×1,000 μm^3, as shown in Figure 7.5(a) [167];
(4) The free surfaces were randomly selected by more than 1000 times cross-sectioning through the digital pore structure, as illustrated in Figure 7.5(b) [167];
(5) The position of each pore and area fraction of pores on each surface and around the surface within [0, 2] of D/r were collected;
(6) The averaging area fraction of surfaces from simulations and the experimental area fraction was compared to verify the model stability;
(7) Crack population from surface pores was quantified;
(8) The simulated results and experimental results were compared for validation of the model.

Only single-sized pores of 7 μm in diameter was employed in the 3-D digital pore structure to avoid the overwhelming computing time required for the calculation of crack incubation life at each pore with different sizes. The total area fraction of pores was measured from more than 100 optical micrographs that were randomly taken from well-polished specimens at magnification of 200x, which was 0.352% in the alloy studied. The corresponding number of pores in the 10^9 μm^3 cube was thus calculated to be 16932, namely, the volume number density was 16.932 x 10^{-6} μm^{-3} through the conversion using stereology theory. These pores were randomly distributed into the cube under the condition that two pores were more than one radius apart between the edges of the pores to avoid pore clustering effect. The pore area fraction was determined by averaging the simulated value on each randomly selected cross-section through the cube over the number of sampling (i.e., sample size). As shown in Figure 7.5(c), the difference between the experimental and simulated pore area fractions on surface was only 0.1% when the sampling size was greater than 1000, meaning that the simulated pore structure was consistent with the experimental measurement in terms of the total pore area fraction. In other words, in order to provide a consistent pore structure with an area fraction of 0.352% on the randomly selected cross-sections, the volume of the digital pore structure constructed in a single sampling should be equal to or more than 1×10^{12} μm^3.

7.3 Results and discussion

7.3.1 The stress and strain distributions around a surface pore

The distribution of the Von Mises stress (σ_{mises}) and the maximum plastic shear strain (γ^p_{max}) around a spherical pore in the free surface at the maximum applied cyclic stress of 80% σ_y and D/r = 0 is shown in Figure 7.6. The red color represents the maximum stress contour around the pore, which occurred on the plane normal to the loading direction. Whereas the maximum plastic shear strain contour around the pore appeared as the blue color that was near the sample surface and on the plane through the pore origin and close to 45 degree with the loading direction. The local maximum Mises stress was calculated to be 338.8 MPa that was lower than the yield strength because of the low applied stress and the pore location that was not close enough to the surface, meaning that plastic deformation could not occur around the pore under this condition, although stress concentration existed.

7.3.2 Effect of pore position on stress/strain concentration

The relationship between pore position and stress/strain concentration at various applied cyclic stresses for the pore with 7 μm in diameter was analyzed. Figure 7.7 plots the effective plastic concentration factor (K_t) around a pore with regard to the pore depth from the sample surface at the stress levels of 80% σ_y, 100% σ_y and 110% σ_y, respectively. The K_t plots appeared to be approximately axial symmetrical on both sides of the pore position of D/r = 1, showing the highest values at D/r = 1, i.e., when the pore was just buried beneath the free surface. The peak value of K_t was >= 10, from which the values dropped quickly and was subsided to almost a constant value of 1.2 when D/r > 2 or D/r < 0.

7.3.3 Effect of pore position on driving force and incubation life

The maximum shear strain range ($\Delta\gamma_{max}^{p*}$) was considered to be the driving force for fatigue crack formation at a pore, which is plotted against the pore position in depth from the surface at the applied maximum cyclic stresses of 80% σ_y, 100% σ_y and 110% σ_y, respectively, as shown in Figure 7.8. The $\Delta\gamma_{max}^{p*}$ curves showed extreme values at D/r = 1 which was increased with increased applied stress, and the values of $\Delta\gamma_{max}^{p*}$ decreased very sharply to almost zero when the pore was away from the position of D/r = 1, meaning the existence of very narrow range of D/r in which fatigue crack initiation at pores might occur.

The fatigue crack incubation life at each pore in the surface and subsurface was estimated by the micro-scale Manson-Coffin equation. As shown in Figure 7.9, the crack incubation life (N_{inc}) was lowest at the pore position of D/r = 1 due to a much higher strain concentration generated at this position. By fitting the curves in Figure 7.9, N_{inc} at various stress levels could be estimated as a function of pore depth from the surface (D/r) by

$$\left.\begin{array}{l} N_{inc} = (a_1 \times \frac{D}{r} + a_2)^{a_3},\ \frac{D}{r} \le 1 \\ N_{inc} = (b_1 \times \frac{D}{r} + b_2)^{b_3},\ \frac{D}{r} > 1 \end{array}\right\} \qquad (7.2)$$

where a_1, a_2, a_3, b_1, b_2, b_3 are constants, which vary with the applied cyclic stress, as shown in Table 7.1.

7.3.4 Crack population vs stress

The critical crack incubation life (N_{inc}) in modelling was selected to be 90% of the experimentally measured fatigue life, since it was reported that the initiation of microcracks covered over 90% of the fatigue life under high-cycle fatigue condition. The fatigue crack incubation life as a function of pore position (D/r) at 100% σ_y stress level was shown in Figure 7.10, in which the critical crack incubation life was indicated as the dash line that was 90% of the experimentally measured fatigue life (4.6262 in a log scale) of the alloy. The corresponding critical range of the positions of those crack initiation pores at 100% σ_y applied cyclic stress is illustrated by the window between points A and B, which was calculated to be from 0.98852 to 1.01326 in D/r. This critical range of D/r was also calculated for the applied stress levels of 80% and 110%, respectively. It was found that the critical range of the pore in depth, within which a fatigue crack could be initiated, was very narrow and became a little wider at a higher applied cyclic stress than a relatively low applied cyclic stress.

The number of cracks were quantified in the alloy with a pore area fraction of 0.352% after running the model 1000 times at different stress levels. Figure 7.11 plots the quantified number of cracks obtained by the model against the maximum cyclic stress normalized by the yield strength of the alloy, together with the experimental results. It is shown that the simulated results were consistent with those experimentally measured when the applied maximum cyclic stress was below the yield strength. However, the model could not demonstrate the sudden increase in crack population at UTS, as observed in the experiments.

Many factors such as pore size, morphology, location, orientation as well as clustering, may exert an influence on the imitation of a fatigue crack [157,165]. In order to study these effects, finite element analysis was employed in Al alloys. In cast A356-T6 Al alloy [156,157,161], it was reported that the stress concentration around a pore was certainly dependent on the geometric shape of that pore, and a high stress concentration was generated around the concave roots of the pores in between the secondary dendrite arms, where fatigue damage accumulated and, eventually, a fatigue crack was formed. It was also

found that the closer the pore was to the specimen surface, the higher the stress concentration. A pore that intersected the surface induced the highest stress concentration. For pores either near or at the surface, both the strain and stress concentration factors increased with pore size, meaning that compared to a small surface pore, a larger surface pore was more likely to initiate a fatigue crack due to the higher induced stress and accumulated plastic strain. In cast Al-Si-Cu alloys, shrinkage pores were revealed to be prone to act as crack initiation sites due to their 3-D complex morphology with high stress concentration factor, through the application of Computer-Tomography (μ-CT) and FE simulations [170]. The effects of pore position in depth, pore orientation, pore size and pore clustering on the stress field around a pore was studied by Xu et al. [165] in a cast 713 Al-Zn alloy. It was found that the stress and strain concentrations increased sharply when a pore intercepted the free surface or with the decrease in distance between two pores in the surface when they were within one radius apart in the direction perpendicular to the loading axis. By tilting an elongated (ellipsoidal) pore in the surface, the stress/strain was further increased. The stress/strain was much higher at the intercept point where the pore intercepted the free surface at an acute angle than the intercept point at an obtuse angle. Increasing the pore size could increase the zone of high stress/strain concentration around the pore in the surface. From a continuum standpoint, the primary driving force for fatigue crack formation is assumed to be the local maximum plastic shear strain range ($\Delta\gamma_{max}^{p*}$) with respect to all possible shear strain planes [155,168]. The fatigue crack incubation life could be evaluated based on local Coffin-Manson equation. In cast A356-T6 Al alloy, it was revealed that larger pores and smaller pore spacing resulted in higher $\Delta\gamma_{max}^{p*}$, and thus lower fatigue crack incubation life. As the pore moved away from the free surface to the inside of the material, $\Delta\gamma_{max}^{p*}$ decreased and N_{inc} increased rapidly [155]. It was also reported that the shape of voids was proposed to have a relatively small effect on the driving force for fatigue crack formation, whereas the size of voids had a significant influence on the driving force. In a quantitative 3-D pore-sensitive model for an A713 Al alloy [167], both stress/strain concentration and driving force increased (incubation life decreased) when a pore was located closer to the surface, which were also ascended with the increase in the applied cyclic stress and strain. A sharp increase of driving force occurred in pore size from 5 to ~100 μm in diameter, followed by almost a plateau, meaning that the crack

incubation life was remarkably decreased with increase in pore size from 5 μm to 100 μm and almost saturated when the pore size > 100 μm.

In the present study, the single-sized pore-sensitive model developed by Yang et al. [167] was applied to investigate the effect of porosity on the fatigue crack initiation behavior in the modified AA6061 Al alloy. The pores in the alloy were simplified to be ideal spherical in shape with a diameter of 7 μm. The critical ranges of pore positions for crack initiation were calculated to be quite narrow at all applied stresses without much increase with the increase of the applied stress, outside which nearly no driving force for crack initiation ($\Delta\gamma_{max}^{p*}$) existed (Figures 7.8-7.10), resulting in the nearly same low probability of pores located in the critical ranges of positions no matter at low or high stress level. This might due to the use of ideal spherical pores with only one size of 7 μm in diameter. The experiments illustrated that the crack initiation pores were always aspheric in shape with the larger dimension in depth from the sample surface, and therefore, the consideration of only pore position effect was not enough to describe the crack initiation behavior in the alloy. Other factors such as pore size, shape and orientation should also be considered in simulating fatigue crack initiation at the pores near surface in the model. In the future, methods to characterize the 3-D morphology of the pores should be developed to incorporate the effects of location, size, shape and orientation of the pores into the model. Computer-Tomography (μ-CT) coupled with finite element analysis (FEA) enables the 3-D characterization of defects and cracks, which may provide a new insight into the fatigue analysis of the alloy studied. Focused ion beam (FIB) may also be employed to characterize the 3-D geometries of pores, which has been used in high strength Al alloys to understand the 3-D effect of constituent particles on fatigue crack nucleation behavior [224]. Although this could be very time-consuming to calculate the crack population in the alloy, it would still be desirable, in order to simulate the fatigue crack initiation more accurately in the alloy.

7.4 Conclusions

(1) FEA results demonstrate that both the stress/strain concentration factors (K_t) and crack initiation driving force ($\Delta\gamma_{max}^{p*}$) around a micro-pore increased (fatigue

incubation life decreased) with decreasing the distance between the pore and the alloy surface. They reached peaks when the pore was just buried beneath the surface (i.e., at D/r = 1) in the modified AA6061-T6 Al alloy. The critical ranges of pore positions for crack initiation in surface were very narrow for all applied stress levels without much increase with the increase of the applied stress. No cracks could be initiated outside the critical range as $\Delta\gamma_{max}^{p*}$ was effectively too small.

(2) The population of fatigue cracks initiated at various applied cyclic stresses was quantified using a 3-D pore-sensitive model which computed crack initiation life with a micro-scale Manson-Coffin equation, assuming that pores were all in the same size, 7 μm in diameter. The simulated results were consistent with those experimentally measured when the applied maximum cyclic stress was below the yield strength. However, the model could not capture the sudden increase in crack population at UTS, which was likely to be due to the fact that the effects of pore shape and size were not considered in simulating fatigue crack initiation at the pores near surface in the model.

Table 7.1 Parameters used in Equation 7.2 for different applied stresses

Applied stress	a_1	a_2	a_3	b_1	b_2	b_3
80%σ_y	-2.41739E7	2.42178E7	0.11956	8.46655E7	-8.46115E7	0.11484
100%σ_y	-1.41908E11	1.41916E11	0.0722	1.96906E8	-1.96857E8	0.10354
110%σ_y	-2.12201E11	2.12208E11	0.0695	1.73005E8	-1.72969E8	0.10179

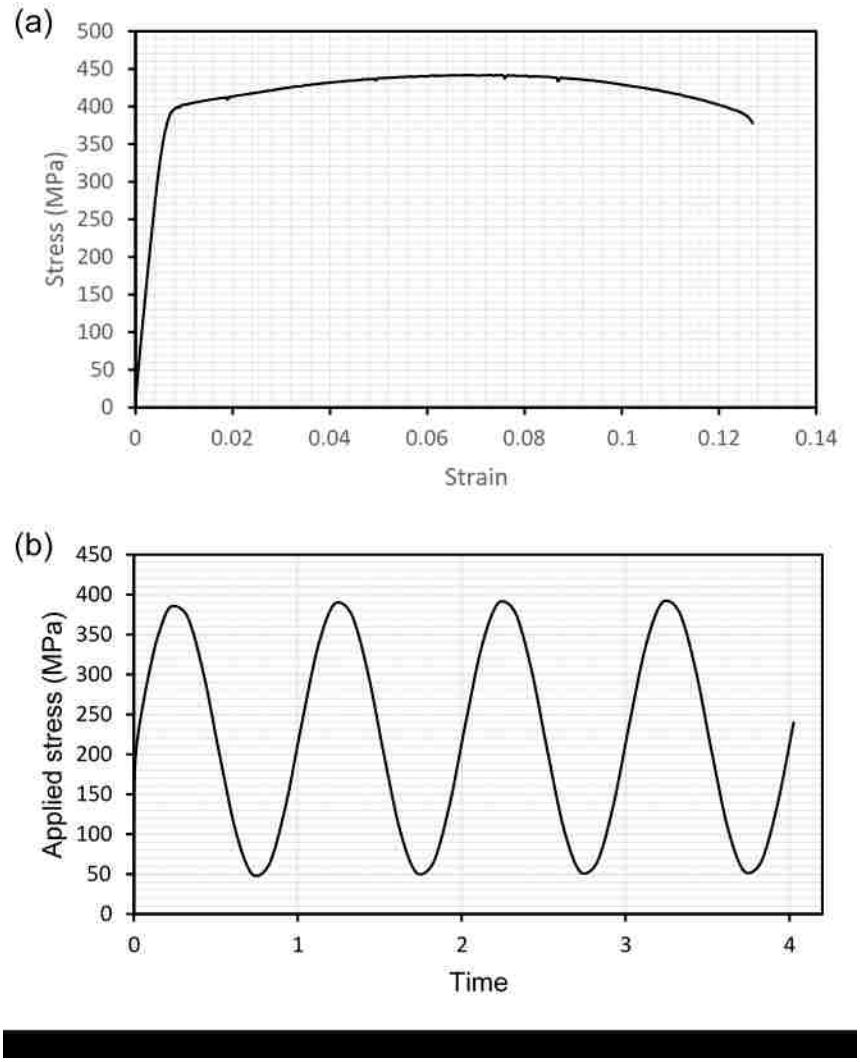

Figure 7.1 (a) Tensile stress-strain curve measured in the modified AA6061-T6 Al alloy; (b) the sinusoidal wave of applied cyclic stress (100% σ_y) curve (at R = 0.1) showing cyclically stable behavior.

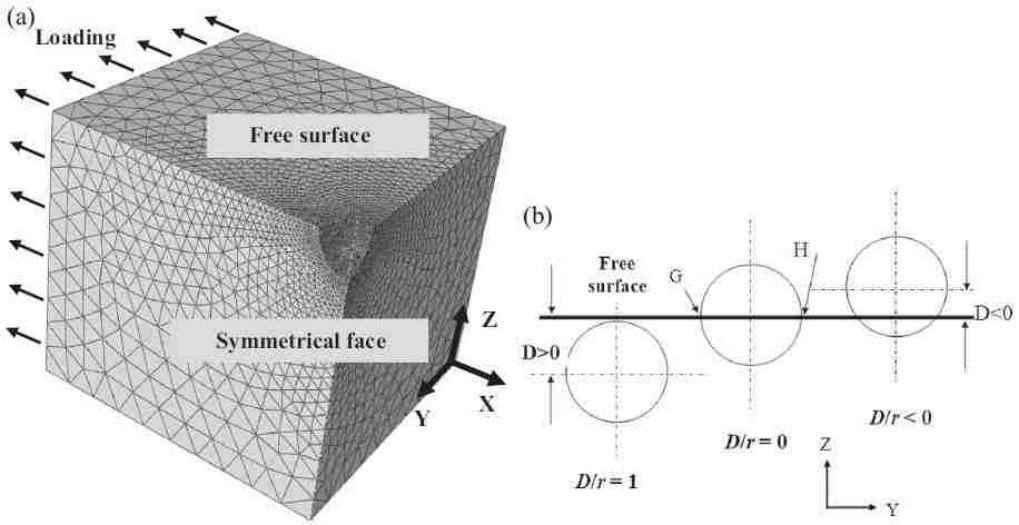

Figure 7.2 (a) A quarter of symmetrical model with mesh; (b) typical pore locations in depth from surface [167].

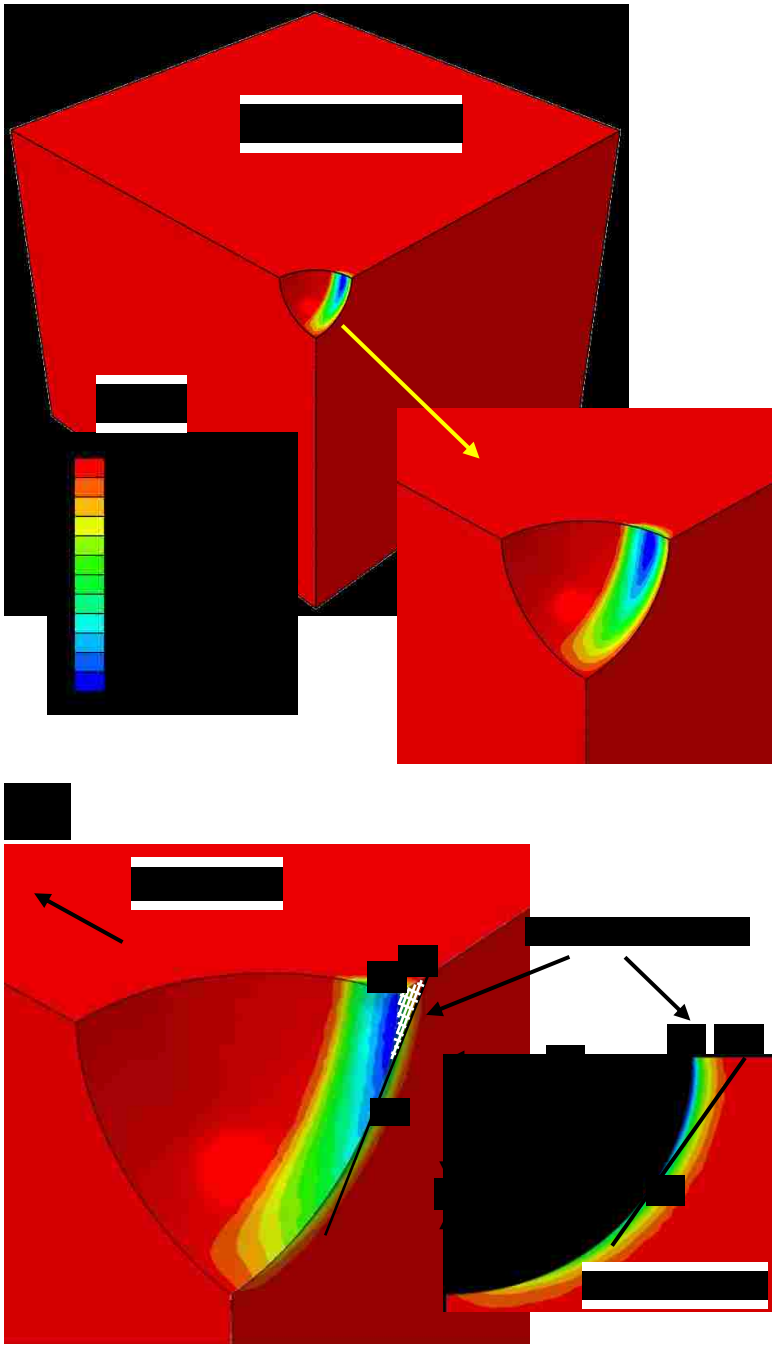

Figure 7.3 Calculation of the average value of maximum shear strain range, $\Delta\gamma_{max}^{p*}$. (a) The contours of maximum plastic shear strain, γ_{max}^{p} (for shear stress/strain: '+' means clockwise, '-' means anti-clockwise. Dark blue is the maximum absolute value in this result); (b) area MNL used to calculate the average value of $\Delta\gamma_{max}^{p*}$ on the critical plane.

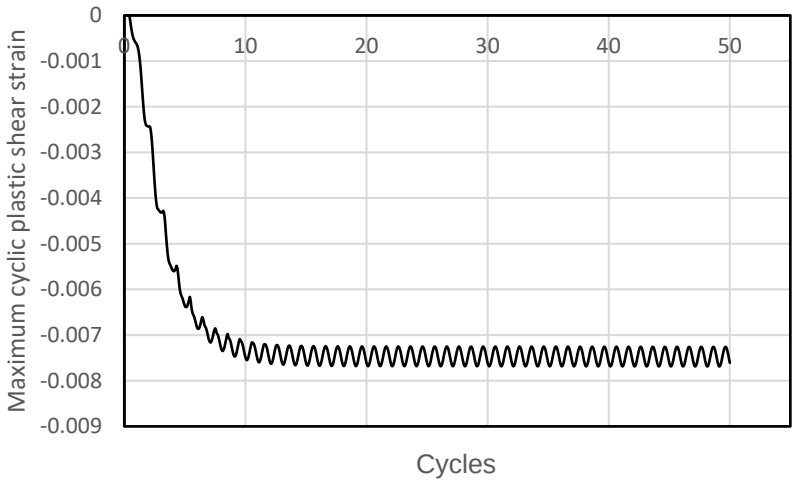

Figure 7.4 The maximum cyclic plastic shear strain, γ_{max}^{p} of the first 50 cycles from FEA simulation results in the region surrounding the micro-pore when the applied maximum cyclic stress is 100% σ_y.

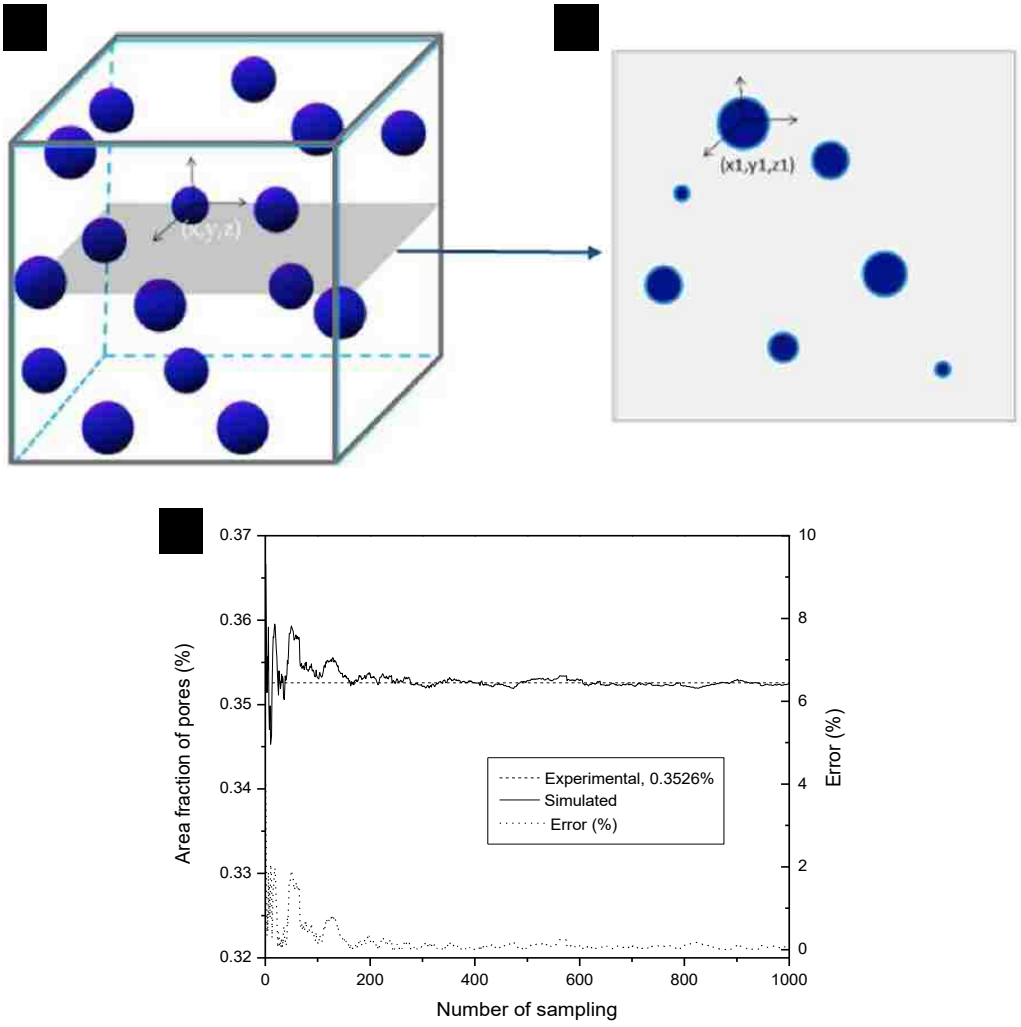

Figure 7.5 A 3-D pore-sensitive model. (a) The schematic of the reconstructed 3-D digital pore structure by randomly distributing spherical pores in a cube [167]; (b) a simulated sample surface by randomly cross-sectioning the digit pore structure [167]; (c) verification of the statistical stability of the model by calculating the average area fraction of the pores on the simulated surfaces as a function of sampling number.

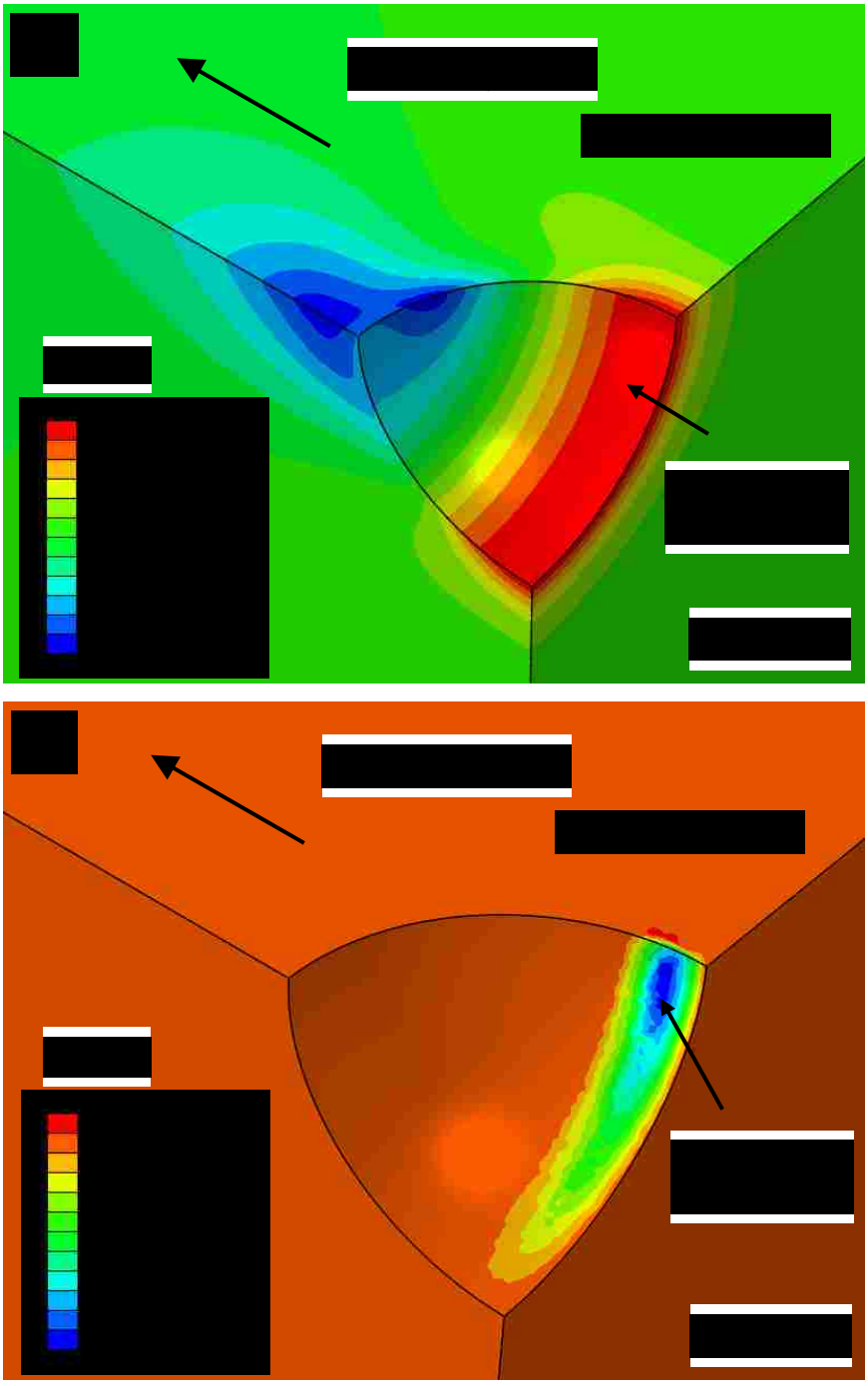

Figure 7.6 The stress/strain fields calculated using an FEA method around a spherical pore at a maximum cyclic stress of 80% σ_y and D/r = 0. (a) The contours of Mises stress around the pore and the maximum value marked by an arrow, the stress unit is 10^6 MPa and the maximum stress is 338.8 MPa; (b) the contours of maximum shear strain around the pore and the maximum value (dark blue) marked by an arrow.

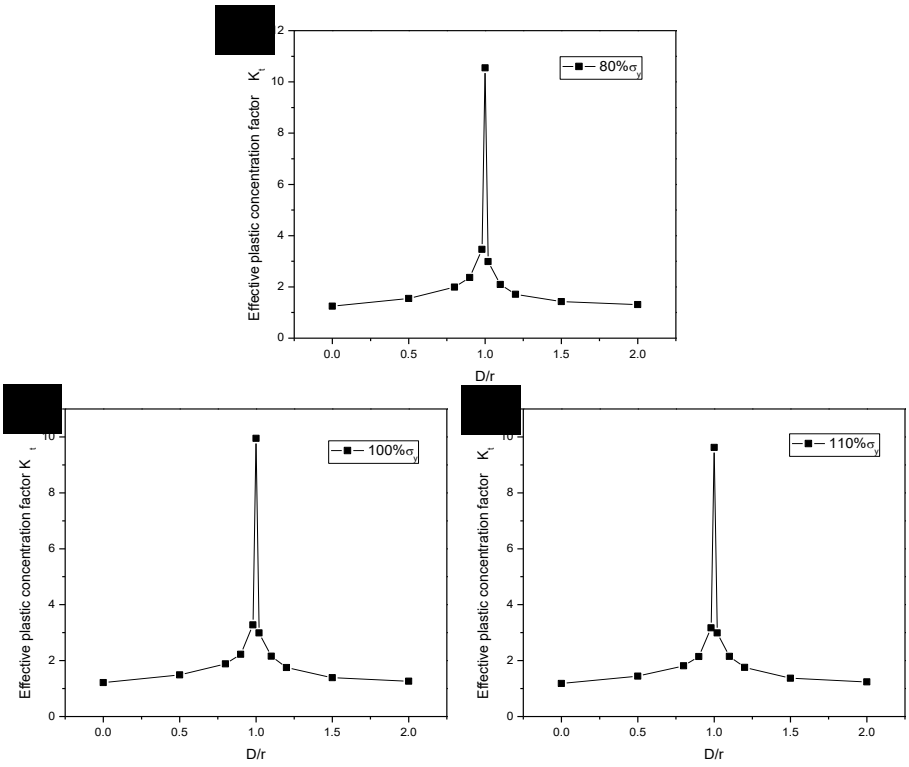

Figure 7.7 The effect of pore depth on stress/strain concentration (K_t) at the applied stress of (a) 80% σ_y; (b) 100% σ_y; and (c) 110% σ_y.

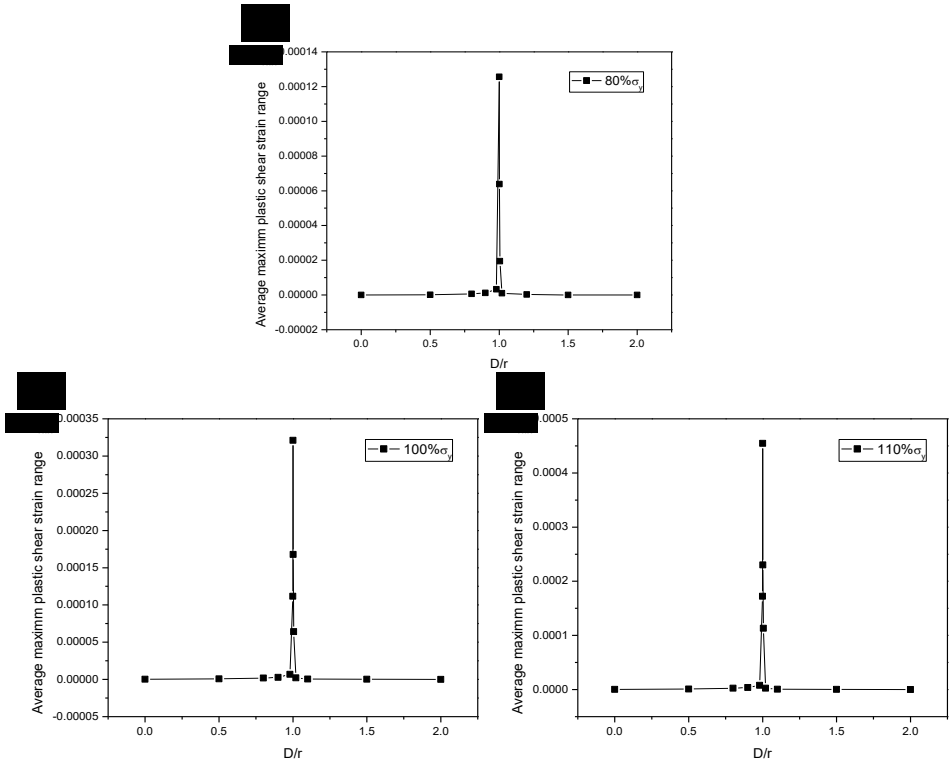

Figure 7.8 The effect of pore depth on maximum shear strain amplitude ($\Delta\gamma_{max}^{p*}$) at the applied stress of (a) 80% σ_y; (b) 100% σ_y; and (c) 110% σ_y.

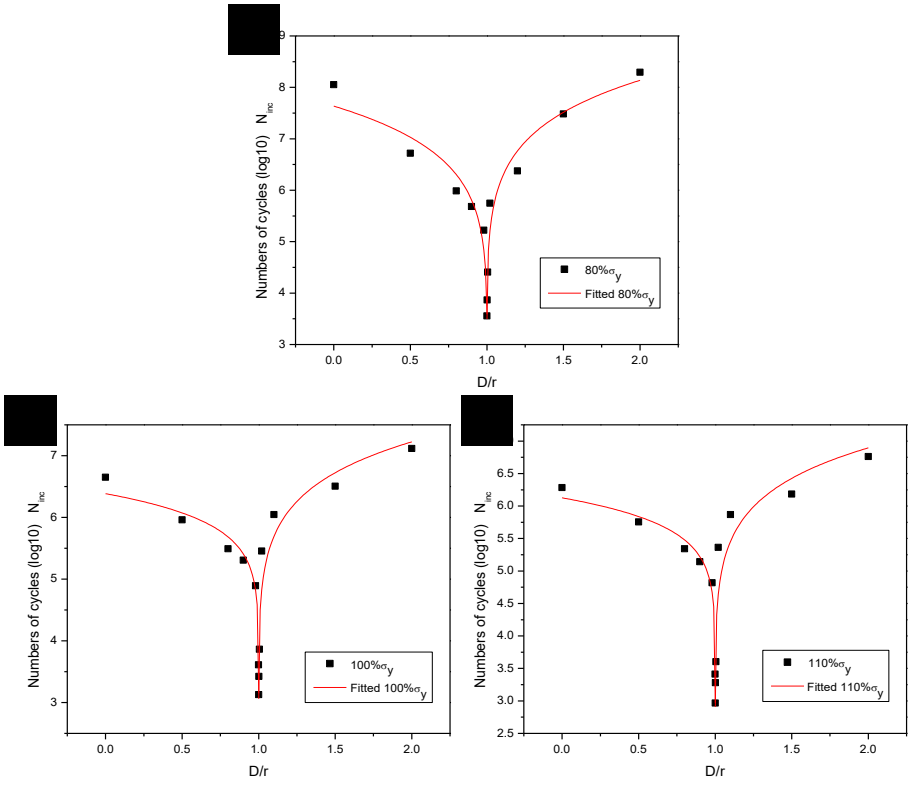

Figure 7.9 The effect of pore depth on crack incubation life (N_{inc}) at the applied stress of (a) 80% σ_y; (b) 100% σ_y; and (c) 110% σ_y.

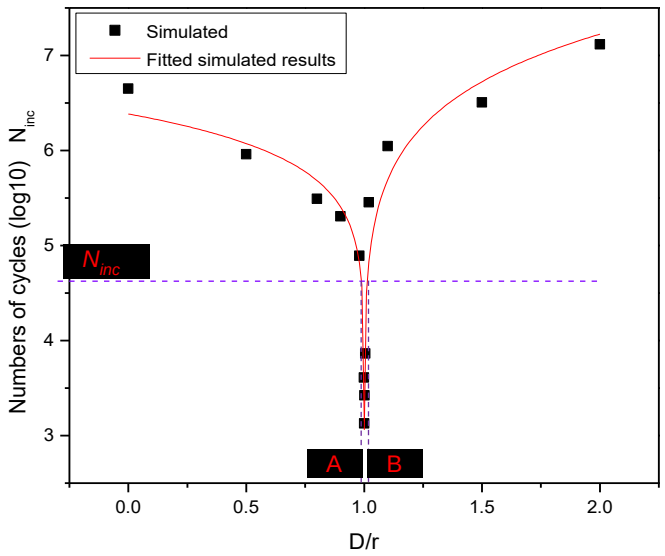

Figure 7.10 The range in pore depth between A and B used to determine crack incubation at pores in surface under the maximum cyclic stress of 100% σ_y.

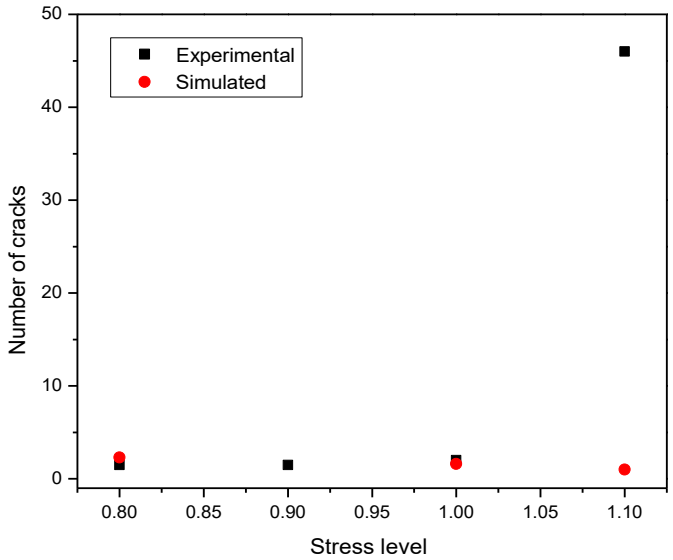

Figure 7.11 Simulated number of fatigue cracks initiated at pores as compared to the experimental result at different stress levels in the studied alloy.

Chapter 8 Conclusions

The formation process of α-dispersoids, their inhibiting effect on recrystallization and fatigue crack initiation behavior of the AA6061 (Al-Mg-Si-Cu) Al alloys modified with the addition of Mn and/or Cr were studied in this study. The formation mechanism of α-dispersoids during high temperature annealing was investigated with the help of STEM and 3-D APT. The strengthening mechanisms in the alloy were also quantitatively interpreted as a function of the annealing temperature. The dispersoid characteristics were quantified on STEM, allowing investigation of the effects of heating rate, content of Mn, low temperature pre-nucleation treatment and homogenization temperature on the formation of α-dispersoids during homogenization in these alloys. Upsetting tests were performed on two modified AA6061 Al alloys with distinctive Mn contents. The effective inhibiting effects of the finely distributed α-dispersoids on recovery and recrystallization were revealed using STEM and EBSD. Four-point bend fatigue tests were carried out on two modified AA6061-T6 Al alloys with different Si contents. OM and SEM were applied to capture a detailed view of the fatigue crack initiation behaviors of the alloys. A quantitative model, which took into account the 3-D effects of pores (7 μm in diameter) on the local stress/strain fields around the pores in surface, was applied to quantification of the fatigue crack population and incubation life in a modified AA6061-T6 Al alloy at various applied cyclic stresses. All the main conclusions drawn from the current research work are summarized as follows:

(1) The as-cast microstructure of the alloys studied consisted of a dominant α-Al(FeMnCr)Si constituent phase, a minor phase of Mg_2Si and a small amount of AlCuMgSi phase. During homogenization treatments, α-phase began to fragment and spheroidize, and Mg_2Si and Q-AlCuMgSi phases were almost fully dissolved into the Al matrix.

(2) During homogenization treatments, a large amount of α-Al(MnFeCr)Si dispersoids were formed in the alloys which had the morphology of rods, platelets and fine blocks, with PFZs being formed surrounding the Mg_2Si phase on grain boundaries. The

formation of α-dispersoids was strongly affected by various homogenization parameters, such as heating rate, content of Mn, low temperature pre-nucleation treatment and homogenization temperature. Increasing the heating rate or homogenization temperature led to a reduction of the number density and an increase in the equivalent size of dispersoids. A higher Mn content resulted in a larger number density, equivalent size and length/width ratio of the dispersoids. Through low temperature pre-nucleation treatment, the number density of dispersoids was increased.

(3) Three sizes of precipitates, i.e., nano-sized (< 100 nm), submicron-sized (< 1 μm) and micron-sized (> 1 μm), existed in the alloys after upsetting. The Cu-containing coarse precipitates (> 1 μm), formed during rapid heating before upsetting, could be fractured during hot deformation, which was detrimental to the mechanical properties of the alloys. The other two sizes of precipitates were fine α-Al(MnCrFe)Si dispersoids that were formed during previous high temperature annealing.

(4) Mn and Cr-containing α-dispersoids with a high number density and thermal stability could effectively retard recovery and recrystallization, and stabilize the microstructure of the alloys during hot deformation and the subsequent solution heat treatment by pinning movement of dislocations and migration of (sub)grain boundaries. A higher content of Mn led to a higher number density of dispersoids, and thus an enhanced retardation effect on recrystallization. An optimum dispersoid size, approximately 0.1~1 μm, was suggested to have the best dislocation pinning effect.

(5) Three typical morphologies of fine α-Al(MnCrFe)Si dispersoids, i.e., rods, platelets and fine blocks, were observed in the alloy after 4 hours of homogenization treatment at 460 and 550 ˚C, respectively. Strings of fine block-like α-dispersoids were also found after the homogenization treatment at 460 ˚C.

(6) Mn distributed non-uniformly with a Mn-depleted region surrounding the Mg_2Si phase at GBs in the as-cast alloy. In the early stage of homogenization, in Mn-rich regions, Mn segregated at the interface between the long lath-shaped Q-phase and the matrix, which triggered the transformation of Q-phase into strings of Mn-rich precipitates. Meanwhile, Q-phase still remained unchanged in the Mn-depleted regions without segregation of Mn at the Q-phase/matrix interface. This indicated that the segregation of Mn was essential to induce the transformation of Q-phase into α-dispersoids, and that Q-phase was considered to be the precursor phase for the formation of α-dispersoids.

(7) With further increase in the homogenization temperature and time, α-dispersoids gradually evolved, with the participation of other dispersoids-forming elements in addition to Mn. The atomic ratio of Mn/Si was found to be close to 1 in the α-dispersoids when the dispersoids were fully developed.

(8) A significant dispersoid hardening effect could be achieved in the alloy after 4 hours of annealing at 460 ˚C, while after annealing the alloy at 550 ˚C for 4 hours, strengthening by a higher level of solid solution of alloying elements, such as Mn, Cr, Fe, Si, etc., played a more important role in determining the strength of the alloy, as a result of increasing dissolution of dispersoids thereby increasing the supersaturation of the alloying elements in the alloy at 550 ˚C.

(9) The micro-pores were observed and statistically characterized in the two modified AA6061-T6 Al alloys with various Si contents. The average diameters of the pores on the surface were 3.2 and 2.64 μm, the average area fractions of the pores were 0.24% and 0.35%, and the average pore densities were 218 and 449 mm^{-2} for the alloys with low and high Si content, respectively. These pores were formed during solidification or due to overheating that partially melted the Si-containing particles at GBs in the alloys during homogenization.

(10) The fatigue limits were measured to be approximately 224 and 283.5 MPa for the alloys with low and high Si content, respectively, at a run-out number of 5.5 x 10^6 cycles in four-point bend tests.

(11) The number of cracks observed on surface was found to be very small (1~3) and barely increased with the applied stress, when the applied stress was below the yield strength. However, it was increased sharply with the increase of the applied stress to approximately the ultimate tensile strength.

(12) The fatigue crack initiation behaviors of the alloys were dramatically influenced by the tunnel-shaped pores in the alloys. Fatigue cracks were predominantly initiated at the pores at or very close to surface, which were always aspheric in shape with the larger dimension in depth from the sample surface, with the minority of the cracks being initiated at the second phase Mg_2Si-particles or at the interface between the Mg_2Si-particle and the matrix.

(13) FEA results demonstrate that both the stress/strain concentration factors (K_t) and crack initiation driving force ($\Delta\gamma_{max}^{p*}$) around a micro-pore increased (fatigue incubation life decreased) with decreasing the distance between the pore and the alloy surface. They reached peaks when the pore was just buried beneath the surface (i.e., at D/r = 1) in the modified AA6061-T6 Al alloy. The critical ranges of pore positions for crack initiation in surface were very narrow for all applied stress levels without much increase with the increase of the applied stress. No cracks could be initiated outside the critical range as $\Delta\gamma_{max}^{p*}$ was effectively too small.

(14) The population of fatigue cracks initiated at various applied cyclic stresses was quantified using a 3-D pore-sensitive model which computed crack initiation life with a micro-scale Manson-Coffin equation, assuming that pores were all in the same size, 7 μm in diameter. The simulated results were consistent with those experimentally measured, when the applied maximum cyclic stress was below the yield strength. However, the model could not capture the sudden increase in crack population at UTS,

which was likely to be due to the fact that the effects of pore shape and size were not considered in simulating fatigue crack initiation at the pores near surface in the model.

References

[1] G.E. Totten, D.S. MacKenzie, Handbook of Aluminum: Vol. 1: Physical Metallurgy and Processes, Marcel Dekker, New York, 2003.
[2] R.E. Smallman, A.H.W. Ngan, Modern Physical Metallurgy, 8th edition, Elsevier, 2014.
[3] Z. Liang, Clustering and Precipitation in Al-Mg-Si Alloys, doctoral thesis, Berlin, 2012.
[4] ASM Handbook, 10th edition, 1992.
[5] J.R. Davis, Alloying Understanding the Basics, ASM International, 2001.
[6] D. Hull, D.J. Bacon, Introduction to Dislocations, 5th edition, Elsevier, 2011.
[7] M.A. Meyers, K.K. Chawla, Mechanical Behavior of Materials, 2nd edition, Cambridge, 2009.
[8] R.W. Hertzberg, Deformation and Fracture Mechanics of Engineering Materials, 4th edition, John Wiley & Sons, 1996.
[9] D. Laughlin, K. Hono, Physical Metallurgy, 5th edition, Elsevier, 2014.
[10] G. Gottstein, Physical Foundations of Materials Science, Springer, 2004.X. Xu, G.
[11] X. Xu, G. Wu, B. Wang, F. Zhang, Y. Luo, T. Song, C. Cheng, L. Pan, X. Cheng, Journal of Shanghai Jiaotong University, 45 (2011) 911-914.
[12] K.M. Youssef, R.O. Scattergood, K.L. Murty, C.C. Koch, Scripta Materialia, 54 (2006) 251-256.
[13] G.P.M. Leyson, L.G. Hector Jr., W.A. Curtin, Acta Materialia, 60 (2012) 3873-3884.
[14] K. Liu, X.-G. Chen, Materials and Design 84 (2015) 340-350.
[15] A.M.F. Muggerud, E.A. Mørtsell, Y. Li, R. Holmestad, Materials Science and Engineering A, 567 (2013) 21-28.
[16] Y. Li, A.M.F. Muggerud, A. Olsen, T. Furu, Acta Materialia, 60 (2012) 1004-1014.
[17] J.Y. Uan, L.H. Chen, T.S. Lui, Scripta Materialia, 36 (1997) 1391-1395.
[18] K.L. Kendig, D.B. Miracle, Acta Materialia, 50 (2002) 4165-4175.
[19] E.L. Huskins, B. Cao, K.T. Ramesh, Materials Science and Engineering A, 527 (2010) 1292-1298.
[20] L. Lodgaard, N. Ryum, Mater. Sci. Technol., 16 (2000) 599-604.
[21] N. C. W. Kuijpers, Intermetallic phase transformations during homogenization of 6xxx Al alloys, a literature review, Internal report of the Netherlands Institute for Metals Research (NIMR), The Netherlands, 2000.
[22] L.F. Mondolfo, Aluminum alloys: structure and properties, Butterworth-Heinemann, 1976.
[23] H. Tanihata, T. Sugawara, K. Matsuda, S. Ikeno, J. Mat. Sci., 34 (1999) 1205-1210.
[24] P. Skjerpe, Metall. Trans. A, 18 (1987) 189-200.
[25] J.G. Zheng, R. Vincent, J.W. Steeds, Phil. Mag. A, 80 (2000) 493-500.
[26] A.L. Dons, Z. Metallkde, 75 (1984) 170-174.
[27] A. Griger, V. Stefániay, A. Lendvai, T. Turmezey, Aluminum, 65 (1989) 1049-1056.
[28] D.J. Skinner, R. L. Bye, D. Raybould, A. M. Brown, Scripta Met., 20 (1986) 867-872.
[29] M. Cooper, K. Robinson: Acta Cryst., 20 (1966) 614-617.
[30] M. Cooper, Acta Cryst., 23 (1967) 1106-1107.
[31] P. Donnadieu, G. Lapasset, T.H. Sanders, Philos. Mag. Lett., 70 (1994) 319-326.
[32] Y. Birol, Z. Metallkd., 89 (1998) 501-506.

[33] P. Donnadieu, G. Lapasset, B. Thanaboonsombut, T. H. Sanders, The 4th international conference on aluminum alloys, Atlanta, Georgia, USA (1994) 668-675.
[34] D.T.L. Alexander, A.L. Greer, Acta. Mat., 50 (2002) 2571-2583.
[35] H. Westengen, Z. Metallkd., 73 (1982) 360-368.
[36] T. Turmezey, Mater. Sci. Forum, 13-14 (1987) 121-132.
[37] K. Sugiyama, N. Kaji, K. Hiraga, Acta Cryst., C 54 (1998) 445-447.
[38] M.H. Mulazimoglu, A. Zaluska, J.E. Gruzleski, F. Paray, Metall. Mater. Trans., A 27 (1996) 929-936.
[39] G. Phragmen, J. Inst. Metals, 77 (1950) 489-552.
[40] Chr. Rømming, Acta Cryst., B 50 (1994) 307-312.
[41] H. Tanihata, K. Matsuda, S. Ikeno, Mater. Sci. Forum, 217-222 (1996) 809-814.
[42] A. Valles, R. P. L. Orsetti, R. Tosta, Proc. of the International Conference on Aluminum Alloys, Toyohashi, Japan (1998) 2123-2128.
[43] S. Zajac, B. Hutchinson, A. Johansson, L.O. Gullman, Mat. Sci. Tech., 10 (1994) 323-333.
[44] T. Sheppard, Extrusion of Aluminum Alloys, Springer, 1999.
[45] L. Lodgaard, N. Ryum, Mater. Sci. Eng. A, 283 (2000) 144-152.
[46] R.A. Jeniski Jr., B. Thanaboonsombut, T.H. Sanders Jr., Metall. Mater. Trans. A, 27A (1996) 19-27.
[47] G. Zhang, H. Nagaumi, Y. Han, Y. Xu, C.M. Parish, T. Zhai, Mater. Sci. Forum, 877 (2016) 172-179.
[48] R. Hu, T. Ogura, H. Tezuka, T. Sato, Q. Liu, J. Mater. Sci. Technol., 26(3) (2010) 237-243.
[49] D.H. Lee, J.H. Park, S.W. Nam, Mater. Sci. Technol., 15 (1999) 450-55.
[50] J.E. Yoo, A. Shan, I.G. Moon, S.J. Maeng, J. Mater. Sci., 34 (1999) 2679-2683.
[51] H. Westengen, O. Reiso, L.Auran, Aluminum, 56 (1980) 768-775.
[52] K. Robinson, Acta Cryst., 6 (1953) 854-859.
[53] K. Strobel, E. Sweet, M. Easton, J.F. Nie and M. Couper, Materials Science Forum, 654-656 (2010) 926-929.
[54] H. Hirasawa, Scripta Met., 9 (1975) 955-958.
[55] R. Vissers, M.A. van Huis, J. Jansen, H.W. Zandbergen, C.D. Marioara and S.J. Andersen, Acta Materialia, 55 (2007) 3815-3823.
[56] C.D. Marioara, S.J. Andersen, J. Jansen, H.W. Zandbergen, Acta Mater., 49 (2001) 321-328.
[57] G.A. Edwards, K. Stiller, G.L. Dunlop, M.J. Couper, Acta Mater., 46 (1998) 3893-3904.
[58] X. Fang, M. Song, K. Li and Y. Du, J. Min. Metall. Sect. B-Metall., 46 B (2010) 171-180.
[59] S.J. Anderson, H.W. Zandbergen, J.E. Jansen, C. Taeholt, U. Tundal, O. Reiso, Acta Mater., 46 (1998) 3283-3298.
[60] S. Pogatscher, H. Antrekowitsch, H. Leitner, T. Ebner and P.J. Uggowitzer, Acta Materialia, 59 (2011) 3352-3363.
[61] M. Cabibbo, S. Spigarelli, E. Evangelista, Materials Characterization, 49 (2003) 193-202.
[62] N. Maruyama, R. Uemori, N. Hashimoto, M. Saga, M. Kikuchi, Scr. Mater., 36 (1997) 89-93.

[63] M. Van Rooyen, J.A. Sinte Maartensdijk, E.J.Mittemeijer, Metall. Trans. A, 19 (1988) 2433-2443.
[64] A. Perovic, D.D. Perovic, G.C. Weatherly, D.J. Llyd, Scr. Mater., 41 (1999) 703-708.
[65] C. Ravi, C. Wolverton, Acta Materialia, 52 (2004) 4213-4227.
[66] M.H. Jacobs, Philos. Mag., 26 (1972) 1-13.
[67] K. Matsuda, S. Ikeno, H. Matsui, T. Sato, Mater. Trans. A, 36 (2005) 2007
[68] K. Matsuda, Y. Sakaguchi, Y. Miyata, Y. Uetani, T. Sato, A. Kamio, S. Ikeno, J. Mater. Sci., 35 (2000) 179-189.
[69] C. Wolverton, Acta Mater., 49 (2001) 3129-3142.
[70] G.C. Weatherly, A. Perovic, N.K. Mukhopadhyay, D.J. Lloyd, D.D.Perovic, Metall. Mater. Trans., A 32A (2001) 213-218.
[71] L. Arnberg, B. Aurivillius, Acta Chem. Scand. A, 34 (1980) 1-5.
[72] C. Cayron, L. Sagalowicz, O. Beffort, P.A. Buffat, Phil Mag A, 79 (1999) 2833-2851.
[73] A. Biswas, D.J. Siegel, D.N. Seidman, Acta Mater., 75 (2014) 322-336.
[74] D.J. Chakrabarti, D.E. Laughlin, Progress in Mater. Sci., 49 (2004) 389-410.
[75] H.S. Hasting, J.C. Walmsley, A.T.J. Van Helvoort, C.D. Marioara, S.J. Andersen, R. Holmestad, Phil. Mag. Lett., 86 (2006) 589-597.
[76] S.D. Dumolt, Scripta Metall., 18 (1984) 1347-1350.
[77] K. Matsuda, Y. Uetani, T. Sato, S. Ikeno, Metall. Mater. Trans. A, 32 (2001) 1293-1299.
[78] R.S. Yassar, D.P. Field, H. Weiland, Scripta Mater., 53 (2005) 299-303.
[79] K. Matsuda, T. Kawabata, Y. Uetani, Mater. Sci. Forum, 426-432 (2003) 375-380.
[80] C. Cayron, These No. 2246. Ecole Polytech. Fed., Lausanne, 2000.
[81] L. Sagalowicz, G. Hug, D. Bechet, P. Sainfort, and G. Lapasset, Proc. Fourth International Conference on Aluminum Alloys, Atlanta, USA (1994), 636-643.
[82] C.D. Marioara, S.J. Andersen, T.N. Stene, H. Hasting, J. Walmsley, A.T.J.Van Helvoort and R. Holmestad, Philosophical Magazine, 87 (23) (2007) 3385-3413.
[83] A. Gaber, A. M. Ali, K. Matsuda, T. Kawabata, T. Yamazaki, S. Ikeno, J. Alloys and Compounds, 432 (2007) 149-155.
[84] M. Jin, J. Li, G.J. Shao, J. Alloys and Compounds, 437 (2007) 146-150.
[85] W.F. Miao, D.E. Laughlin, Metall. Mater. Trans. A, 31A (2000) 361-371.
[86] J. Buha, R.N. Lumley, A.G. Crosky, K. Hono, Acta Materialia, 55 (2007) 301-3024.
[87] H.J. Humphreys, M. Hatherly: Recrystallization and Related Annealing Phenomena, 2nd ed., Elsevier, 2004,
[88] Y. Xu, H. Nagaumi, Y. Han, G. Zhang, T. Zhai, Metallurgical and Materials Transactions A, 48 (2017) 1355-1365.
[89] S. Gourdet, F. Montheillet, Mater. Sci. Eng. A, 283 (2000) 274-288.
[90] R.D. Doherty, D.A. Hughes, F.J. Humphreys, J.J. Jonas, D. Juul Jensen, M.E. Kassnerf, W.E. King, T.R. McNelley, H.J. McQueen, A.D. Rollett, Mater. Sci. Eng. A, 238 (1997) 219-274.
[91] H.E. Hu, L. Zhen, L. Yang, W.Z. Shao, B.Y. Zhang, Mater. Sci. Eng. A, 488 (2008) 64-71.
[92] H.J. McQueen, W. Blum, Mater. Sci. Eng. A, 290 (2000) 95-107.
[93] X.Y. Liu, Q.L. Pan, Y.B. He, W.B. Li, Z.M. Yin: Mater. Sci. Eng. A, 500 (2009) 150-154.

[94] R. Kaibyshev, O. Sitdikov, A. Goloborodko, T. Sakai, Mater. Sci. Eng. A, 344 (2003) 348-356.
[95] X. Zhang, M. Xu, J. Tang, J. Ou, J. Cent. South Univ. Technol., 17 (2010) 425-430.
[96] J. Sarkar, Y.V.R.K. Prasad, M.K. Surappa, J. Mater. Sci., 30 (1995) 2843-2848.
[97] Y.V.R.K. Prasad, K.P. Rao, Mater. Sci. Eng. A, 391 (2005) 141-150.
[98] M. Cabibbo, E. Evangelista, and S. Spigarelli, Metallurgical and Materials Transactions A, 35A (2004) 293-300.
[99] C. Zener, C.S. Smith, Trans. Metall. Soc. AIME, 175 (1948) 11-51.
[100] A.R. Eivani, H. Ahmed, J. Zhou, J. Duszczyk, Metallurgical and Materials Transactions A, 40A (2009) 2435-2446.
[101] S. Suresh, Fatigue of Materials, 2nd ed., Cambridge University Press, 1998.
[102] U. Krupp, Fatigue Crack Progagation in Metals and Alloys, WILEY-VDH Verlag GmbH & Co. KGaA, 2007.
[103] J. Schijve, Fatigue of Structures and Materials, 2nd edition, Springer, 2009.
[104] K. Sobczyk, B. Spencer Jr, Random fatigue: from data to theory, Academic Press, 1992.
[105] R.L. Norton, Machine Design: An Integrated Approach, 3rd edition, Prentice-Hall, 2006.
[106] T. Zhai, Metall. Mater. Trans. A, 37A (2006) 3139-3147.
[107] Y. Jin, P. Cai, Q. Tian, T. Zhai, Fatigue & Fracture of Engineering Materials & Structures, 39 (2016) 696-711.
[108] W. Weibull, Proc. R. Swed. Inst. Eng. Res., 151 (1939) 1-45.
[109] Y. Jin, P. Cai, W. Wen, H. Nagaumi, B. Xu, Y. Zhang, T. Zhai, Mater. Sci. Eng. A, 622 (2015) 7-15.
[110] Y. Zhang, J. Xu, T. Zhai, Mater. Sci. Eng. A, 527 (2010) 3639-3644.
[111] C.S. Barrett, Structure of Metals (crystallographic method, priciples and data), McGRAW-Hill, 1943.
[112] H. Mughrabi, R. Wang, K. Differt, U. Essmann, Fatigue Mechanisms, ASTM, 1983.
[113] U. Essmann, U. Gosele, H. Mughrabi, Philos. Mag. A, 44 (1981) 405-426.
[114] A. Hunsche, P. Neumann, Acta Metallurgica, 34 (1986) 207-217.
[115] K.K. Sankaran, R. Perez, K.V. Jata, Advanced Materials & Processes, 158 (2000) 53-54.
[116] C. Scheerder, Delft University of Technology, 1992.
[117] W.A. Wood, Philos Mag, 3 (1958) 692-699.
[118] P.J.E. Forsyth, Nature, 171 (1953) 172-173.
[119] C. Laird, J.M. Finney, D. Kuhlmannwilsdorf, Materials Science and Engineering, 50 (1981) 127-136.
[120] A.S. Cheng, C. Laird, Materials Science and Engineering, 51 (1981) 111-121.
[121] B.L. Boyce, J.R. Michael, P.G. Kotula, Acta Materialia, 52 (2004) 1609-1619.
[122] A. Zabett, A. Plumtree, Fatigue & Fracture of Engineering Materials & Structures, 18 (1995) 801-809.
[123] J. Antonopoulos, L. Brown, A. Winter, Philosophical Magazine, 34 (1976) 549-563.
[124] K. Tanaka, T. Mura, J. Appl. Mech.-Trans. ASME, 48 (1981) 97-103.
[125] D. Sigler, M.C. Montpetit, W.L. Haworth, Metallurgical Transactions A, 14 (1983) 931-938.

[126] D.G. Harlow, J. Nardiello, J. Payne, International Journal of Fatigue, 32 (2010) 505-511.
[127] J. Payne, G. Welsh, R.J. Christ, Jr., J. Nardiello, J.M. Papazian, International Journal of Fatigue, 32 (2010) 247-255.
[128] Y. Xue, H. El Kadiri, M.F. Horstmeyer, J.B. Jordon, H. Weiland, Acta Materialia, 55 (2007) 1975-1984.
[129] G. Patton, C. Rinaldi, Y. Brechet, G. Lormand, R. Fougeres, Mat Sci. Eng. A, 254 (1998) 207-218.
[130] Z.Q. Zheng, B. Cai, T. Zhai, S.C. Li, Mat Sci Eng A, 528 (2011) 2017-2022.
[131] R. Chang, W.L. Morris, O. Buck, Scripta Metallurgica, 13 (1979) 191-194.
[132] S.S. Singh, C. Schwartzstein, J.J. Williams, X. Xiao, F. De Carlo, N. Chawla, J Alloy Compound, 602 (2014) 163-174.
[133] W.L. Morris, MTA, 11 (1980) 1117-1123.
[134] W.L. Morris, MTA, 10 (1979) 5-11.
[135] C.Y. Kung, M.E. Fine, Metallurgical Transactions a-Physical Metallurgy and Materials Science, 10 (1979) 603-610.
[136] W.L. Morris, MTA, 9 (1978) 1345-1348.
[137] W.L. Morris, MTA, 8 (1977) 1087-1093.
[138] E.A. DeBartolo, B.M. Hillberry, International Journal of Fatigue, 20 (1998) 727-735.
[139] C.B. Fuller, A.R. Krause, D.C. Dunand, D.N. Seidman, Mat. Sci. Eng. A, 338 (2002) 8-16.
[140] T.S. Srivatsan, D. Kolar, P. Magnusen, Mater Design, 23 (2002) 129-139.
[141] J.C.W. Vandekasteele, D. Broek, Eng. Fract. Mech., 9 (1977) 625-635.
[142] R. Gurbuz, S.P. Alpay, Scripta Metallurgica Et Materialia, 30 (1994) 1373-1376.
[143] W.L. Morris, O. Buck, H.L. Marcus, Metallurgical Transactions A, 7 (1976) 1161-1165.
[144] S.G. Grosskreutz J, Proceedings of second international conference on fracture, Chapman and Hall, Brighton, UK, 1969.
[145] S. Pearson, Eng. Fract. Mech., 7 (1975) 235-247.
[146] S.E. Axter, W.B. Jones, D.H. Polonis, Metallography, 8 (1975) 425-438
[147] H. Weiland, J. Nardiello, S. Zaefferer, S. Cheong, J. Papazian, D. Raabe, Engineering Fracture Mechanics, 76 (2009) 709-714.
[148] A.K. Vasudevan, R.D. Doherty, Acta Metallurgica, 35 (1987) 1193-1219.
[149] D.L. Davidson, R.G. Tryon, M. Oja, R. Matthews, K.S.R. Chandran, Metall. Mater. Trans. A, 38A (2007) 2214-2225.
[150] P. Mulvihill, C.J. Beevers, Mechanical Engineering Publications, eds. K. J. Miller and E. R. de los Rios, (1986) 203-213.
[151] J.P. Anson, J.E. Gruzleski, Materials Characterization, 43 (1999) 319-335.
[152] X. Zhu, J.W. Jones, J.E. Allison, Metall Mater Trans A, 39A (2008) 2681-2688.
[153] K.S. Chan, P. Jones, Q.G. Wang, Mat Sci Eng a-Struct, 341 (2003) 18-34.
[154] Q.G. Wang, D. Apelian, D.A. Lados, Journal of Light Metals, 1 (2001) 73-84.
[155] J.H. Fan, D.L. McDowell, M.F. Horstemeyer, K. Gall, Eng. Fract. Mech., 70 (2003) 1281-1302.
[156] Y.X. Gao, J.Z. Yi, P.D. Lee, T.C. Lindley, Fatigue & Fracture of Engineering Materials & Structures, 27 (2004) 559-570.
[157] P. Li, P.D. Lee, D.M. Maijer, T.C. Lindley, Acta Materialia, 57 (2009) 3539-3548.

[158] H.T. Pang, P.A.S. Reed, Int. J. Fatigue, 25 (2003) 1089-1099.
[159] M. Couper, A. Neeson, J. Griffiths, Fatigue & Fracture of Engineering Materials & Structures, 13 (1990) 213-227.
[160] H. Ammar, A. Samuel, F. Samuel, Mater. Sci. Eng. A, 473 (2008) 65-75.
[161] J.Z. Yi, Y.X. Gao, P.D. Lee, H.M. Flower, T.C. Lindley, Metallurgical and Materials Transactions A, 34A (2003) 1879-1890.
[162] Y. Zhang, J. Xu, T. Zhai, Mater. Sci. Eng. A, 527 (2010) 3639-3644.
[163] J.C. Ting, F.V. Lawrence, Fatigue & Fracture of Engineering Materials & Structures, 16 (1993) 631-647.
[164] S. Benedictus-deVries, A. Bakker, G. Janssen, H. de Wit, Journal of engineering materials and technology, 126 (2004) 199-203.
[165] Z.Q. Xu, W. Wen, T.G. Zhai, Metall. Mater. Trans. A, 43A (2012) 2763-2770.
[166] S.E. Stanzltschegg, H.R. Mayer, A. Beste, S. Kroll, International Journal of Fatigue, 17 (1995) 149-155.
[167] L. Yang, P. Cai, Z. Xu, Y. Jin, C. Liang, F. Yin, T. Zhai, International Journal of Fatigue 96 (2017) 185-195.
[168] K. Gall, M.F. Horstemeyer, B.W. Degner, D.L. McDowell, J.H. Fan, Int. J. Fract., 108 (2001) 207-233.
[169] D. McDowell, K. Gall, M. Horstemeyer, J. Fan, Engineering Fracture Mechanics, 70 (2003) 49-80.
[170] M.Wicke, M. Luetje, I. Bacaicoa, A. Brueckner-Foit, Procedia Structural Integrity 2 (2016) 2643-2649.
[171] G. Nicoletto, R. Konecna, S. Fintova, International Journal of Fatigue. 41 (2012) 39-46.
[172] T. Zhai, Y.G. Xu, J.W. Martin, A.J. Wilkinson, G.A.D. Briggs, Int. J. Fatigue, 21 (1999) 889-894.
[173] D. B. Williams and C. B. Carter, Transmission Electron Microscopy, 2nd edition, Springer, 2009.
[174] Y. Leng, Materials Characterization (Introduction to Microscopic and Spectroscopic Methods), John Wiley & Sons, 2008.
[175] M.K. Millera, T.F. Kelly, K. Rajanc, S.P. Ringerd, materialstoday, 15 (2012) 158-165.
[176] A. Cerezo, P.H. Cliftonc, M.J. Galtreyd et al., materialstoday, 10 (2007) 36-42.
[177] B. Gault, M.P. Moody, J.M. Cairney, S.P..Ringer. Atom Probe Microscopy, Springer, 2012.
[178] D. McMullan, Scanning, 17 (1995) 175-185.
[179] J. Goldstein, D.E. Newbury, P. Echlin, D.C. Joy, A.D. Romig Jr, C.E. Lyman, C. Fiori, E. Lifshin, Scanning electron microscopy and X-ray microanalysis: a text for biologists, materials scientists, and geologists, Springer Science & Business Media, 2012.
[180] D.J. Dingley, K. Baba-Kishi, V. Randle, An Atlas of Backscatter Kikuchi Diffraction Patterns, Institute of Physics Publishing, Bristol, 1994.
[181] G. Gottstein, O. Engler, Journal De Physique IV, 3 (1993) 2137-2142.
[182] S. Kikuchi, J. Appl. Phys., 5 (1928) 83-96.
[183] GB/T4340.1-2009. Metallic materials-Vickers hardness test - Part 1: Test method. Beijing: Standards Press of China; 2009.

[184] GB/T228.1-2010. Metallic materials-Tensile testing - Part 1: Method of test at room temperature. Beijing: Standards Press of China; 2011.
[185] A.M.F. Muggerud, PhD Thesis, Trondheim, Norway, 2014.
[186] D.L. Logan, A first course in the finite element method, Cengage Learning, 2011.
[187] A. Gilat, MATLAB An Introduction with Applications, 6th edition, Wiley, 2017.
[188] Y. Li, L. Arnberg, Acta Mater., 51 (2003) 3415-3428.
[189] Y. Han, K. Ma, L. Li, W. Chen, H. Nagaumi, Mater. Design, 39 (2012) 418-424.
[190] G. Sha, K.A.Q O' Reilly, B. Cantor, Mater. Sci. Forum, 519-521 (2006) 1721-1726.
[191] G. Zhang et al., unpublished results.
[192] Ch.-A. Gandin, A. Jacot, Acta Materialia, 55 (2007) 2539-2553.
[193] P.L. Rossiter, The Electrical Resistivity of Metals and Alloys, Cambridge University Press, 1987.
[194] E. Nes, Acta Metal., 24 (1976) 391-398.
[195] F. Gatto, G. Camona, M. Conserva, P. Fiorini, Mater. Sci. Eng., 3 (1968/69) 56-61.
[196] L.M. Wu, W.H. Wang, Y.F. Hsu, S. Trong, J. Alloys. Compounds, 456 (2008) 163-169.
[197] B. Morere, C. Maurice, R. Shahani, J. Driver, Metall. Mater. Trans. A, 32A (2001) 625-632.
[198] J.D. Robson, Mater. Sci. Eng. A, 338 (2002) 219-229.
[199] A.R. Eivani, PhD Thesis, Delft, The Netherlands, 2010.
[200] P.V. Raymond, J.W. Martin, Z. Metallkde, 70 (1979) 80-84.
[201] H. Zhang, L. Li, D. Yuan, D. Peng, Mater. Charact., 58 (2007) 168-173.
[202] G.C. Weatherly, A. Perovic, N.K. Mukhopadhyay, D.J. Lloyd, D.D..Perovic, Metall. Mater. Trans. A, 32A (2001) 213-218.
[203] A. Biswas, D.J. Siegel, C. Wolverton, D.N..Seidman, Acta Mater., 59 (2011) 6187-6204.
[204] A. Biswas, D.J. Siegel, D.N. Seidman, Phys. Rev. Lett., 105, 076102 (2010) 1-4.
[205] Z.B. Jiao, J.H. Luan, M.K. Miller, C.Y. Yu, C.T. Liu, Acta Mater., 84 (2015) 283-291.
[206] G.E. Dieter, Mechanical Metallurgy, 2nd edition, McGraw-Hill, 1976.
[207] M.F. Ashby, Oxide dispersion strengthening, In: AIME conf. proc., New York, Met. Soc. AIME, 1966.
[208] E. Ogris, H. Luchinger, P.J. Uggowitzer, Mater. Sci. Forum, 152 (2002) 396-402.
[209] R.K.W. Marceau, A. de Vaucorbeil, G. Sha, S.P. Ringer, W.J. Poole, Acta Mater., 61(2013) 7285-7303.
[210] S. Gungor, L. Edwards, Materials Science and Engineering A, 160 (1993) 17-24.
[211] L. Zeng, T. Shikama, Y. Takahashi, S. Yoshihara, T. Aiura, H. Noguchi, International Journal of Fatigue, 44 (2012) 32-40.
[212] Y. Takahashi, H. Yoshitake, R. Nakamichi, T. Wada, M. Takuma, T. Shikama, H. Noguchi, Materials Science and Engineering A, 614 (2014) 243-249.
[213] D. Azzam, Craig C. Menzemera, T.S. Srivatsanb, Materials Science and Engineering A, 527 (2010) 5341-5345.
[214] L. Edwards, A.K. Busby, J.W. Martin, Materials Science and Technology, 2 (1986) 823-828.
[215] D.M. Jiang, B.D. Hong, T.C. Lei, Scripta Metallurgica, 24 (1990) 651-654.
[216] D. Jiang, C. Wang, Materials Science and Engineering A, 352 (2003) 29-33.

[217] D.M. Jiang, B.D. Hong, T.C. Lei, D.A. Downham, G.W. Lorimer, Materials Science and Technology, 7 (1991) 1010-1014.
[218] J.M. Boileau, J.E. Allison, Metallurgical and Materials Transactions A, 34A (2003) 1807-1820.
[219] Y. Zhang, H. Luo, T. Zhai, Advanced Materials Research, 139-141(2010) 251-254.
[220] P. Daswa, H. Möller, M. du Toit, G. Govender, Solid State Phenomena, 217-218 (2014) 259-264.
[221] Materials Science International Team MSIT, Bodak, Oksana, Chakrabarti, Nirupan, Kumar, Hari, Lukas, Hans-Leo, Rokhlin, Lazar, Aluminium- Magnesium-Silicon.Springer Materials- The Landolt-Börnstein Database (http://www.springermaterials.com). DOI: 10.1007/10915998_18
[222] T. Zhai, A.J. Wilkinson, J.W. Martin, Acta Mater., 48 (2000) 4917-4927.
[223] A.T. Brammer, master thesis, Alabama, USA, 2013.
[224] W. Wen, A.H.W. Ngan, Y. Zhang, B. Xu, T. Zhai, Materials Science and Engineering A, 564 (2013) 97-101.

VITA

Gongwang Zhang

Education

- University of Kentucky, Lexington, Kentucky, USA

  Aug. 2013 - At present Ph.D. Candidate (Materials Engineering)

- RWTH Aachen University, Aachen, Nordrhein-Westfalen, Germany

  Oct. 2009 - Jan. 2013 M.S. (Metallurgical Engineering)

- University of Science and Technology Beijing, Beijing, China

  Sep. 2005 - Jul. 2009 B.E. (Materials Science and Engineering)

Honors and Awards

- Best Student Poster Finalist Award, CNMS (Center for Nanophase Materials Sciences) User Meeting, Oak Ridge National Laboratory, 2015

Publications

- S. Jin, T. Ngai, G. Zhang, T. Zhai, S. Jia, L. Li, Precipitation strengthening mechanisms during natural ageing and subsequent artificial aging in an Al-Mg-Si-Cu alloy, Materials Science and Engineering A, 724 (2018), pp. 53-59.
- Y. Xu, H. Nagaumi, Y. Han, G. Zhang, T. Zhai, The deformation behavior and microstructure evolution of a Mn- and Cr-containing Al-Mg-Si-Cu alloy during hot compression and subsequent heat treatment, Metallurgical and Materials Transactions A, 48 (2017), pp. 1355-1365. (Equal contribution to this research work)
- G. Zhang, H. Nagaumi, Y. Han, Y. Xu, C.M. Parish, T. Zhai, Effects of Mn and Cr additions on the recrystallization behavior of Al-Mg-Si-Cu alloys, Materials Science Forum, 877 (2016), pp. 172-179.
- L. Hu, G. Zhang, W. Hu, G. Gottstein, S. Bogner, A. Bührig-Polaczek, Tensile creep of directionally solidified NiAl-9Mo in situ composites, Acta Materialia, 61 (2013), pp. 7155-7165.
- G. Zhang, L. Hu, W. Hu, G. Gottstein, S. Bogner, A. Bührig-Polaczek, Mechanical properties of NiAl-Mo composites produced by specially controlled directional solidification, 2012 MRS Fall Meeting, 1516 (2013), pp. 255-260.
- G. Zhang, T. Zhai, G. Sha, etc., Manganese-induced precipitation in a modified AA6061 (Al-Mg-Si-Cu) alloy during homogenization, to be submitted
- G. Zhang, T. Zhai, G. Sha, etc., Effects of different homogenization treatments on dispersoids formation in modified AA6061 (Al-Mg-Si-Cu) alloys, to be submitted
- Other 2-3 manuscripts are being drafted

Conference Oral Presentations

- G. Zhang, Y. Han, Q. Zhou, H. Nagaumi, G. Sha, C. Parish, D. Leonard, T. Zhai, Manganese-induced precipitation in a modified AA6061 (Al-Mg-Si-Cu) alloy during homogenization, 2017 TMS meeting, San Diego, California, USA
- G. Zhang, T. Zhai, Y. Han, Y. Xu, H. Nagaumi, G. Sha, C. Parish, D. Leonard, A study of the formation mechanism of Mn containing precipitates during homogenization in a 6xxx series aluminum alloy, 2016 TMS meeting, Nashville, Tennessee, USA
- G. Zhang, Y. Han, Y. Xu, H. Nagaumi, G. Sha, C. Parish, D. Leonard, T. Zhai, A formation mechanism of Mn containing precipitates during homogenization in 6xxx series aluminum alloys, 2016 MACE spring symposium, Lexington, Kentucky, USA (poster)
- G. Zhang, Y. Han, Y. Xu, H. Nagaumi, G. Sha, C. Parish, T. Zhai, A study of formation mechanism and recrystallization behavior of Mn containing precipitates during homogenization in 6xxx series aluminum alloys, 2015 TMS meeting, Orlando, Florida, USA (Invited)
- G. Zhang, Y. Han, Y. Xu, H. Nagaumi, G. Sha, C. Parish, D. Leonard, T. Zhai, A formation mechanism of Mn containing precipitates during homogenization in 6xxx series aluminum alloys, 2014 and 2015 CNMS User Meeting, Oak Ridge National Laboratory, Oak Ridge, Tennessee, USA (poster)
- G. Zhang, Y. Han, H. Nagaumi, G. Sha, C. Parish, T. Zhai, A study of precipitation sequence and formation mechanism of high temperature second phases in a modified 6xxx Al alloy, 2014 TMS meeting, San Diego, California, USA